The main objective of this book is designing Next Generation Optical Telescope (NGOT) to gather information from a far region of space and illustrates with simulation the Adaptive Optics system. The Quality of images and spectra taken at ground-based astronomical observations is degraded by distortions in the Earth's atmosphere. Compensation of the atmospheric seeing can be achieved using the technology of Adaptive Optics, a technique which is being pursued by every major ground-based observatory. The techniques of adaptive Optics are those by which telescope optics is adjusted on a rapid time scale to compensate for distortions in the wave front entering a telescope.

R.N.Hassan is an assistant prof. and vice presidant in Al-karkh university of science, got B.Sc.(1998),M.Sc. (image processing 2002),Ph.D.(remote sensing 2012) in Baghdad Univ., he taught courses in astronomical techniques, astronomical applications for elementary level and adaptive optics, fourier optics for advanced level in astronomy and space.

978-3-659-96966-9

1st Edition

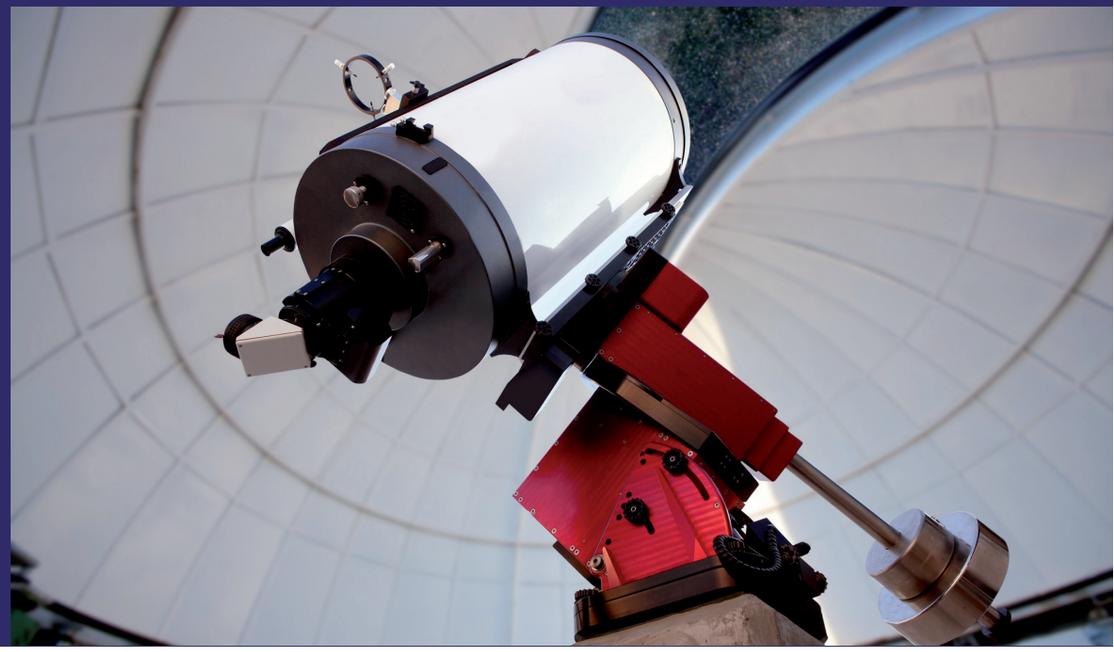

Raaid N. Hassan
Loay K. Abood
Shatha M. Al-Hilly

Computer Simulation of Segmented Mirrors for large Optical Telescopes

LAP LAMBERT Academic Publishing

N. Hassan, K. Abood, M. Al-Hilly

Raaid N. Hassan
Loay K. Abood
Shatha M. Al-Hilly

Computer Simulation of Segmented Mirrors for large Optical Telescopes

Raaid N. Hassan
Loay K. Abood
Shatha M. Al-Hilly

Computer Simulation of Segmented Mirrors for large Optical Telescopes

LAP LAMBERT Academic Publishing

Impressum / Imprint
Bibliografische Information der Deutschen Nationalbibliothek: Die Deutsche Nationalbibliothek verzeichnet diese Publikation in der Deutschen Nationalbibliografie; detaillierte bibliografische Daten sind im Internet über http://dnb.d-nb.de abrufbar.

Bibliographic information published by the Deutsche Nationalbibliothek: The Deutsche Nationalbibliothek lists this publication in the Deutsche Nationalbibliografie; detailed bibliographic data are available in the Internet at http://dnb.d-nb.de.

Coverbild / Cover image: www.ingimage.com

Verlag / Publisher:
LAP LAMBERT Academic Publishing
ist ein Imprint der / is a trademark of
OmniScriptum GmbH & Co. KG
Bahnhofstraße 28, 66111 Saarbrücken, Deutschland / Germany
Email: info@omniscriptum.com

Herstellung: siehe letzte Seite /
Printed at: see last page
ISBN: 978-3-659-96966-9

Zugl. / Approved by: University of Baghdad, College of Science, 2012

Computer Simulation of Segmented Mirrors for large Optical Telescopes

By

Dr. Raaid N. Hassan
Dr. Loay K. Abood
Dr. Shatha M. Al-Hilly

Acknowledgments

First, the author thanks deeply Allah for supporting him to achieve this work. He wishes to express his great thanks and the sincerest gratitude to my supervisors Dr. Loay K. Abood & Dr. Shatha M. Al-Hilly for their valuable guidance and useful suggestions.

My greatest thanks and sincerest gratitude is to my colleagues especially: Shaker Ali, Bushra Ali, Khudair Abbas, Thamir Abd-Alamir, Mekky Al-Maliky, Hany Kbashi, and also extended to Firas A. Hadi.

I would like to present my deeps acknowledge to Professor Aziz Ziad.

Also, I would like to thank all Astronomy Department staff for their support, specially the head of the department, Dr. Kmal M. Abood and Prof. Dr. Ali Talib for their supports and encouragements.

Finally, I express my deep gratefulness to my Family for their patience and encouragement throughout this work. And I have to say thank you for every thing.

Raaid Nawfee Hassan

Abstract

The main objective of designing a Next Generation Optical Telescope (*NGOT*) is to gather information from the far regions of space. The information will be used for understanding the: Universe structure, birth and evolution of stars, origins and evolution of planetary systems and galaxies. The key element to achieve these goals is to build a space and/or ground based telescopes with a large reflector mirror. Many difficulties are associated with the size of such reflectors; to overcome these problems is to build a ground or space optical telescope with a number of small mirrors. These mirrors can be deployed inside the space launch vehicle for space telescope and then adjusted together in the orbit to form a desired shape of a single larger reflector; however, on earth the ground-based optical telescope is easily manufactured with less cost.

Simulation results showed that the hexagonal apodized aperture with subsegments hexagon 6-6 configuration, which has 72 subsegments was the recommended design for designing the next generation optical telescope.

Beside the new configuration for the future telescope other approach force itself to improve the performance to achieve the diffraction limit like Deformable Mirror (DM) and Adaptive Optics (AO). Preliminary test of the wavefront and Point Spread Function (PSF) reconstruction using theories of numerical modeling for a single DM AO system has been performed and the preliminary results are presented.

To construct the DM surface for compensation the perturbed incident wavefront four methods are adopted; Zernike polynomials, modified Zernike polynomials, poke matrix and trigonometric function (the suggested) methods. The simulation results showed that the suggested method is more accurate and less consuming calculation time.

Abbreviation and Acronyms

AITC	Advanced Instrumentation and Technology Centre
AO	Adaptive Optics
AT	Auxiliary Telescopes
DM	Deformable Mirror
EE	Encircled Energy
FFT	Fast Fourier Transform
FWHM	Full Width at Half Maximum
GMOS	Gemini Multi-Object Spectrographs
GTC	Gran Telescope Canaries
HST	Hubble Space Telescope
HET	Hobby-Eberly Telescope
IF	Influence Functions
IFU	Integral Field Unit
JWST	James Webb Space Telescope
LBT	Large Binocular Telescope
LGS	Laser Guide Star
MEMS	Micro-Electro-Mechanical Systems
MOAO	Multi-Object Adaptive Optics
MTF	Modulation Transfer Function
NGOT	Next Generation Optical Telescope
NGST	Next Generation Space/Segmented Telescope

OTF	Optical Transfer Function
PSF	Point Spread Function
PSNR	Peak Signal to Noise Ratio
PSD	Power Spectrum Density
P-V	Peak-to-Valley
RMS	Root Mean Square
RSAA	Research School of Astronomy and Astrophysics
SAAO	South African Astronomical Observatory
SALT	Southern African Large Telescope
SH	Shack-Hartmann
SH-WFS	Shack Hartmann Wavefront Sensor
SVD	Singular-Value Decomposition
VLTI	Very Large Telescope Interferometer
WF	Wavefront
WFS	Wavefront Sensor

Table of Contents

Chapter One

General Introduction

1.1 Introduction

Astronomers had studied celestial objects since ancient times like stars, comets and planets. The fields of theoretical and observational astronomy are deeply linked to other natural sciences, such as physics, chemistry and even biology. For example, recent discoveries of planets orbiting other stars are giving the opportunity to think about life beyond Earth, and to link astronomy and biology. With a scientific basis for the first time in human history the old question "are we alone?" may be answered.

Observational astronomy is part of astronomy that deals with research on objects in the sky through scientific observation. The telescope development, such as Galileo's telescope, which was built 400 years ago, is a key tool for this purpose. This has enabled steady growth in the volume and accuracy of observations of very faint objects, allowing astronomers to make transcendental discoveries, such as the rapid expansion of the universe or the existence of massive black hole at the center of our galaxy [1].

The astronomical optical telescope has evolved from a small, manually pointed device for visual observations to a large and sophisticated computer-controlled instrument with full digital output. All know that astronomers use telescopes to study the far reaches of space. But an astronomer's telescope would be useless without the instruments that measure and analyze the light that telescopes gather. Often, astronomers create their own instruments depending on what they are studying.

Throughout this development, two parameters have been particularly important: the light-collecting power or diameter of the telescope (allowing the detection of fainter and more distant objects) and the angular resolution (or image sharpness). For a perfect telescope used in vacuum, resolution is directly proportional to the inverse of the telescope diameter. A plane wavefront from distant star (effectively at infinity) would be converted by the telescope into a perfectly spherical wavefront, forming the image, with an angular resolution only limited by light diffraction - aptly called the diffraction limit [2].

New discoveries and exciting as these are the ones that are waiting for the next generation of optical telescopes, which will be built in selected locations on Earth, where the thin air above the telescope allows observations of an unprecedented quality. The next generation of telescopes conveniently named "Extremely Large Telescopes" or ELTs, are to signify a leap forward for their predecessors. [3].

Ambitions are to use a mirror diameter of more than 100m for the next generation. In order to build these giant machines the need to develop a new technologies, as well as, overcoming the obstacles, monetary and politics. The work

reported in this book is part of the development of new technologies for the next generation of the optical telescopes.

Ground-based telescopes suffer from the negative effects of the atmosphere, even in the best astronomical sites on Earth.

Adaptive optics is a technique that deals with the effect of atmospheric turbulence on the performance of the telescope, in order to compensate for turbulence in real time while collecting the light from the sky for astronomical observation. The system of adaptive optics in the telescope increases the spatial resolution of obtained images. The spatial resolution in a telescope image improves as the diameter of the telescope gets larger. This allows the resolution of the individual point sources (stars for example) that are close to each other in the sky to be resolved. High spatial resolution allows observing the components of the distant galaxy, enabling the study of its internal structure [4] [5].

This science is not possible if the resolution were limited such that observing the galaxy as a diffuse nebula. The spatial resolution is function of wavelength and size of the optical element, and preferably larger telescopes not only because of their region's large collection, but also because of the spatial resolution that can be achieved [6].

1.2 Current Segmented- Mirror Telescopes

According to Wikipedia, the free encyclopedia, the Gran Telescope Canaries (GTC) is the largest optical telescopes on Earth; with a 10.4m segmented primary mirror have 36 hexagonal segments. It is located in one of the top astronomical sites in the northern hemisphere- Canary Islands. The “First Light” event took place on July 13, 2007.

The next largest is the two 10m Keck I and Keck II telescopes located on the summit of Hawaii’s dormant Mauna Kea volcano as shown in figure (1.1). Each stands eight stores tall and weighs 300 tons, yet operates with nanometer precision. At the heart of each Keck Telescope is a revolutionary primary mirror. Ten meters in diameter, the mirror is composed of 36 hexagonal segments that work in concert as a single piece of reflective glass.

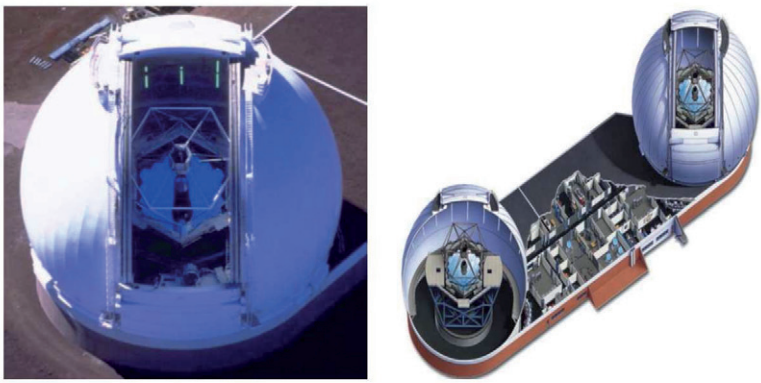

Figure (1.1): Two 10m Keck Telescope [8].

Then the 10m Southern African Large Telescope (SALT) was introduced. The South African Astronomical Observatory (SAAO) is the national centre for optical and infrared astronomy in South Africa. The SALT is the largest single optical telescope in the southern hemisphere, with a hexagonal mirror array 9.2m across. Although very similar to the Hobby-Eberly Telescope (HET) in Texas, SALT has a redesigned optical system using more mirror array. With this telescope it is able to record distant stars, galaxies and quasars a billion times too faint to be seen with the unaided eye as faint as a candle flame at the distance of the moon.

The 9.2m Hobby-Eberly telescope in mount Fowlkes, Texas is the objective: to gather a very large amount of light, specifically for spectroscopy, at extremely low cost. A fixed elevation-axis design, based on the radio telescope at Arecibo, and an innovative system for tracking stars, contributed to an 80% reduction in initial costs compared to optical telescopes of similar size. The HET's 9.2m effective aperture have 91 hexagonal segments makes it currently the world's fourth largest optical telescope. The HET entered its commissioning phase in 1997, and began science operations in October of 1999.

The Large Binocular Telescope (LBT) is located in mounts Graham, Arizona as shown in figure (1.2). These twins are 8.4m each. The Large Binocular Telescope uses an elevation over an azimuth mounting. The elevation optical support structure moves on two large C-shaped rings and the compact azimuth platform transmits the loads directly down to the pier. The two 8.4m diameter primary mirrors are mounted with a 14.4m center-center separation. The light-gathering power of the two primary mirrors

combined is equivalent to an 11.8m telescope and the angular resolution of a 22.8m telescope when the LBT is used as an interferometer. The short focal length of the primary mirrors (f/ no = 1.142) permits a compact and therefore quite stiff telescope structure.

Figure (1.2): Large Binocular Telescope Observatory [8].

The Suburu telescope is an optical-infrared telescope at the Mauna Kea on the island of Hawaii. The telescope represents a new generation in telescope design not only because of the size of its primary mirror with an effective aperture of 8.2m, but also because of the various revolutionary technologies used to achieve outstanding performance. An active support system that maintains an unprecedentedly high mirror surface accuracy is the new enclosure design to suppress local atmospheric turbulence, with extremely accurate tracking mechanism using magnetic driving systems. Seven observational instruments installed at the four foci, and auto-exchanger systems to use the observational instruments are effectively just some of the unique features associated with this telescope.

There are four 8.2m diameter telescopes located in Cerro Paranal, Chile. The Very Large Telescope Interferometer (VLTI) with its own suite of instruments, ultimately providing imagery at the milli-arcsecond level as well as astrometry at 10 micro-arcsecond precision. In addition to the 8.2m telescopes the VLTI will soon be complemented with four Auxiliary Telescopes (AT) of 1.8m diameter to improve its imaging capabilities and enable full nighttime use on a year-round basis.

The 8.1m diameter Gemini telescope is in Mauna Kea, Hawaii (North) and the other is in Cerro Pachon, Chile as shown in figure (1.3). The two Gemini Multi-Object

Spectrographs (GMOS), one on each telescope, provide multi-slit spectroscopy and imaging over a 5.5 arcmin field of view. Each GMOS is also equipped with an Integral Field Unit (IFU) making it possible to obtain spectra of an area of about 35 square arcsec with a sampling of 0.2 arcsec. The Nod-Shuffle mode enables superior sky subtraction, available with both GMOSs in most spectroscopic modes.

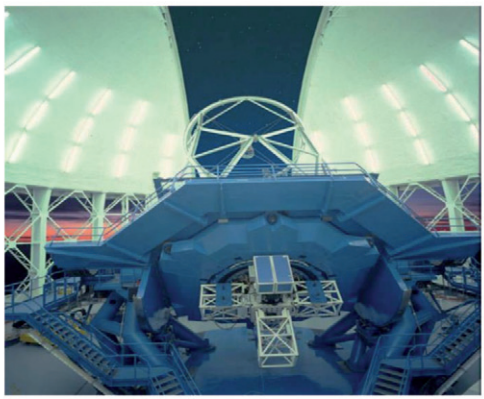

Figure (1.3): Gemini Observatory [8].

Figures (1.4, 1.5) show the observatory layout, structure, segmented aperture, and the main components of the optical telescope.

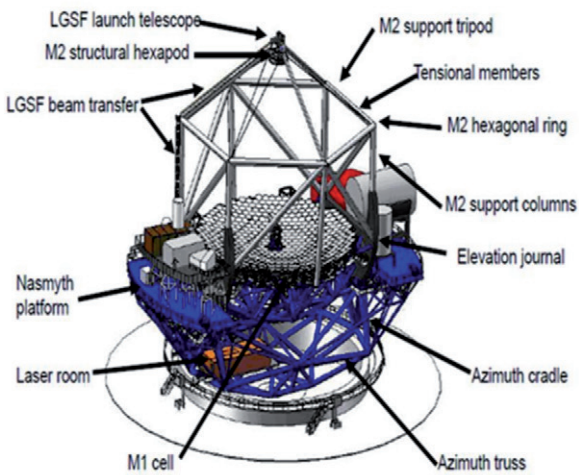

Figure (1.4): Observatory Layout for Optical Telescope [7].

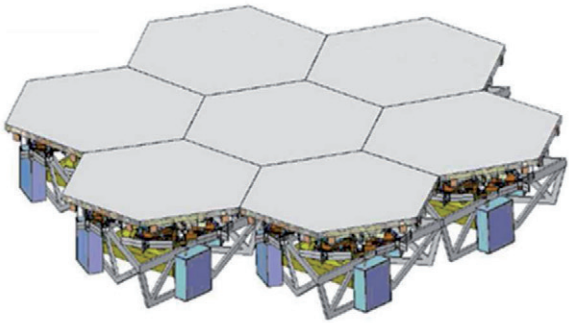

Figure (1.5): Top View of Segmented Aperture [7]

Table (1-1) contains telescopes with aperture greater than 5m with some details.

Table (1-1): Largest Ground-Optical Telescopes

Aperture (m)	Circular aperture equiv. (m)	Telescope name	location	Date of operation	Primary f/no	Mirror type	Mirror aspect ratio	Mounting type	Ref.
2x8.4	11.8	Large Binocular Telescope (LBT)	Mt. Graham, Arizona	2006	1.14	Honeycomb	9.4	Alt-Az	1
10.4	10.4	Gran telescope Canarias (GTC)	La Palma, Canary Islands, Spain	2009	1.65	Segmented	125	Alt-Az	3
10	10	Keck I	Mauna Kea, Hawaii	1993	1.75	segmented	133	Alt-Az	2
10	10	Keck I	Mauna Kea, Hawaii	1996	1.75	segmented	133	Alt-Az	2
9.2	9.2	Hobby-Eberley Telescope (HET)	Mt. Fowlkers, Texas	1997	1.4	segmented	200	Azimuth only	4
9.2	9.2	Southern African Large Telescope (SALT)	Sutherland South Africa	2005	1.4	segmented	200	Azimuth only	
8.2	8.2	Subaru	Mauna Kea, Hawaii	1999	1.8	Meniscus	41	Azimuth only	6
8.2	8.2	Very Large Telescope VLT (UT1)	Cerro Paranal, Chile	1998	1.75	Meniscus	46	Alt-Az	7

8.2	8.2	Very Large Telescope VLT (UT2)	Cerro Paranal, Chile	1999	1.75	Meniscus	46	Alt-Az	7
8.2	8.2	Very Large Telescope VLT (UT3)	Cerro Paranal, Chile	2000	1.75	Meniscus	46	Alt-Az	7
8.2	8.2	Very Large Telescope VLT (UT4)	Cerro Paranal, Chile	2000	1.75	Meniscus	46	Alt-Az	7
8.0	8.0	Gemini North	Mauna Kea, Hawaii	1999	1.8	Meniscus	40	Alt-Az	8
8.0	8.0	Gemini North	Mauna Kea, Hawaii	2001	1.8	Meniscus	40	Alt-Az	8
6.5	6.5	MMT Conversion	Arizona	2000	1.25	Honeycomb	9	Alt-Az	9
6.5	6.5	Magellan I	Chile	2000	1.25	Honeycomb	9	Alt-Az	10
6.5	6.5	Magellan II	Chile	2002	1.25	Honeycomb	9	Alt-Az	10
6.0	6.0	Large Zenith Telescope (LZT)	Canada	2003	1.5	Liquid Hg		Fixed	11
6.0	6.0	BTA-6	Russia	1975	4	solid	6	Alt-Az	12
5.1	5.1	Hale Telescope	California	1948	3.3	Honeycomb	8	Equatorial	13

References

(1) http:// lbto.org/, (2) http:// http://www.keckobservatory.org//, (3) http://www.gtc.iac.es/, (4) http://www.as.utexas.edu/mcdonald/het/het.html, (5) http://www.salt.ac.za/, (6) http://www.naoj.org/, (7) http://www.eso.org/, (8) http://www.gemini.edu/, (9) http://www.mmto.org/, (10)http://www.ociw.edu/magellan/magellan.html, (11) http://www.astro.ubc.ca/LMT/, (12) http://www.sao.ru/, (13) http://astro.caltech.edu/observatories/palomar/

Table (1-2): Sky Survey Telescopes

Survey	Status	Aperture (m)	f/no	Field of View (degree^2)	Magnitude	Speed (degree^2 per hour)	Ref.
CSS-Mt. Lemmon	Operational	1.5	2.0	1.3	21	20	1
CSS-Catalina	Operational	0.68	1.9	8	19.5	150	1
CSS-Siding Spring Uppsala	Operational	0.5	3.5	4.2	19.5	75	1
LINEAR	Operational	2x1.0	2.2	2.0	19.5	1200	2
LONEOS (Schmidt)	Operational	0.44	1.9	8.3	19.3	106	3
LONEOS (USNO)	In development	1.3	2.4	1.3	21.4	15	3
NEAT (Palomar)	Operational	1.2	1.5	9.5	22.5	85	4
NEAT (MSSS)	Operational	1.2	3.0	2.3	19.7	40.5	4
NEAT (Schmidt)	In development	1.2	2.5	9.4	20.0	50	4
Spacewatch (Mosaic)	Operational	0.93	3.0	2.9	21.5	160	5
Spacewatch (1.8m)	Operational	1.82	2.7	0.32	22.5	8.9	5
Pan-STARRS (Hawaii)	In development	4x1.8	4	3.0	24.0	700	6
Discovery Channel Telescope (Lowell)	In development	4.0	2.2	3.1	21.8	110	7
Large Synoptic Survey Telescope	proposed	6.9	1.25	7	24	2500	8

References

(1) Catalina Sky Survey, http://www.lpl.arizona.edu/css/, (2) Lincoln Near Earth Asteroid Research, http://www.ll.mit.edu/LINEAR/, (3) Lowell Observatory Near-Earth-Object Search, http://asteroid.lowell.edu/asteroid/loneos/loneos1.html, (4) Near-Earth Asteroid Tracking, http://neat.jpl.nasa.gov/, (5) http://spacewatch.lpl.arizona.edu/, (6) Panoramic Survey Telescope & Rapid Response System, http://pan- starrs.ifa.hawaii.edu/public/, (7) http://www.lowell.edu/, (8) http://www.lsst.org/

For table (1-2) that contains the summary of the sky survey telescopes:

1. Field-of-view is the area of sky covered in a single exposure.
2. Magnitude limit is the faintest star recorded at visible wavelengths.
3. Speed is the rate at which observations can be carried out. One can see that of the operational facilities, LINEAR covers the most sky per hour (1200 degree/hour) but

the faintest stars it can observe at this speed 19.4 mag. The Spacewatch 1.8m telescope can observe stars that are 3 magnitudes fainter but at a speed of only 8.9 degree/hour.

1.3 Reflecting Telescopes

Reflecting telescopes and their associated instrumentation are the principal tools of the observational astronomer. In this section the characteristics of the reflecting telescope is considered. Although refracting telescopes are still in use, they are relatively few in number and do not compete in light gathering power with the large reflectors.

Figure (1.6) is the schematic of different telescope mounts: (a) equatorial, (b) alt-az, (c) azimuth only, (d) fixed. The Hale 5.1m telescope is the last large telescope to be built with an equatorial mount. The equatorial mount has one axis aligned to the rotation axis of the earth. All fully steerable large telescopes utilize the alt-az mount, such as the Keck, Gemini, VLT, and Subaru telescopes (see Table (1.1)) [8].

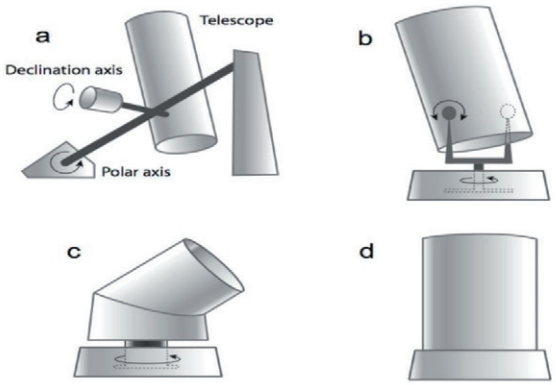

Figure (1.6): Schematic of different telescope mounts: (a) equatorial, (b) alt-az, (c) azimuth only, (d) fixed.

1.4 The next Generation Optical Telescope

The Next Generation Space Telescope (NGST) or complex next generation segmented telescope (NGST) system represents a challenging problem from the point of view of maintaining a milli-arcsecond level pointing accuracy and diffraction limited wavefront performance in the presence of dynamic onboard disturbances during science observations. This is due to the fact that NGST will make extensive use of deployable, inflatable and lightweight components, which leads to high modal density and light damping of the structural plant. An integrated model comprising multiple disturbance sources, structures, optics and control systems was developed in

order to predict the expected dynamic performance of the observatory in term of wavefront error. Figure (1.7) shows the scientific window for NGST observation [16] [9].

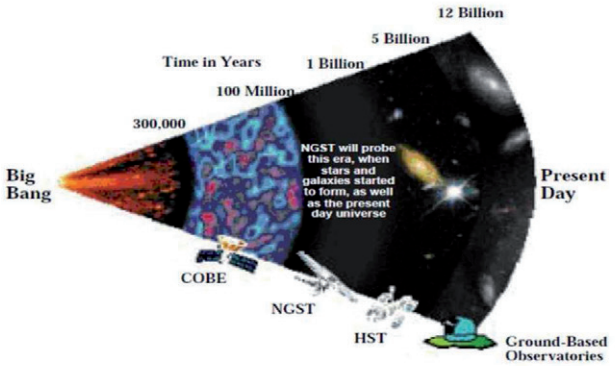

Figure (1.7): The Scientific Window for NGST Observation

Next generation optical telescope must be able to see object 400 times fainter than those currently studied with large ground-based infrared IR telescopes, such as Keck observatory or current generation of space-based Infrared telescopes (e.g. space IR telescope facility (SIRTF)).
Figure (1.8) illustrates one of the NGST designs being considered [10].

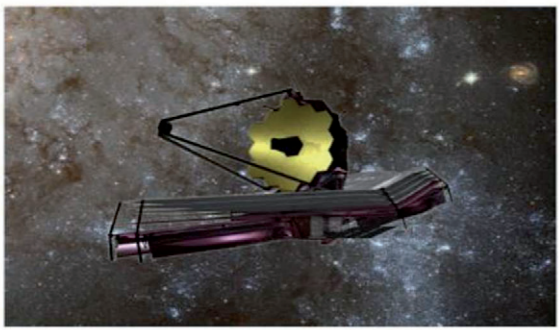

Figure (1.8): The James Webb Space Telescope [NASA image]

1.5 Literature Review

Thorough reviews of next generation optical telescope and related issues can be found in the key sources.

In 1987, C. F. Dunkl presented orthogonal polynomials on the hexagon. Least-square approximation by polynomials, with respect to area measure on the regular hexagon, is useful in the construction and analysis of hexagonal optical elements.

Notably the Keck ten meter telescope will utilize a main mirror composed of thirty six hexagonal segments. The computations can be carried out in rational (exact) arithmetic, and an appendix lists the polynomials and orthogonal expansions of monomials up to degree six [11].

In 1992, R. G. Lane et al. presented a simulation of a Kolmogorov phase screen. Two new methods for modeling Kolmogorov phase fluctuations over a finite aperture are described. The firs method relies on the incorporation of sub harmonics in order to model accurately the low frequencies of the Kolmogorov Spectrum. The second method provides a less accurate, but much faster method for simulating the Kolmogorov spectrum by using a midpoint displacement algorithm used in computer graphics [12].

In 1994, W. Swantner and W. W. Chow presented a Gram-Schmidt orthonormalization of Zernike polynomials for general aperture shapes. They had shown that the Zernike functions for circular apertures can be generalized for any aperture shape. Completely general aperture shapes and user-selected basis sets may be treated with a digital Gram-Schmidt orthonormalization approach [13].

In 1994, V. N. Mahajan presented Zernike circle polynomials and optical aberrations of systems with circular pupils. Zernike circle polynomials, their numbering scheme, and relationship to balanced optical aberrations of systems with circular pupils were discussed [14].

In 1994, G. Love and A. K. Saxena presented an active and adaptive optics for the new generation of large telescopes. Active and adaptive optics were techniques for improving the image quality of large astronomical telescopes. Active optics was concerned with correcting aberrations produced within the telescope and adaptive optics aims to correct distortions introduced by the Earth's atmosphere [15].

In 1996, L. M. Mugnier et al. presented an aperture configuration optimality criterion for phased arrays of optical telescopes. Address the optimization of the relative arrangement (aperture configuration) of a phased array of optical telescopes, coherently combined to form images of extended objects in a common focal plane [16].

In 1999, A. Glindemann et al. presented an adaptive optics on large telescopes. They discussed the physical background of imaging through turbulence, using Kolmogorov statistics, and different techniques to sense and to correct the wavefront aberrations with adaptive optics. [17].

In 1999, O. L. de Weck and D. W. Miller presented an integrated modeling and dynamics simulation for the next generation space telescope. An integrated model comprising multiple disturbance sources, structures, optics and control systems was developed in order to predict the expected dynamic performance of the observatory in terms of wavefront error and line-of-sight jitter. [18].

In 2001, J. S. Gibson, C. C. Chang and Neil Chen presented an adaptive optics with a new modal decomposition of actuator and sensor spaces. They introduced a new modal decomposition of actuator and sensor spaces for adaptive optics. The decomposition, which was based on the singular value decomposition of the "poke matrix," provides orthonormal bases, or modes, for both actuator and sensor spaces [19].

In 2003, G. Z. Angeli et al. presented an active optics and control architecture for a giant segmented mirror telescope. The next generation 30m class ground-based telescopes pose an unprecedented challenge for control systems envisioned to support diffraction limited imaging. The approach is a multi-tiered, decentralized control architecture utilizing two kinds of feedback: optical and mechanical [20].

In 2003, R. Angel et al. presented a 20 and 30 m telescope designs with potential for subsequent incorporation into a track-mounted pair (20/20 or 30/30). Any future giant ground-based telescope must, at a minimum, provide foci for seeing-limited imaging over a wide field and for diffraction-limited imaging over ~1 arcminute fields corrected by adaptive optics (AO). Large round segments can also be individually apodized for high-contrast imaging of exoplanets [21].

In 2004, C. Cox and P. Hodge presented a point spread function modeling for the James Webb Space Telescope. They described software which models the Point Spread Function of the James Webb Space Telescope. This software is designed to be expandable to incorporate optical and instrument data as they become available. An initial model of the detector used in the Near Infrared Camera has been used to generate realistic stellar images [22].

In 2005, E. Sabatke et al. presented an analytic diffraction analysis of a 32-m telescope with hexagonal segments for high-contrast imaging. Large segmented telescopes cannot be modeled accurately with fast-Fourier-transform techniques since small features such as gaps between the segments will be inadequately sampled. Apodizing the edges of the individual segments reduced the useful regions in the image since the gaps appeared to be wider [23].

In 2007, A. Beasley presented a Xinζtics Deformable Mirror. The Research School of Astronomy and Astrophysics (RSAA) was loaned a Deformable Mirror (DM) by Gemini in return for its characterization. This DM was manufactured to test an actuator design to be incorporated into the Gemini Multi-Conjugate Adaptive Optics program. The experiments were undertaken between July 2006 and May 2007 [24].

In 2007, V. N. Mahajan, and G. m. Dai presented Orthonormal polynomials in wavefront analysis: analytical solution. Zernike circle polynomials are in widespread use for wavefront analysis because of their orthogonality over a circular pupil and their representation of balanced classical aberrations. Derived closed form polynomials that

are orthonormal over a hexagonal pupil, such as the hexagonal segments of a large mirror. [25].

In 2007, A. Basden et al. presented a Durham extremely large telescope adaptive optics simulation platform. Simulation of adaptive optics systems on the largest proposed future extremely large telescopes, as well as, on the current systems. The simulation platform described can be highly parallelized using parallelization techniques suited for adaptive optics simulation. The results from the simulation of a ground layer adaptive optics system were provided as an example to demonstrate the flexibility of this simulation platform [26].

In 2007, G. m. Dai presented a wavefront reconstruction from slope data within pupils of arbitrary shapes using iterative Fourier transform. This presents a new modal technique that reconstructs a wavefront using iterative Fourier transforms and converts the Fourier coefficients as needed to from the coefficients of the orthonormal basis set over pupils of arbitrary shapes. Elliptical, annular, hexagonal, and irregular pupils are considered as practical examples to illustrate the results [27].

In 2007, L. Jolissaint et al. presented an analytical modeling of the optical transfer function of a segmented telescope with/without adaptive optics correction of the telescope's dynamical aberrations. They presented the mathematical development of the method, and give an example of application to a 73 segments 10-m telescope, without adaptive optics correction [28].

In 2007, A. M. Hvisc and J. H. Burge presented a structure function analysis of mirror fabrication and support errors. Telescopes are ultimately limited by atmospheric turbulence, which is commonly characterized by a structure function. The fabrication and support errors are most naturally described by Zernike polynomials or by bending modes for the active mirrors [29].

In 2008, T. Gray and D. W. Miller presented a minimizing high spatial frequency residual in active space telescope mirrors. The trend in future space telescopes is towards large apertures and lightweight, rib-stiffened, and actively controlled deformable mirrors. This book details efforts to evaluate the mirror correction limit and the three predominant high spatial frequency mirror surface residual components: actuation-induced dimpling, manufacturing-induced print-through, and disturbance-induced uncorrectable error. [30].

In 2008, E. Sidick et al. presented an improved wavefront control algorithm for large space telescopes. Wavefront sensing and control is required throughout the mission lifecycle of large space telescopes such as James webb space telescope (JWST). They propose a simple approach for preventing a sensitivity-matrix from singularity. Also introduce a new “minimum-wavefront and optimal control compensator” [31].

In 2008, G. m. Dai, and V. N. Mahajan presented Orthonormal polynomials in wavefront analysis: error analysis. They illustrated that the wavefront fitting with a set of orthonormal polynomials was identical to the fitting with a corresponding set of Zernike polynomials. Also they analyzed the error that arises if Zernike polynomials are used for noncircular pupils by treating them as circular pupils and illustrate it with numerical examples [32].

In 2009, A. Beghi et al. presented algorithms for turbulence compensation in large adaptive optics systems. In this paper, they considered some efficient algorithms for the adaptive optics system of large telescopes. Then, using it in a Kalman-based approach, it provides good performances for the closed-loop system. The proposed Kalman-based model ensures a good tradeoff between complexity and performances [33].

In 2010, J. H. Allen presented an orthogonality and convergence of discrete Zernike polynomials. The Zernike polynomials are an infinite set of orthogonal polynomials over the unit disk, which are rotationally invariant. The analysis concludes with design criteria for computing an accurate analysis with the discrete Zernike polynomials [34].

1.6 Aim of Book

The aim of work is searching for the optimal shape of the optical telescope's aperture, utilizing mirror segmentation techniques. Also, describing the incident and the reflected perturbed wavefront from the aperture of the telescope to the focal plane. Then, using an adaptive optics technique to compensate the perturbed wavefront to be corrected and flattened by modifying the deformable mirror surface.

1.7 Book Layout

The remainder of book will be structured as follows:

1- ***Chapter one*** present a general introduction that includes the problem of interest, and the literature survey that tackles the problem.

2- Theoretical background, Diffraction Theory and Aberration Theory, Two-Mirror Telescope, Resolution of Telescope, Telescope Limiting Magnitude, Imaging through Atmospheric Turbulence, Zernike Polynomials and Their Uses in Describing the Wavefront Aberrations, Orthonormal Polynomial for Hexagonal Apertures and Strehl Ratio are presented in ***chapter two***.

3- ***Chapter three*** contains adaptive optics and their applications.

4- ***Chapter four***, this chapter is dedicated to the simulation of telescope's aperture configurations and analysis the problem, many involved parameters were studied. Also, adaptive optics framework of the developed model was illustrated.

5- ***Chapter five*** contains the main derived conclusions and some stimulated suggestions future works.

Chapter Two

Theoretical Background

2.1 Introduction

In this chapter, some of the related theoretical topics are presented. When a telescope focuses an image from the sky, it deals with the ray and the wave nature of light. A correct optical figure in the telescope optics produces an image free of aberrations. However, the wave nature causes diffraction of light in the telescope, which leads to limit the resolution that can be achieved *(diffraction limit)* [6].

When the telescope focuses a point source, the image at the focal plane is the Point Spread Function (PSF), which, due to diffraction is not dimensionless of a point anymore, but a complex irradiance pattern that depends on the size and shape of the telescope aperture. Given that the point source accounts for all possible spatial frequencies, so a point source in the spatial domain can be decomposed into components with individual spatial frequencies. This is equivalent to the Fourier transform of a Dirac delta, which has components at all frequencies and with the same magnitude. This is why the PSF represents the response of the system; since it shows how an optical system responds to all possible frequencies [35].

In practice, however, both atmospheric and telescope errors distort the spherical wavefront, creating phase errors in the image-forming ray paths. Even at the best sites, ground-based telescopes observing at visible wavelengths cannot achieve an angular resolution better than telescopes of (10-20) cm diameter, because of atmospheric turbulence alone. For a 4m telescope, atmospheric distortion degrades the spatial resolution by more than one order of magnitude compared with the diffraction limit, and the intensity at the center of the star image is lowered by a factor of 100 or more. The cause is random spatial and temporal wavefront perturbations induced by turbulence in various layers of the atmosphere; one of the principal reasons for flying the Hubble Space Telescope was to avoid this image smearing. In addition, image quality is affected by permanent manufacturing errors and by long time scale-wavefront aberrations introduced by mechanical, thermal, and optical effects in the telescope, such as defocusing, decentering, or mirror deformations generated by their supporting devices [36].

2.2 Diffraction Theory and Aberration

The telescopes and their aberrations can be discussed entirely from the point of view of geometrical optics. Geometrical optics *(ray optics)* is concerned with the light

ray, an entity that does not exist which carries energy. It is customary, therefore, to begin discussions of *ray optics* with a theoretical justification for the use of the ray [6].

Rays propagate in straight lines in homogeneous media and have curved paths in heterogeneous media. Rays is used to predict positions, and directions of light. Ray paths are reversible. The paths of rays through an optical system are governed by Fermat's principle. Aberrations occur when rays do not pass through the paraxial image point. An aberration-free image in the *ray optics* limit is, according to Fermat's principle, a true point image. That the wave nature of light sets the image size for an otherwise perfect or diffraction-limited optical system, with the analysis there intended only to give an estimate of the size of the diffraction image [17].

In this work the emphasis is on the character of the perfect image from the point of view of diffraction theory. Because no optical system is strictly perfect, the effect of aberrations of a nearly perfect optical system on the diffraction image is also considered. This analysis proceeds along two lines. The starting point is Huygens' Principle and the superposition of waves from points on a wavefront. The second analysis is in terms of transfer functions.

As part of the discussion of the nearly-perfect image, the representation of its characteristics in terms of transverse aberrations is generalized by introducing orthogonal aberrations in terms of Zernike polynomials. With this representation an image quality in terms of Root Mean Square (RMS) wavefront error is especially informative.

Before discussing the nature of a perfect image as formed by a telescope with a circular or any shape aperture, Huygens' Principle will be discussed and its extension by Fresnel. This principle is the basis for diffraction theory.

2.3 Huygens- Fresnel Principle

The initial statement of Huygens' Principle was made in an attempt to understand the laws of reflection, refraction, and the propagation of light. It started with the assumption that light was a wave and could be described in terms of wavefronts. From the point of view of Fermat's principle, a wavefront is the locus of all points having the same optical path from a point source of light. Viewed as a wave, a wavefront is the locus of all points having the same phase [37]. Huygens postulated that each point on a primary wavefront acts as a secondary source for producing spherical wavelets, and that the envelope of these wavelets at a slightly later time is the new wavefront. He further stated that the new wavefront propagates with a speed and frequency equal to that of the primary wave as shown in figure (2.1). [6]

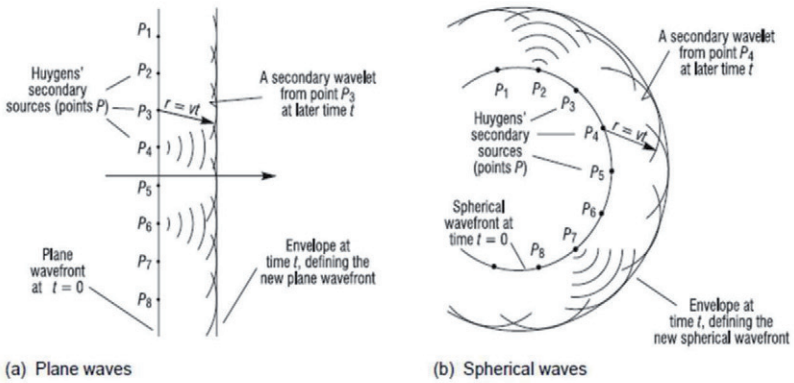

Figure (2.1): Huygens-Fresnel diffraction [6].

This statement suffices to account for the laws of reflection and refraction, and the approximately straight line propagation of light through large apertures, but it fails to account for diffraction, the deviations from exact straightline propagation of light. Fresnel extended Huygens' Principle by assuming that the secondary wavelets interfere with one another according to the principle of superposition. His statement postulated that each unobstructed point on a wavefront is a source of spherical wavelets, and that the amplitude of the wave at any point ahead of the wavefront is the superposition of all of these wavelets. In adding these wavelets it is necessary to include the amplitude and phase of each wavelet. The Huygens-Fresnel principle was put on a firm theoretical basis by Kirchhoff and expressed as an integral called Fresnel-Kirchhoff diffraction integral derived from the wave equation, in this research only the special case of *Fraunhofer diffraction* is used, in which the source of light and the field are effectively at infinity relative to the aperture. Thus the image of a star formed by a telescope or, equivalently, the converging spherical wave diffracted by the exit pupil of the telescope, is a Fraunhofer diffraction pattern [5].

2.4 Two-Mirror Telescope

In astronomy, most telescopes are two-mirror telescopes such as Newtonian, Cassegrain, or Gregorian design. All three types have a concave primary. The Newtonian has a flat secondary, the Cassegrain a convex secondary, and the Gregorian

a concave secondary as shown in figure (2.2). The Cassegrain is the most common for research astronomy; it is more compact than a Gregorian and allows for magnification by the secondary.

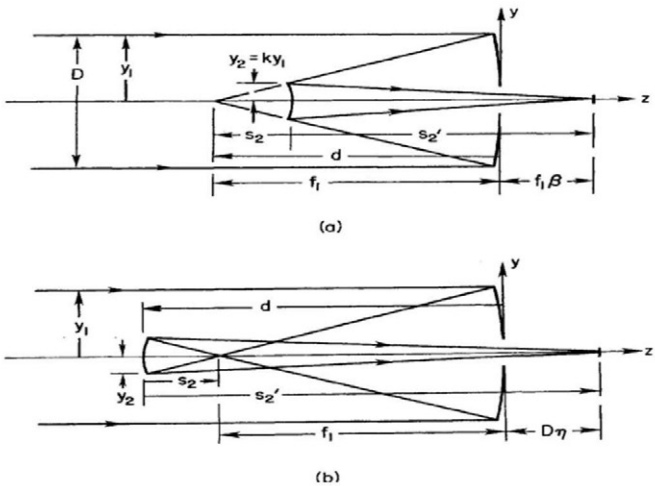

Figure (2.2): Schematic Diagrams of Two-mirror Reflecting Telescopes: (a) Cassegrain; (b) Gregorian [1].

From figure (2.2) the normalized parameters for two-mirror telescope can be written as basic definitions [6]:

$k = y_2/y_1$ = ratio of ray heights at mirror margins

$\rho = R_2/R_1$ = ratio of mirror radii of curvature

$m = -S'_2/S_2$ = transverse magnification of secondary

$f_1\beta = D\eta$ = back focal distance, or distance from vertex of primary mirror to final focal point

β and η, back focal distance in units of f_1 and D, respectively.

$F_1 = |f_1|/D$ = primary mirror focal ratio

$W = (1 - k) f_1$ = distance from secondary to primary mirror

= location of telescope entrance pupil relative to the secondary when the primary mirror is the aperture stop.

$F = f/D$ = system focal ratio, where f is the telescope focal length

Basic parameters are outlined here. Each of these telescope types defines a *family* of telescopes with different first-order performances. From the usage/instrumentation point of view, the important quantities are [6][63]:

- the diameter of the primary, which defines the light collecting power
- the scale of the telescope, which is related to the focal length of the primary (f_1) and the magnification of the secondary[63]:

$$f_{\text{eff}} = f_1 m \ldots\ldots (2.1)$$

- the back focal distance, which is the distance of the focal plane behind the telescope

From the design point of view, the following parameters are needed to be specified:

- the radii of curvature of the mirrors
- the separation between the mirrors

Using some geometry, some basic relations between these quantities cab be derived, in particular [6]:

$$\rho = \frac{mk}{(m-1)} \ldots..(2.2)$$

and

$$(1+\beta) = k(m+1) \ldots..(2.3)$$

Usually, f_1 is limited by technology. m is chosen to match desired scale. k is related to separation of mirrors, and it is a compromise between making telescope shorter and blocking out more light vs. longer and blocking less light; in either case, focal plane has to be kept behind primary. One final thing to note is how to focus a Cassegrain telescope. Most instruments are placed at a fixed location behind the primary. Ideally, this will be at the back focal distance, and everything should be set as designed. However, sometimes the instrument may not be exactly at the correct back focal distance, or it might move slightly because of thermal expansion/contraction. In this case, focusing is usually then done by moving the secondary mirror. The amount of image motion for a given secondary motion is given by [6]:

$$\frac{d\beta}{dk} = \frac{d}{dk} k(m+1) - 1 \ldots..(2.4)$$

Working through the relations above, this gives:

$$\frac{d\beta}{dk} = m^2 + 1 \ldots..(2.5)$$

So the amount of focal plane motion ($f_1 d\beta$) for a given amount of secondary motion ($f_1 dk$) depends on the magnification of the system. If the secondary is moved then k is changed. Since ρ is fixed by the mirror shapes, it's also clear that the magnification is changed as the secondary is moved; this is expected since the system focal length, $f =$

mf_1 is changed. So it's possible that a given instrument could have a slightly varying scale if its position is not perfectly fixed relative to the primary.

2.5 Definitions for Multi-Surface System: Stops and Pupils

The following parameters can be defined from figure (2.3) as follows:

- **Aperture stop:** determines the amount of light reaching an image (usually the primary mirror).
- **Field stop:** determines the angular size of the field. This is usually the detector, but for a large enough detector, it could be the secondary.
- **Pupil:** location where rays from all field angles fill the same aperture.
- **Entrance pupil:** image of aperture stop as seen from object source (usually the primary).
- **Exit pupil:** image of aperture stop formed by all subsequent optical elements [38].

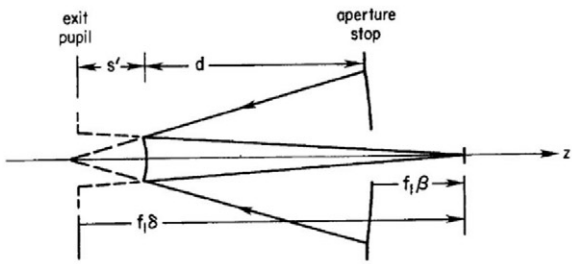

Figure (2.3): Location of Exit Pupil for Cassegrain Telescope. The Exit Pupil is closer to the Secondary than is the Primary Focal Point [6].

In a two-mirror telescope, the location of the exit pupil is where the image of the primary is formed by the secondary. This can be calculated using S(the object distance) = d (the separation of the mirrors), then with the reflection equation, the location of the exit pupil relative to the secondary mirror S' can be found. If one defines the quantity δ , such that $f_1\delta$ is the distance between the exit pupil and the focal plane, then [6]:

$$\delta = \frac{m^2}{m+k-1} = \frac{m^2(1+\beta)}{m^2+\beta} \quad \text{.....(2.6)}$$

The exit pupil is an important concept, when discussing aberrations; it is the total wavefront error at the exit pupil which gives the system aberration.

2.6 Telescope Resolution

Fraunhofer modeled the irradiance distribution (***E***) of light caused by diffraction for a circular aperture, which is true in the case of telescopes. ***E*** can be described as a pattern of irradiance in the focal plane by a Bessel function of the first order J_1 [5][41]. The mathematical expression, also called the Airy pattern, is [39]:

$$E(r) = E_A\left(\frac{A}{\lambda f}\right)^2\left[\frac{2J_1\left(\frac{\pi r D}{\lambda f}\right)}{\frac{\pi r D}{\lambda f}}\right] \text{.....(2.7)}$$

Where: *E(r):* is the irradiance intensity at a distance *r* from the optical axis

E_A*:* is the irradiance at the aperture

λ*:* is the wavelength of light under study

D: diameter of the telescope

A: area of the aperture

f: focal length

An irradiance pattern for the case of an 8-m telescope (This is an example of a single mirror telescope working at f/no = 15 and without secondary mirror is presented in figure (2.4) the first ring occurs at [5]:

$r \cong \frac{1.22\lambda f}{D}$, this is $r = \pm 9.15$ μm

The ability of an optical system to image two separate point sources at its focal plane is function to its diameter. Lord Rayleigh defined a criterion for the resolution limit of the telescope, which is related to the first ring of the PSF. The expression for the angular resolution is then [41]:

$$\Delta\theta = \frac{1.22\lambda}{D}(rad) = \frac{251542\lambda}{D}(arc\,\text{sec}) \text{.....(2.8)}$$

Two PSFs having the distance separation of Eq. (2.8) are presented in figures (2.4, 4.5) this is an upper limit in terms of the resolving power of the telescope that can be achieved. In the next section, atmospheric turbulence limitation to the resolution of any ground-based optical telescope will be shown to be equal to a few tens of centimeters at best.

Figure (2.6) shows the Improvement in angular resolution at optical wavelengths. The development of adaptive optics has permitted diffraction-limited observations from ground-based observatories since 1990, largely eliminating the effects of the atmosphere. The dashed line shows the theoretical diffraction-limited resolution for the telescope. The solid line shows the seeing limit imposed by the atmosphere. Improvements were obtained by going to very good seeing sites [3].

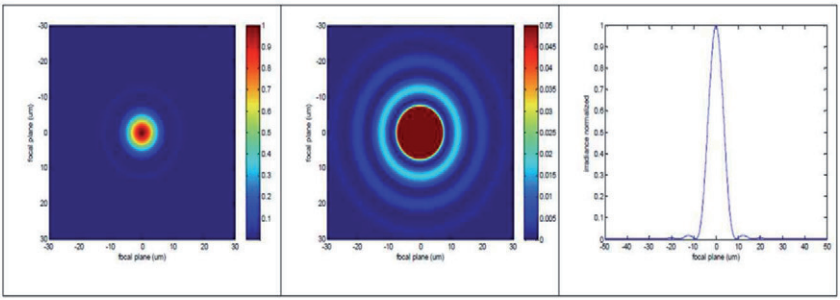

Figure (2.4): Diffraction-Limited Irradiance Pattern produced by an 8-m telescope at its Nasmyth focus (with F-ratio = 15), for wavelength = 500 nm. Left panel: Airy disk with linear color scale. Central panel: scale adjusted to see the rings. Right panel: slice of the Airy disk through the origin.

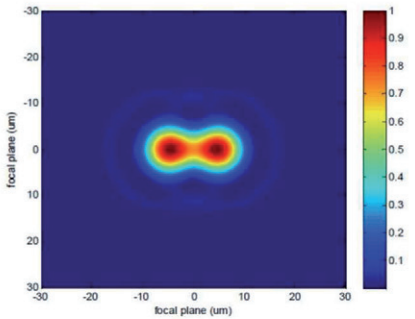

Figure (2.5): Rayleigh Resolution Criterion, illustrated for two point sources on an 8m telescope working at F-ratio = 15 and 500 nm wavelength.

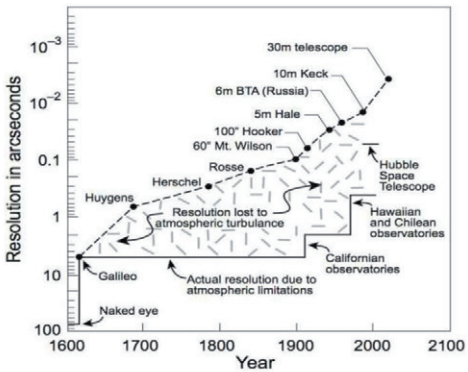

Figure (2.6): Historical improvement in angular resolution at optical wavelengths [3].

2.7 Telescope Limiting Magnitude

The apparent magnitude is the degree of brightness of a celestial body designated on a numerical scale, on which the brightest star has magnitude -1.4 and the faintest visible star has magnitude 6, with scale rule such that a decrease of one unit represents an increase in apparent brightness by a factor of 2.512 as shown in figure (2.7).

Any star that is 2.512 times brighter than a 6th magnitude star is said to have a 5th magnitude. Notice that a magnitude with a large number is dimmer than another with a small number. The number 2.512 is not any number taking at random. 2.512 happen to be a number whose logarithm is 0.4. The reason for using logarithms is fundamental. Our eyes and all our senses respond logarithmically. Mathematically the apparent magnitude can be represented as [40]:

$$m = -2.5\log_{10}(I) + c \text{.....(2.9)}$$

Where:
(I) represents the observed intensity and (c) is a constant.

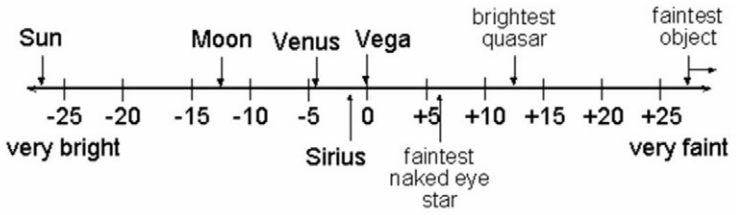

Figure (2.7): Apparent Brightness of Some Objects in the Magnitude System [40].

ess) of the faintest star that can be seen with a telescope. An approximate formula for determining the visual limiting magnitude of a telescope is [41]:

$$LM = 7.5 + 5\log_{10}(D) \text{.....(2.10)}$$

Where D is diameter of the aperture of the telescope in cm.

Keeping in mind that this formula does not take into account light loss within the telescope, seeing conditions, the observer's age (visual performance decreases as the observer got older), the telescope's age (the reflectivity of telescope's mirrors decreases as they got older), etc... The limiting magnitudes specified by manufacturers for their telescopes assume very dark skies, trained observers, and excellent atmospheric transparency and are therefore, rarely obtainable under average observing conditions.

2.8 Imaging through Atmospheric Turbulence

In the following, the relevant theoretical framework for understanding imaging through atmospheric turbulence will be discussed.

Preliminaries

The wave propagation through the atmosphere and the telescope into the focal plane is conveniently described by diffraction theory. Incorporating optical elements like lenses or mirrors in a spherical approximation leads to the well-known Fourier relationship between the amplitude of the electromagnetic wave in the pupil of the telescope and the amplitude in its focal plane. Using the notation $\psi(\vec{x})$ for the complex amplitude in the telescope pupil and $A(\vec{u})$ for the complex amplitude in the focal plane. The two quantities are connected through a Fourier transform where the integration is performed over the telescope pupil. The phase $\varphi(\vec{x})$ of $\psi(\vec{x})$ incorporates the turbulent atmosphere as well as the telescope aberrations. In the telescope focus, the intensity distribution $I(\vec{u}) = |A(\vec{u})|^2$ is usually used and can be written as [17]:

$$I(\vec{u}) = \iint \psi(\vec{x}')\psi^*(\vec{x}'')\exp\left(2\pi i(\vec{x}'-\vec{x}'')\vec{u}\right)d\vec{x}'d\vec{x}''$$

$$I(\vec{u}) = \int\left(\int \psi(\vec{x}')\psi^*(\vec{x}'-\vec{x})d\vec{x}'\right)\exp\left(2\pi i\vec{x}\vec{u}\right)d\vec{x} \quad \text{.....(2.11)}$$

Where $\int \psi(\vec{x}')\,\psi^*(\vec{x}'-\vec{x})d\vec{x}'$ is the autocorrelation of the amplitude in the telescope pupil that is called the optical transfer function (OTF) as shown in figure (2.8). If a plane wave from a point source at infinity enters a perfect, i.e. aberration free telescope the OTF is a purely real function – approximately shaped like a triangle – and its Fourier transform is the diffraction limited point spread function, the Airy disk. In the case of statistical fluctuations of the electromagnetic wave, due to an incoherent source or due to atmospheric turbulence, the autocorrelation can be expressed as an ensemble average over all possible realizations, called the coherence function [17]:

$$\Lambda(\vec{x}) = \left\langle \psi(\vec{x}')\psi^*(\vec{x}'-\vec{x})\right\rangle \text{.....(2.12)}$$

It is one of the main tasks of turbulence theory to connect the atmospheric properties to the coherence function in the telescope pupil and, thus, to its Fourier transform, the PSF in the telescope focal plane. If atmospheric turbulence rather than the telescope diameter limits the size of the PSF it is called the seeing disk and its full width at half maximum (FWHM) is called the *seeing condition* [6].

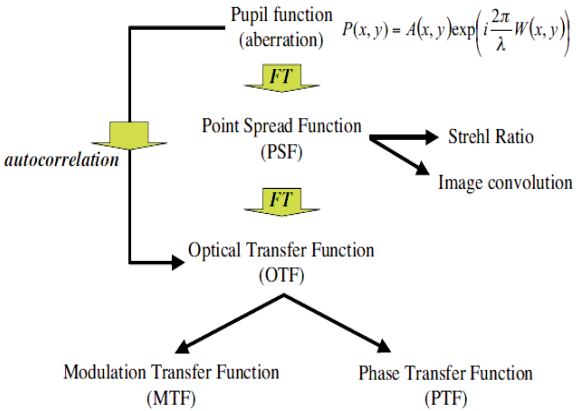

Figure (2.8): Aberration vs. Image Quality

2.9 Atmospheric Turbulence

In this section a short overview of the theoretical background for the generation of turbulence in the atmosphere, and the wavefront deformation is given. To assess the turbulent behavior, one first needs to characterize the medium under investigation, based on the theory of fluid flows, using the Reynolds number (R_n) defined as [42]:

$$R_n = \frac{VL}{\nu} \text{.....(2.13)}$$

Where V is the velocity, L is a characteristic scale length and $\boldsymbol{\nu}$ the kinematic viscosity.

The Reynolds number is a measure of the ratio between the inertial forces and the viscous forces of the fluid. If the Reynolds number is high, the motion on the scale L is undampened, as viscosity plays no dominant role. When the Reynolds number becomes of the order of 1, the influence of viscosity becomes high enough that energy can be dissipated. L is set by the outer geometry of the flow, and the Reynolds number can be interpreted as the ratio between this length and the structure size at which the energy is dissipated. For atmospheric flows, $R_n \geq 10^6$. They can be always considered turbulence. The transfer of energy between the large scale and the dissipative scale can be explained as follows:

The turbulence in the atmosphere is introduced by large eddies of a scale L_0. These eddies cannot dissipate, as indicated by the Reynolds number, but break up in a hierarchical cascade to smaller and smaller eddies, until they reach inner scale l_0, and the turbulent energy is dissipated. The range between l_0 and L_0 is called the inertial range; L_0 is called the outer scale of the turbulence.

Also, the turbulence in the atmosphere is the result of mixing of air at different temperatures, which occurs through the solar heating during the day. Having a mix of air molecules at different temperatures, the air density is constantly changing in a random fashion, which in turn produces a change in the index of refraction of the air. Light coming from stars is slightly refracted by the atmosphere, producing degradation in the resolution of the image. Atmospheric turbulence at observatories had been extensively studied in the last decade, indicating that the turbulence is mostly limited to thin layers within the first 15 km of atmosphere above the observatory [2].

Figure (2.9) shows this effect at Cerro Paranal in Chile, where the VLT is located. The figure is a kinetic energy plot with respect to altitude above the telescope. The two distinctive peaks are from the two strong turbulent layers, one directly above the telescope (the ground layer) and the second about 8 km from altitude. Turbulent layers represent about two-thirds of the total turbulence, but there is one-third that is distributed along the whole column of turbulence.

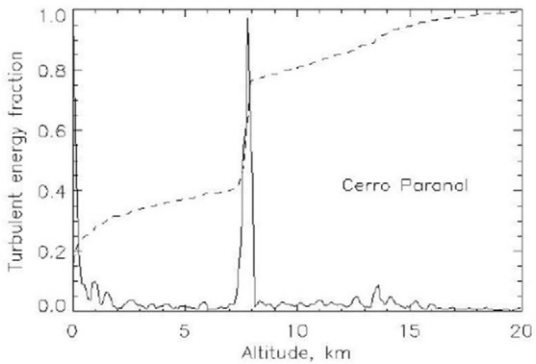

Figure (2.9): Turbulence Profile at Cerro Paranal in Northern Chile. The solid line represents the turbulence energy (in normalized units) and the segmented line is the accumulated energy. Plot courtesy A. Tokovinin (CTIO).

The most notable effect of a turbulent atmosphere is a blurred image in the focal plane of a telescope. For a large telescope the image size, often called the seeing disk, is usually larger than the diffraction disk. The angular radius of the Airy disk and the limit of resolution $\Delta\theta$, from Eq. (2.8), can be written as [6]:

$$\Delta\theta(arc\sec) = \frac{0.25\lambda(\mu m)}{D(m)} \quad \text{.....(2.14)}$$

If the radius (a) of the seeing disk is 0.5 arcsec and $\lambda = 0.5$ μm, then $a = \Delta\theta$ for a 25 cm telescope. Thus for the visible wavelengths and 1m or larger telescopes, the image size is determined by atmospheric effects. Because $\Delta\theta \prec \frac{\lambda}{D}$, the seeing disk may be comparable to the diffraction disk at infrared wavelengths for large telescopes. Especially, at the longest wavelengths that reach the ground.

2.10 Seeing and Scintillation

The effect of atmospheric turbulence on stellar images is usually separated into two distinct phenomena; *Seeing* is the term used to describe random changes in the direction of light entering a telescope, while *Scintillation* refers to random fluctuations in the intensity [6]. Both of these effects arise from variations in the index of refraction and give rise to a distorted wavefront. A cross section of such a wavefront reaching the ground at a given instant of time is shown schematically in the figure (2.10). The corruption effect of seeing and scintillation on a stellar image as observed with the eye will be described first. Scintillation is most evident to the unaided eye as the phenomenon called "twinkling".

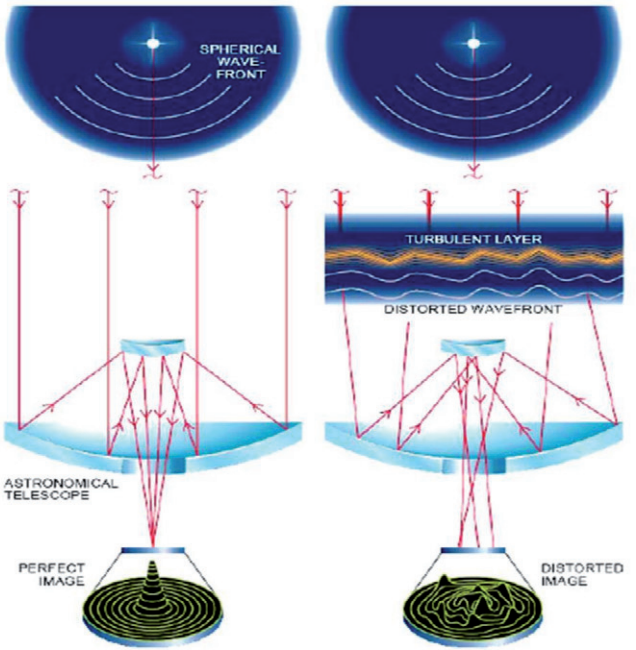

Figure (2.10): Perfect Image versus Distorted Image Due to Atmospheric Turbulence [17].

In a telescope the twinkling couldn't usually be seen, and a photometer is needed to record the fluctuations in intensity. In general, the larger aperture is the smaller fractional changes in the intensity.

The effect of seeing is function to the telescope aperture. In good seeing, with a 10 cm aperture or less, the Airy disk of a star moves randomly about its mean position in the focal plane with excursions of 1 or 2 arcsec. In a large telescope, 1 m or larger, a blurred image is seen with little or no motion of the image as a whole. If the eye could follow the rapid changes within the image, it would see a changing pattern of speckles, each speckle having a size comparable to an Airy disk. A given speckle pattern is stationary over time of an order of 10-50 millisec, with two patterns similar only for point sources within about 10 arcsec of one another.

From these observations it can be deduced that the curvature of the wavefront is negligible over distances of the order of 10 cm, with instantaneous slopes of 1 or 2 arcsec from an undistorted wavefront. The image seen in a large telescope is thus the average over many sections of the wavefront, each with a different instantaneous slope. For short exposures these fluctuating aberrations will cause the light to scatter and form a **speckle pattern** in the image plane as seen in Figures (2.11, 2.12, 2.13), where the individual speckles are diffraction-limited [44].

Figure (2.11): Diffraction-limited PSF of an 8 m telescope at a wavelength of 1000 nm with 0.65" seeing.

Figure (2.12): Speckle pattern of an 8 m telescope at a wavelength of 1000 nm with 0.65" seeing.

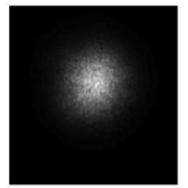

Figure (2.13): Seeing disk of an 8 m telescope at a wavelength of 1000 nm with 0.65" seeing.

The most commonly used model for atmospheric turbulence was proposed by Kolmogorov (1941) and developed by Tatarski (1961). This model is general for turbulence in a fluid medium, in which the turbulence is a consequence of adding energy to the medium in large spatial scales: solar heating in the case of atmospheric turbulence.

Kolmogorov developed a theory that allows us to assess the turbulent behavior on different scales over the inertial range, that is, to calculate the power spectrum. His result shows that the spectrum has a universal form, and the calculations can be easily

retraced. A good way to describe the turbulence as a function of position is a structure function.

2.11 Kolmogorov Model

The Kolmogorov model describes the turbulent behavior between the "outer scale" L_0 and the "inner scale" l_0. The former corresponds to the scale where energy is added to the medium (usually tens of meters), while the latter occurs when the energy is finally dissipated as heat by viscous friction (within millimeters).

Atmospheric turbulence is a random process. It can be modeled with the structure function $D_n(\Delta x)$, defined as the average difference between two values of a random variable for a large number of points, with the random variable being the index of refraction *n(x)*, i.e. [35]:

$$D_n(\Delta x) = \left\langle \left[n(x) - n(x') \right]^2 \right\rangle \text{.....(2.15)}$$

The structure function for the refractive index variation of turbulent air in the Kolmogorov model is [45]:

$$D_n(\Delta x) = C_n^2(h)\Delta x^{2/3} \qquad l_0 \langle \Delta x \langle L_0 \text{.....(2.16)}$$

$C_n^2(h)$ is the vertical refractive index structure parameter, which is function of the altitude *h*.

The vertical refractive index structure parameter $C_n^2(h)$ is a measure of the strength of the fluctuations in the refractive index. The values of C_n^2 is typically in the range from 10^{-17}m$^{-2/3}$ or less for conditions of "weak turbulence" and up to 10^{-13} m$^{-2/3}$ or more when the turbulence is "strong".

Developed from this model, the *Fried* parameter r_0 allows one to characterize the strength of the whole atmosphere (Fried 1965). The mathematical expression for r_0 is [46]:

$$r_0 = \left[0.423 \left(\frac{2\pi}{\lambda} \right)^2 (\sec\zeta) \int C_n^2(h)\, dh \right]^{-3/5} \text{.....(2.17)}$$

Where

ζ is the zenith angle of observation.

λ is the observational wavelength.

The effect of turbulence on a telescope of diameter D is seen on the variance of the wavefront σ_ϕ^2 which can be computed as:

$$\sigma_\phi^2 = 1.0299 \left(\frac{D}{r_0} \right)^{5/3} .....(2.18)$$

Alternatively, one can use the resolution $\Delta\theta$ of the telescope in the presence of turbulence.

$$\Delta\theta = \frac{1.22\ \lambda}{r_0} .....(2.19)$$

The main interpretation of Eq. 2.19 and its similarity with Eq. 2.8 is straight forward: in the presence of turbulence, the resolution is set by the parameter r_0, which represents the diameter of a telescope that produces the same resolution. Typical values for the *Fried* parameter are $5cm < r_0 < 20cm$.

For example the diffraction limit of resolution for 4m telescope at 500 nm is given by equation [43]:

$$\Delta\theta = \frac{1.22\lambda}{D} = 1.52\,X\,10^{-7}\ rad$$

The angular resolution due to atmospheric turbulence is:

$$\Delta\theta = \frac{1.22.\lambda}{r_0} = 0.6X10^{-5}\ rad$$

So turbulence in this case degrades the resolution by a factor of 100.

When a telescope of such a diameter is used, only the first order of the turbulence, i.e. the wavefront gradient or “tip and tilt” needs to be compensated for achieving the diffraction limit. An alternative physical interpretation for the *Fried* parameter is that r_0 is the aperture size that produces a mean square wavefront error of around 1 rad^2. To quantify the relationship between the phase aberrations and the image quality the Strehl ratio is used.

2.12 Power Spectrum Models

For optical wave propagation, refractive index fluctuations are caused almost by small fluctuations in temperature. One well-known power spectrum model is *Kolmogorov* spectrum [45]:

$$\phi_n(K) = 0.033C_n^2 \times K^{-11/3} \qquad 1/L_0 \ \langle\ K \ \langle\ \ 1/l_0 .....(2.20)$$

K is the transverse wave number, l_0 and L_0 are the inner and outer scales of the turbulence, respectively.

There are also other models of spectrum for refractive index fluctuations, such as V*on Kármán* spectrum [46]:

$$\phi_n(K) = 0.033C_n^2 \times \exp\left[-\left(\frac{Kl_0}{2\pi}\right)^2\right]\left(K^2 + \left(\frac{2\pi}{L_0}\right)^2\right)^{-11/6} \quad \text{.....(2.21)}$$

This spectrum regards both inner scale and outer scale parameters inside the spectrum which is more appropriate for calculation of beam through atmosphere with turbulence presence.

2.13 Zernike Polynomials and their use in Describing the Wavefront Aberrations

The objectives of this section include an explanation of why Zernike polynomials are preferred over other functions, a mathematical definition of Zernike polynomials, and their use in describing the wave aberration function. Simulation shows the effects of the low and high order aberrations on image quality; and an illustration of how Zernike polynomials are used to estimate the wave aberration function from measurement data.

2.14 Why Using Zernike Polynomials?

Optical system aberrations have historically been described, characterized, and catalogued by power series expansions, where the wave aberration is expressed as a weighted sum of power series terms that are functions of the pupil coordinates. Each term is associated with a particular aberration or mode. For example, spherical aberration, coma, astigmatism, field curvature, distortion, and other higher order modes [56].

Many optical systems have circular pupils. So many analyses and calculations (e.g. diffraction) will involve the integration of the pupil function and wave aberration function over a circular pupil. Experimental measurements will also be performed over a circular pupil and will commonly require some form of data fitting. It is, therefore, convenient to expand the wave aberration in terms of a complete set of basis functions that are orthogonal over the interior of a circle. Experimental data can be fitted to a weighted sum of these orthogonal basis functions [71].

Zernike polynomials form a complete set of functions or modes that are orthogonal over a circle of unit radius and are convenient for serving as a set of basis functions. This makes them suitable for accurately describing wave aberrations as well as for data fitting. They are usually expressed in polar coordinates, and are readily convertible to Cartesian coordinates. These polynomials are mutually orthogonal, and are therefore mathematically independent, making the variance of the sum of modes equal to the sum of the variances of each individual mode. They can be scaled so that

non-zero order modes have zero mean and unit variance. This puts all modes in a common reference frame that enables meaningful relative comparison between them.

Different Zernike polynomial definitions are currently in use. The convention adopted has x "horizontal", y "vertical", and θ is measured counter-clockwise from x-axis (i.e. right-handed coordinate system). More traditional notation measures θ clockwise from y-axis.

There is the orthogonal type where the polynomials are normalized to have unit magnitude at edge pupil. There is also the Orthonormal type where the terms are normalized so that the coefficient of a particular term or mode is the RMS contribution of that term.

2.15 Standard Set of Zernike Polynomials

Zernike polynomials are normally expressed in polar coordinates (ρ,θ) where $0 \leq \rho \leq 1$, $0 \leq \theta \leq 2\pi$.

The wave aberration polynomial is typically expressed in terms of the normalized pupil radius [71]:

$\rho = \frac{r}{a}$ where a is the exit pupil radius.

Figure (2-14) shows the coordinate system of the unit circle over which they are defined. Conversion to rectangular coordinates may be desirable for some applications.

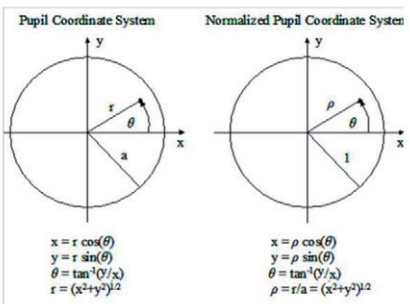

Figure (2.14): Pupil Coordinate Systems

The Zernike polynomials are defined as [52] [53]:

$$Z_n^m(\rho,\theta) = N_n^m R_n^{|m|}(\rho)\cos(m\theta) \quad \text{for } m \geq 0,\ 0 \leq \rho \leq 1,\ 0 \leq \theta \leq 2\pi \qquad \text{……..(2.22)}$$
$$= -N_n^m R_n^{|m|}(\rho)\sin(m\theta) \quad \text{for } m < 0,\ 0 \leq \rho \leq 1,\ 0 \leq \theta \leq 2\pi$$

for a given n: m can only take on values of $-n, -n+2, -n+4, \ldots, n$

N_n^m is the normalization factor ……..(2.23)

$$N_n^m = \sqrt{\frac{2(n+1)}{1+\delta_{m0}}} \qquad \delta_{m0} = 1 \text{ for } m = 0, \quad \delta_{m0} = 0 \text{ for } m \neq 0$$

……..(2.24)

$R_n^{|m|}(\rho)$ is the radial polynomial

$$R_n^{|m|}(\rho) = \sum_{s=0}^{(n-|m|)/2} \frac{(-1)^s (n-s)!}{s!\left[0.5(n+|m|)-s\right]!\left[0.5(n-|m|)-s\right]!} \rho^{n-2s}$$

Each polynomial has three components: the normalization factor, a radially dependent polynomial, and an azimuthally dependent sinusoid. A double indexing scheme is used where: (n) is the highest power or order of the radial polynomial and (m) is the azimuthal or angular frequency of the sinusoidal component. An accompanying single indexing scheme is also employed where the index (j) is used to indicate mode number. Table (2-1) contains a list of Zernike polynomials up to order seven and their meanings relative to the traditional Seidel or Primary aberrations [51][54].

Table (2-1): Algebraic expansion of the Zernike polynomial sequence up to 7th order [56]

n	m	Z_n^m	RMS	Polar form $(dx^2 \to rd\theta dr)$	Cartesian form $(dx^2 \to dxdy)$
0	0	Z_0^0	$\sqrt{2}$	1	1
1	−1	Z_1^{-1}	2	$r\sin\theta$	x
1	1	Z_1^1	2	$r\cos\theta$	y
2	−2	Z_2^{-2}	$\sqrt{6}$	$r^2\sin2\theta$	$2xy$
2	0	Z_2^0	$\sqrt{3}$	$2r^2-1$	$-1+2x^2+2y^2$
2	2	Z_2^2	$\sqrt{6}$	$r^2\cos2\theta$	$-x^2+y^2$
3	−3	Z_3^{-3}	$2\sqrt{2}$	$r^3\sin3\theta$	$-x^3+3xy^2$
3	−1	Z_3^{-1}	$2\sqrt{2}$	$(3r^3-2r)\sin\theta$	$-2x+3x^3+3xy^2$
3	1	Z_3^1	$2\sqrt{2}$	$(3r^3-2r)\cos\theta$	$-2y+3y^3+3x^2y$
3	3	Z_3^3	$2\sqrt{2}$	$r^3\cos3\theta$	y^3-3x^2y
4	−4	Z_4^{-4}	$\sqrt{10}$	$r^4\sin4\theta$	$-4x^3y+4xy^3$
4	−2	Z_4^{-2}	$\sqrt{10}$	$(4r^4-3r^2)\sin2\theta$	$-6xy+8x^3y+8xy^3$
4	0	Z_4^0	$\sqrt{5}$	$6r^4-6r^2+1$	$1-6x^2-6y^2+6x^4+12x^2y^2+6y^4$
4	2	Z_4^2	$\sqrt{10}$	$(4r^4-3r^2)\cos2\theta$	$3x^2-3y^2-4x^4+4y^4$
4	4	Z_4^4	$\sqrt{10}$	$r^4\cos4\theta$	$x^4-6x^2y^2+y^4$
5	−5	Z_5^{-5}	$2\sqrt{3}$	$r^5\sin5\theta$	$x^5-10x^3y^2+5xy^4$
5	−3	Z_5^{-3}	$2\sqrt{3}$	$(5r^5-4r^3)\sin3\theta$	$4x^3-12xy^2-5x^5+10x^3y^2+15xy^4$
5	−1	Z_5^{-1}	$2\sqrt{3}$	$(10r^5-12r^3+3r)\sin\theta$	$3x-12x^3-12xy^2+10x^5+20x^3y^2+10xy^4$
5	1	Z_5^1	$2\sqrt{3}$	$(10r^5-12r^3+3r)\cos\theta$	$3y-12y^3-12x^2y+10y^5+20x^2y^3+10x^4y$
5	3	Z_5^3	$2\sqrt{3}$	$(5r^5-4r^3)\cos3\theta$	$-4y^3+12x^2y+5y^5-10x^2y^3-15x^4y$
5	5	Z_5^5	$2\sqrt{3}$	$r^5\cos5\theta$	$y^5-10x^2y^3+5x^4y$
6	−6	Z_6^{-6}	$\sqrt{14}$	$r^6\sin6\theta$	$6x^5y-20x^3y^3+6xy^5$
6	−4	Z_6^{-4}	$\sqrt{14}$	$(6r^6-5r^4)\sin4\theta$	$20x^3y-20xy^3-24x^5y+24xy^5$
6	−2	Z_6^{-2}	$\sqrt{14}$	$(15r^6-20r^4+6r^2)\sin2\theta$	$12xy-40x^3y-40xy^3+30x^5y+60x^3y^3-30xy^5$
6	0	Z_6^0	$\sqrt{7}$	$20r^6-30r^4+12r^2-1$	$-1+12x^2+12y^2-30x^4-60x^2y^2-30y^4+20x^6+60x^4y^2+60x^2y^4+20y^6$
6	2	Z_6^2	$\sqrt{14}$	$(15r^6-20r^4+6r^2)\cos2\theta$	$-6x^2+6y^2+20x^4-20y^4-15x^6-15x^4y^2+15x^2y^4+15y^6$
6	4	Z_6^4	$\sqrt{14}$	$(6r^6-5r^4)\cos4\theta$	$-5x^4+30x^2y^2-5y^4+6x^6-30x^4y^2-30x^2y^4+6y^6$
6	6	Z_6^6	$\sqrt{14}$	$r^6\cos6\theta$	$-x^6+15x^4y^2-15x^2y^4+y^6$
7	−7	Z_7^{-7}	4	$r^7\sin7\theta$	$-x^7+21x^5y^2-35x^3y^4+7xy^6$
7	−5	Z_7^{-5}	4	$(7r^7-6r^5)\sin5\theta$	$-6x^5+60x^3y^2-30xy^4+7x^7-63x^5y^2-35x^3y^4+35xy^6$
7	−3	Z_7^{-3}	4	$(2r^7-30r^5+10r^3)\sin3\theta$	$-10x^3+30xy^2+30x^5-60x^3y^2-90xy^4-21x^7+21x^5y^2+105x^3y^4+63xy^6$
7	−1	Z_7^{-1}	4	$(35r^7-60r^5+30r^3-4r)\sin\theta$	$-4x+30x^3+30xy^2-60x^5-120x^3y^2-60xy^4+35x^7+105x^5y^2+105x^3y^4+35xy^6$
7	1	Z_7^1	4	$(35r^7-60r^5+30r^3-4r)\cos\theta$	$-4y+30y^3+30x^2y-60y^5-120x^2y^3-60x^4y+35y^7+105x^2y^5+105x^4y^3+35x^6y$
7	3	Z_7^3	4	$(2r^7-30r^5+10r^3)\cos3\theta$	$10y^3-30x^2y-30y^5+60x^2y^3+90x^4y+21y^7-21x^2y^5-105x^4y^3+63x^6y$
7	5	Z_7^5	4	$(7r^7-6r^5)\cos5\theta$	$-6y^5+60x^2y^3-30x^4y+7y^7-63x^2y^5-35x^4y^3+35x^6y$
7	7	Z_7^7	4	$r^7\cos7\theta$	$y^7-21x^2y^5+35x^4y^3-7x^6y$

ı figure
is also

There are occasions when expressing the Zernike polynomials in rectangular form. For example, data from the Shack-Hartmann Wavefront Sensor represent the partial derivatives of the wave aberration as a function of x and y. The formulas for conversion to rectangular coordinates and the various indices are provided as follows [55]:

Zernike Polynomials can be converted to rectangular form:

$$Z_n^m(\rho,\theta) \Rightarrow Z_n^m(x,y)$$

by using the following coordinate transformations and trigonometric identities:

$$x = \rho\cos(\theta)$$
$$y = \rho\sin(\theta)$$
$$\rho = \sqrt{x^2 + y^2}$$
$$\cos(m\theta) = 2\cos[(m-1)\theta]\cos(\theta) - \cos[(m-2)\theta]$$
$$\sin(m\theta) = 2\sin[(m-1)\theta]\cos(\theta) - \sin[(m-2)\theta] \quad \text{...(2.25)}$$

Zernike Polynomials can also be specified by the single indexing scheme:

$$Z_j(\rho,\theta) = Z_n^m(\rho,\theta)$$

where

$$j = \frac{n(n+2)+m}{2} \qquad \text{n} = \text{roundup}\left[\frac{-3+\sqrt{9+8j}}{2}\right] \qquad m = 2j - n(n+2)$$

2.16 Describing Wave Aberration Function Using Zernike Polynomials

The wave aberration function is expressed as a weighted sum of Zernike polynomials [57][58]:

$$W(\rho,\theta) = \sum_{n}^{k}\sum_{m=-n}^{n} W_n^m Z_n^m(\rho,\theta) = \sum_{n}^{k}\left\{\sum_{m=-n}^{-1} W_n^m(-N_n^m R_n^{|m|}(\rho)\sin(m\theta)) + \sum_{m=0}^{n} W_n^m(N_n^m R_n^{|m|}(\rho)\cos(m\theta))\right\} \quad (2.26)$$

k is the polynomial order of the expansion

W_n^m is the coefficient of the Z_n^m mode in the expansion

W_n^m is equal to the rms wavefront error for that mode

For computational purposes it may be more convenient to express the wave aberration in rectangular coordinates and use the single indexing scheme:

$$W(x,y) = \sum_{j=0}^{j\max} W_j Z_j(x,y) \quad \text{where } W_j = W_n^m \text{ and } Z_j(x,y) = Z_n^m(x,y) \qquad j = \frac{n(n+2)+m}{2} \quad (2.27)$$

j max refers to the highest mode number included in the expansion

2.17 General Optical System Description

Figures (2.16, 2.17) represent the general form of the optical system.

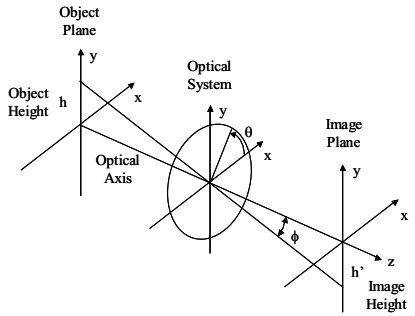

Figure (2.16): Coordinate System [47]

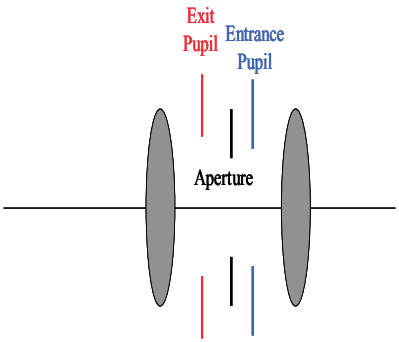

Figure (2.17): Optical System Components [49]

Note that the light forming the image completely fills the exit pupil. Also, since the exit pupil is the aperture as seen from the image space of the optical system, all of the effects of aberrations in the system are fully contained in the light distribution at the exit pupil. The exit pupil therefore is good place to define and characterize the nature of the light in an image forming optical system. Knowing the distribution of light (i.e., amplitude and phase) at the exit pupil, one can calculate the impulse response or PSF of the optical system using the diffraction integral and Fourier optics techniques [47][48][49]. This fully accounts for the effects of both aberrations and diffraction.

2.18 Monochromatic Wavefront Aberrations

Snell's law governs the refraction of light at optical surfaces. It involves the use of the sine function, which is non-linear.

$$\sin(\phi) = \phi - \frac{1}{3!}\phi^3 + \frac{1}{5!}\phi^5 - \frac{1}{7!}\phi^7 + \ldots \qquad \text{.....(2.28)}$$

In paraxial systems, angles are small, $\sin(\phi) \approx \phi$, then first-order theory is applied, no aberrations and spherical wavefronts. In non-paraxial systems, higher order terms in the power series expansion of the sine function can be significant, and aberrations are no longer negligible. The non-zero aberrations cause wavefronts to deviate from sphericity. Non-zero aberrations occur even when refracting surfaces of lenses are

perfectly spherical. Non-zero aberrations occur even for a perfect plane-parallel plate in a converging or diverging beam of light because Snell's law is non-linear.

Therefore expecting the wave aberration function is expressed as power series expansions or polynomials. For example, a weighted sum of basis functions, monomials, or modes, which are functions of the pupil coordinates [50].

The wave aberration function, W(x,y), is defined as the distance, in optical path length (product of the refractive index and path length), from the reference sphere to the wavefront in the exit pupil measured along the ray as a function of the transverse coordinates (x,y) of the ray intersection with a reference sphere centered on the ideal image point. It is not the wavefront itself but it is the departure of the wavefront from the reference spherical wavefront as indicated in figure (2.18).

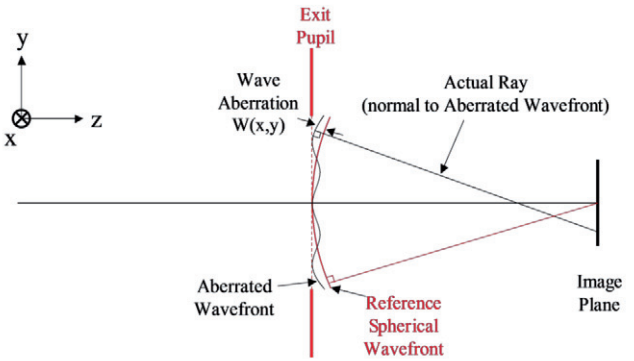

Figure (2.18): Wave Aberration Function for a Distant Point Object [50]

2.19 Calculating the PSF and MTF

The image of a point object formed by the optical system is the point spread function or impulse response. It is defined as [43][47]:

$$PSF(x,y) = \frac{1}{\lambda^2 d^2 A_p}\left\| FT\left\{ p(x,y)e^{-i\frac{2\pi}{\lambda}W(x,y)} \right\}\Big|_{f_x=\frac{x}{\lambda d}, f_y=\frac{y}{\lambda d}} \right\|^2 \quad \text{.....(2.29)}$$

Where:

FT is the Fourier Transform Operator.

d is the distance from the exit pupil to the image.

A_p is the area of the exit pupil.

$P(x,y)$ define shape, size, and transmission of exit pupil.

$e^{-i\frac{2\pi}{\lambda}W(x,y)}$ accounts for the phase deviations of the wavefront from a reference sphere.

$W(x,y)$ is the wave aberration function at the exit pupil.

$P(x,y) = p(x,y).e^{-i\frac{2\pi}{\lambda}W(x,y)}$ is the generalized exit pupil function.

The Modulation Transfer Function (MTF) is modulus of the Optical Transfer Function (OTF). The OTF and MTF are given by [48]:

$$OTF(s_x,s_y) = \frac{FT\{PSF\}}{FT\{PSF\}|_{s_x=0,s_y=0}} = \frac{FT\left\{\left\|FT\left\{p(x,y)\cdot e^{-i\frac{2\pi}{\lambda}W(x,y)}\right\}\Big|_{f_x=\frac{x}{\lambda d},f_y=\frac{y}{\lambda d}}\right\|^2\right\}}{FT\left\{\left\|FT\left\{p(x,y)\cdot e^{-i\frac{2\pi}{\lambda}W(x,y)}\right\}\Big|_{f_x=\frac{x}{\lambda d},f_y=\frac{y}{\lambda d}}\right\|^2\right\}|_{s_x=0,s_y=0}} \quad (2.30)$$

$$MTF(s_x,s_y) = \|OTF(s_x,s_y)\| \quad (2.31)$$

The OTF can also be calculated as the auto-correlation of the generalized pupil function, but because the Fourier transform will be used for computational efficiency, the OTF will be calculated using the FT of the PSF.

For visual applications it is often more convenient to express the PSF and MTF in terms of visual angle. These expressions are given by [51]:

$$PSF(\sin(\theta_x),\sin(\theta_y)) = \frac{\lambda^2}{A_p}\left\|FT\left\{p(x,y)e^{-i\frac{2\pi}{\lambda}W(\frac{x}{\lambda},\frac{y}{\lambda})}\right\}\right\|^2$$

$$PSF(\theta_x,\theta_y) \cong \frac{\lambda^2}{A_p}\left\|FT\left\{p(\frac{x}{\lambda},\frac{y}{\lambda})e^{-i\frac{2\pi}{\lambda}W(\frac{x}{\lambda},\frac{y}{\lambda})}\right\}\right\|^2 \quad \textit{for small angles}.....(2.32)$$

Where:

$p\left(\frac{x}{\lambda},\frac{y}{\lambda}\right)$ defines shape, size (in unit of wave lengths), and transmission of exit pupil

$\frac{A_p}{\lambda^2}$ is the area of the exit pupil in unit of (wavelength)^2

$$OTF(s_x,s_y) = \frac{FT\{PSF(\theta_x,\theta_y)\}}{FT\{PSF(\theta_x,\theta_y)\}_{s_x=0,s_y=0}} \quad .....(2.33)$$

$$MTF(s_x,s_y) = \|OTF(s_x,s_y)\| \quad .....(2.34)$$

s_x is in units of cycles per radian
s_y is in units of cycles per radian } or is unit in cycle per degree

The calculations and computational domains are illustrated in Figures (2.19, 2.20).

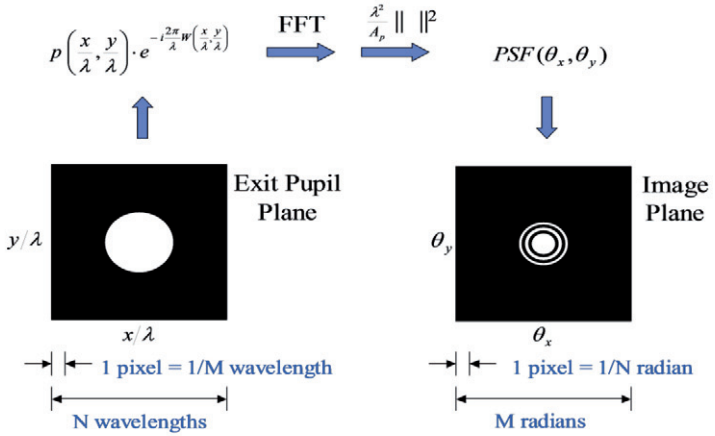

Figure (2.19): PSF Calculation and Computational Domains

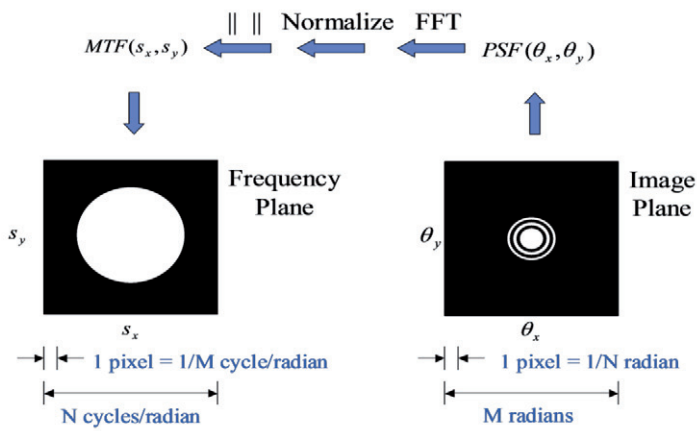

Figure (2.20): MTF Calculation and Computational Domains

Aberrations negatively impact image quality. They change the size and shape of impulse response or PSF, which blurs the image. In terms of frequency analysis, the frequency response of the optical system is reduced by phase distortion within the pass band.

2.20 Orthonormal Polynomial for Hexagonal Apertures

It is quite common in optical design and testing using Zernike circle polynomials to describe the aberration of a system. These polynomials have the advantage that they represent balanced aberrations. Because of their orthogonality across a circular aperture, the Zernike expansion coefficients are independent of each other, each coefficient represents the standard deviation of the corresponding Zernike term (with exception of the piston term), and the variance of the aberration is equal to the sum of the coefficients. However, in the case of a large segmented mirror, the segments are typically hexagonal in the shape, as in the Keck telescope. The advantage of the orthogonality of the polynomial can be lost because Zernike polynomials are not orthogonal over hexagonal region. Here, orthonormal polynomial for hexagonal apertures can be determined by the Gram-Schmidt orthogonalization of Zernike circle polynomial. The polynomial thus obtained is depending on the sequence of the Zernike polynomials used in the orthogonalization process [59].

Figure (2.21) show a unit hexagon inscribed inside a unit circle. Each side of the hexagon has a length of unity. The area of the hexagon is $A=3\sqrt{3}/2$. In Cartesian coordinates *(x,y)*, the aberration function for a hexagonal pupil or aperture can be expanded in terms of polynomials $H_j(x,y)$ that are orthonormal over the aperture [60]:

$$W(x,y)=\sum_j a_j H_j(x,y) \quad \text{.....(2.35)}$$

Where a_j is an expansion or the aberration coefficient of the polynomial $H_j(x,y)$. The orthonormality of the polynomial is represented by:

$$\frac{2}{3\sqrt{3}}\int H_j H_{j'}\,dxdy=\delta_{jj'} \quad \text{.....(2.36)}$$

Where $\delta_{jj'}$ stands for the Kronecker symbol, which equal to 1 if and only if $j=j'$.

The hexagonal region of integration consists of five parts: rectangle ACDF, triangles AGB, GCB, DHE, and HFE with limits of integration $(-1/2,1/2;\ -\sqrt{3}/2,\sqrt{3}/2)$, $(1/2,1;\ \sqrt{3}(1-x),0)$, $(1/2,1;\ -\sqrt{3}(1-x),0)$, $(-1,-1/2;\ 0,\sqrt{3}(1+x))$, and $(-1,-1/2\ ;\ 0,\sqrt{3}(1+x))$, respectively.

The area of the unit hexagon is approximately 17.3% smaller than the area of the unit circle.

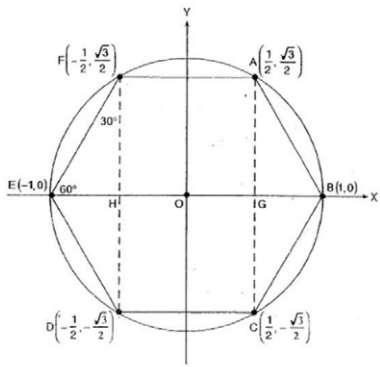

Figure (2.21): Unit hexagon Inscribed Inside a Unit Circle Showing the Coordinates of its Corners. Each side of the Hexagon has a length of Unity. The *x* axis passes through the corners B and E of the Hexagon, and the *y* axis bisects its parallel sides AC and FD.

The relative value of the coefficients of the circle polynomials whose linear combination yields an orthonormal hexagonal polynomial H_k and the variance are given by [60]:

$$a_j = -\frac{2}{3\sqrt{3}} \int_{hexagon} W(x,y) H_j \, dxdy \qquad \text{.....(2.37)}$$

$$\sigma^2 = \sum_j a_j^{\,2} \qquad j \neq 1 \qquad \text{.....(2.38)}$$

Respectively, the mean value of each polynomial, except for j=1, is zero. The number of polynomial, i.e, the maximum value of j is increased until the variance is equal to the actual variance within a prechosen tolerance.

The orthonormal polynomials H_j(x,y) can be obtained from the Zernike polynomials Z_j(x,y) by Gram-Schmidt orthogonalization process [61]. Using abbreviated notation, where the argument (x,y) of the polynomial is omitted,

$$G_1 = Z_1 = 1$$

$$G_{j+1} = \sum_{k=1}^{j} c_{j+1,k} H_k + Z_{j+1} \qquad \text{.....(2.39)}$$

$$H_{j+1} = \frac{G_{j+1}}{\|G_{j+1}\|} = \frac{G_{j+1}}{\left[\frac{1}{2}\int_{hexagon} G_{j+1}^2 \, dxdy\right]^{1/2}} \qquad \text{.....(2.40)}$$

Where:

$$c_{j+1,k} = -\frac{2}{3\sqrt{3}} \int_{hexagon} Z_{j+1} H_k \, dxdy$$

Thus, the *H*-polynomial are obtained recursively starting with $H_1 = 1$. each *H*-polynomial is a linear combination of Zernike polynomials. The orthonormal *H*-polynomials represent the unit vectors of the space that spans the aberration function. Substituting for the Zernike polynomial and noting that of an odd function over the hexagon is zero owing to its symmetry, it is possible to obtain:

$$G_2 = c_{21}H_1 + Z_2 = c_{21}Z_1 + Z_2 = Z_2 = 2x$$

$$H_2 = \frac{2x}{\left[\frac{1}{A}\int_{hexagon} 4x^2 dxdy\right]^{1/2}} = \sqrt{6/5}(2x) = 1.09545Z_2 = 2\sqrt{6/5}\ \rho\sin\theta$$

Where:

A= - 2/3 √3

Similarly

$$H_3 = \sqrt{6/5}(2y) = 1.09545Z_3 = 2\sqrt{6/5}\ \rho\cos\theta$$

$$c_{41} = 1/\sqrt{3} \quad , \quad c_{42} = 0 = c_{43}$$

$$G_4 = \left(1/\sqrt{3}\right)Z_1 + Z_4 = \sqrt{3}(2\rho^2 - 5/6)$$

$$H_4 = \frac{\sqrt{3}(2\rho^2 - 5/6)}{[\frac{1}{A}\int_{hexagon} 3(2\rho^2 - 5/6)^2 dxdy]^{1/2}} = \frac{\sqrt{3}(2\rho^2 - 5/6)}{\sqrt{43/60}}$$

$$= \sqrt{5/43}Z_1 + 2\sqrt{15/43}Z_4 = 0.34100Z_1 + 1.18125Z_4 = 2\sqrt{15/7}\ \rho^2\sin 2\theta$$

The other polynomial terms can be obtained in similar manner as shown as in table (2-2) [24].

Table (2-2): Orthonormal Hexagonal Polynomials in Polar Coordinates

H1 = 1

H2 = 2 √(6/5) ρ sinθ

H3 = 2 √(6/5) ρ cosθ

H4 = 2 √(15/7) ρ^2 sin2θ

H5 = √(5/43) (-5 + 12 ρ^2)

H6 = 2 √(15/7) ρ^2 cos2θ

H7 = (4√(10)/3) ρ^3 sin3θ

H8 = 4 √(42/3685) (-14 ρ + 25 ρ^3) sinθ

H9 = 4 √(42/3685) (-14 ρ + 25 ρ^3) cosθ

H10 = 4 √(70/103) ρ^3 cos3θ

H11 = (10/3) √(7/99258181) (-10 (297 - 598 ρ^2) ρ^2 sin2θ + 5413 ρ^3 sin4θ

H12 = (30 / √(492583)) (-249 ρ^2+ 392 ρ^4) sin2θ

H13 = (3 / √(1072205)) (737 - 5140 ρ^2 + 6020 ρ^4)

H14 = (30 / √(492583)) (-249 ρ^2+ 392 ρ^4) cos2θ

H15 = (10/3) √(7/99258181) (10 (297 - 598 ρ^2) ρ^2 cos2θ + 5413 ρ^4 cos4θ

$H16 = (2.17600248\,\rho - 13.23551876\,\rho^3 + 16.15533716\,\rho^5)\sin\theta + 5.95928883\,\rho^5 \sin 5\theta$

$H17 = 4\sqrt{(5/97)}(-22\,\rho^3 + 35\,\rho^5)\sin 3\theta$

$H18 = 2\sqrt{(6/1089382547)}\,(70369\,\rho - 322280\,\rho^3 + 309540\,\rho^5)\sin\theta$

$H19 = 2\sqrt{(6/1089382547)}\,(70369\,\rho - 322280\,\rho^3 + 309540\,\rho^5)\cos\theta$

$H20 = 4\sqrt{(385/295894589)}\,(-3322\,\rho^3 + 4635\,\rho^5)\cos 3\theta$

$H21 = (-2.17600248\,\rho + 13.23551876\,\rho^3 - 16.15533716\,\rho^5)\cos\theta + 5.95928883\,\rho^5 \cos 5\theta$

2.21 Strehl Ratio

To quantify the performance of an AO system, the Strehl ratio of the PSF is used. The PSF $s(\vec{x})$ is interpreted as the image plane intensity distribution that results from imaging a point source. The point spread function is a very useful performance measure since the resolution of an adaptive optics system is determined directly from the width of the PSF. The Strehl ratio is defined as the ratio of the central intensities of the aberrated PSF and the diffraction-limited PSF of the instrument [44].

$$SR = \frac{s(\vec{x}=0)_{aberrated}}{s(\vec{x}=0)_{diffraction\ limitted}} \quad \text{.....(2.41)}$$

Where $s(\vec{x})$ is the intensity point spread function.

$\vec{x}$ defines a point in the image plane.

Strehl ratios can be measured instantaneously or, averaged over time, which is called the integrated Strehl. The instantaneous Strehl is the Strehl ratio of a short exposure PSF (such as the speckle pattern seen in figure (2.12)), while the integrated Strehl is the Strehl ratio of a long exposure PSF (such as in figure (2.13)). Usually long exposures are used to see fainter objects. Comparing the instantaneous and integrated Strehl will however prove to reveal some interesting information about the performance of the AO system. Figure (2.22) shows a few examples of computer generated integrated PSFs with different Strehl ratios for an 8 m class telescope. A system is said to be well corrected when the Strehl is greater than 80%. This is also called the *Marechal limit* [62].

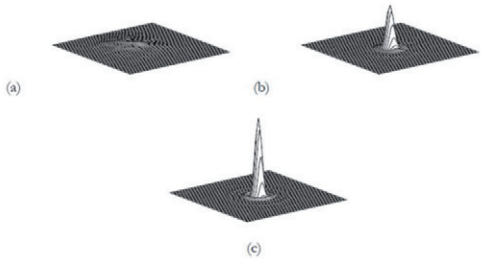

Figure (2.22): (a) Integrated uncorrected PSF with a Strehl ratio of 8%, (b) integrated corrected PSF with a Strehl ratio of 49%, (c) and diffraction-limited PSF [44].

Chapter Three

An Adaptive Optics

3.1 Introduction

Adaptive Optics (AO) was proposed as early as the 1950s, by Horace Babcock, an astronomer at Mt. Wilson and Palomar Observatories. This technology became powerful enough for a first attempt to realize such a system in the late 60s. The early systems were developed for military and aerospace applications, and progress was driven by these communities, who had considerable resources available to them. Early milestones in the advancement of AO systems were the development of the first functioning Deformable Mirrors (DMs), and subsequent experiments with natural guide stars, by John Hardy and co-workers at ITEK company in 1972, and the atmospheric compensation achieved with the Compensated Imaging System (CIS) on Mt. Maleakala, Hawaii, using stars and satellites as guide stars during the years 1982-85 [46][42].

The quality of images and spectra taken at ground-based astronomical observatories is degraded by distortions in the Earth's atmosphere. Rather than achieving diffraction limited resolution, large ground-based telescopes at the best sites seldom achieve image quality better than the diffraction-limit of a 20cm diameter telescope (0.63 arcsec in the visible, 500 nm wavelength). This blurring, which is due to temperature inhomogeneities in the atmosphere, is called atmospheric *seeing*. If the seeing could be eliminated, an 8m telescope would be able to achieve 0.015 arcsec resolution in the visible and 0.069 arcsec resolution in the K-band of the infrared (2200 nm) [45]. Compensation of the atmospheric seeing can be achieved using the technology of AO, a technique which is being pursued by every major ground-based observatory.

Satellite observatories are very costly to operate, however, and exceedingly hard to maintain. Ground-based telescopes of the 10m class equipped with AO are now able to deliver sharper images than HST, at least in the near infrared. Naturally, ground-based observatories are much more versatile and accessible for keeping instruments up to date. While satellite observations remain important for some scientific cases, many programs can be conducted more efficiently from the ground [44].

The techniques of AO are those by which telescope optics is adjusted on a rapid time scale to compensate for distortions in the wavefront entering a telescope. These adjustments are generally applied to a relatively small optical element in an optical train following the Cassegrain or Nasmyth focus and continuously readjusted on a time scale measured in milliseconds. Also a larger isoplanatic angle at infrared wavelength,

25 arcsec at 2500 nm compared to 5 arcsec for visible wavelength, makes AO correction easier than at visible wavelength [42].

Techniques of AO are to be distinguished from those of *active optics* for which adjustments are relatively much slower, often on a time scale of hours. Adjustments of this latter type are usually made to the primary mirror by actuators that adjust the shape of the mirror. The goal of active optics corrections is usually to reduce the aberrations of a telescope [44] [64] [66].

In this chapter the basic principles of AO will be discussed. Techniques by which a distorted wavefront is corrected before detection are considered. It is also possible to apply postdetection corrections to images and achieve high angular resolution on bright sources with ground-based telescopes. The effects of turbulence from the point of view of the time-averaged Modulation Transfer Function (MTF) of the atmosphere are considered.

3.2 Preliminaries

To appreciate the daunting task faced by designers of AO systems, one should understand that an initially plane wavefront traveling 20km through the turbulent atmosphere accumulates, across the diameter of a large telescope, phase errors of a few micrometers. These have to be sensed with a minimum number of photons and corrected to about 1/50 of a micrometer every millisecond or so. Another complication is that, for short integration times, the field of view over which the atmospheric wavefront distortions and hence the images are correlated, the isoplanatic angle, is very small (only a few arc second for visible wavelengths) [46].

Because of the high bandwidth and the small field to which correction can generally be applied, AO uses a small deformable mirror (DM) with a diameter of (8 to 20) cm located behind the focus of the telescope at or near an image of the pupil. In some current projects, the possibility of using a large deformable secondary mirror is being developed. The choice of the number of actuators (usually piezoelectric) is a tradeoff between degree of correction, using a faint reference source, and available budget. For instance, a near-perfect correction for an observation done in visible light with an 8m telescope would require ~ 6400 actuators, whereas a similar performance at 1.5m needs only ~ 225 actuators [46].

A large number of actuators require a similarly large number of subapertures in the wavefront sensor, which means that for correction in the visible, the reference star should be ~ 25 times brighter than that corrected in the infrared. Most current astronomical systems are designed to provide diffraction-limited images in the near-infrared (1000-2500) nm with the capability for partial correction in the visible.

However, some military systems for satellite observations in the USA do provide full correction in the visible on at least 1m class telescopes [44].

Two main methods are used to measure the degraded wavefront, the *Shack-Hartmann* device, which measure the slope of the wavefront from the positions of the images of the reference star given by each subapertures, and *Curvature Sensing* device, where the intensities measured in strongly defocused images provided directly the local curvatures of the wavefront. Correction in the Shack-Hartmann device is made with individual piezoelectric actuators. Correction in a curvature sensing system is accomplished with a bimorph adaptive mirror, made of two bonded piezoelectric plates. With both methods, wavefront sensing is done on a reference star or even on the observed object itself if it is bright enough and has sufficiently sharp light gradients [42].

General scheme for an AO System is shown in figure (3.1). The control system is generally a specialized computer that calculates from the wavefront-sensor measurements the commands sent to the actuators of the DM. The calculation must be done fast (within 0.5 to 1 msec); otherwise the state of the atmosphere may have changed rendering the wavefront correction inaccurate. The required computing power needed can exceed several hundred million operations for each set of commands sent to a 225 actuator DM. As in active optics systems, zonal or modal control methods are used. In zonal control, each zone or segment of the mirror is controlled independently by wavefront signals that are measured for the subaperture corresponding to that zone. In modal control, the wavefront is expressed as the linear combination of modes that best fit the atmospheric perturbations.

The operation of AO is strongly affected by the size of the isoplanatic angle, usually ~ 25" at 2500nm (IR), but only ~ 5" at 500nm (visible). It is generally not possible to find a sufficiently bright reference star close enough to an arbitrary astronomical object. Conditions are much better in the infrared than in the visible since atmospheric turbulence has weaker effect on longer wavelengths for a given AO correction. The spatial and temporal sampling of the disturbed wavefront can therefore be reduced, which in turn permits the use of fainter reference stars. Coupled with the larger isoplanatic angle in the IR, this gives a much better outlook for AO correction than in the visible.

Nevertheless, even for observations at 2200 nm, the sky coverage achievable by this technique (equal to the probability of finding a suitable reference star in the isoplanatic patch around the chosen target) is only of the order of 0.5 to 1%. It is therefore quite normal that most scientific applications of AO so far have been on objects which naturally provide their reference object like solar system small bodies, stellar environments, stellar clusters and a few very bright Seyfert nuclei.

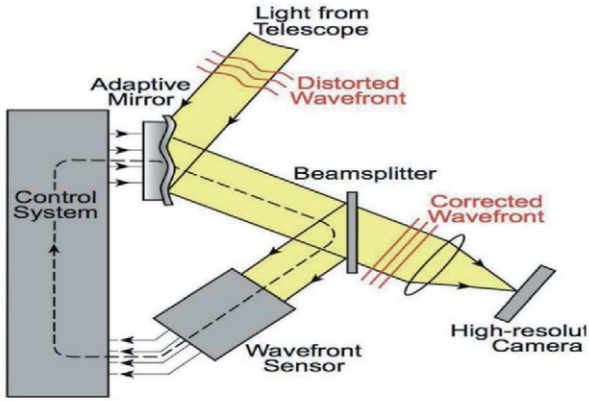

Figure (3.1): General Scheme for an AO System [65].

Figures (3.2-3) show the effect and the enhancement of the Spiral Galaxy image obtained without/with turbulence correction using the AO process.

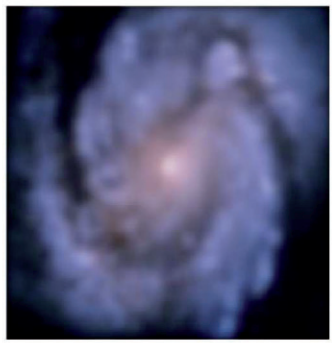

Figure (3.2): Spiral Galaxy M100 Image without AO Correction

Figure (3.3): Spiral Galaxy Image with AO Correction

3.3 Parameters of Deformable Mirror

Deformable Mirrors (DMs) are mirrors whose surface can be deformed, in order to achieve wavefront control and correction of optical aberrations. Figure (3.4) shows the operation of a DM Model with AO System. The DM has several parameters can be categorized into:

1) Number of actuators: determines the number of degrees of freedom (wavefront inflections) the mirror can correct. It is very common to compare an arbitrary DM to an ideal device that can perfectly reproduce wavefront modes in the form of Zernike polynomials. For predefined statistics of aberrations a DM with M actuators can be equivalent to an ideal Zernike corrector with N (usually $N < M$) degrees of freedom. For correction of the atmospheric turbulence, elimination of low-order Zernike terms usually results in significant improvement of the image quality, while further correction of higher-order terms introduces less significant improvements. For strong and rapid wavefront error fluctuations such as shocks and wake turbulence typically encountered in high-speed aerodynamic flow fields, the number of actuators, actuator pitch and stroke determine the maximum wavefront gradients that can be compensated [77].

2) Actuator pitch: is the distance between actuator centers. DMs with large actuator pitch and large number of actuators are bulky and expensive.

3) Actuator stroke: is the maximum possible actuator displacement, typically in positive or negative excursions from some central null position. Stroke typically ranges from ±1 to ±10 micrometers. Free actuator stroke limits the maximum amplitude of the corrected wavefront, while the inter-actuator stroke limits the maximum amplitude and gradients of correctable higher-order aberrations [77].

4) Influence function: is the characteristic shape corresponding to the mirror response to the action of a single actuator. Different types of DMs have different influence functions; moreover the influence functions can be different for different actuators of the same mirror. Influence function that covers the whole mirror surface is called a "modal" function, while localized response is called "zonal".

5) Actuator coupling: shows how much the movement of one actuator will displace its neighbors. All "modal" mirrors have large cross-coupling, which in fact is good as it secures the high quality of correction of smooth low-order optical aberrations that usually have the highest statistical weight.

6) Response time: shows how quickly the mirror will react to the control signal. Response time can vary from microseconds (Micro-Electro-Mechanical Systems (MEMS) mirrors) to tens of seconds for thermally controlled DMs [78].

7) Hysteresis and creep: are nonlinear actuation effects that decrease the precision of the response of the DM. For different concepts, the hysteresis can vary from practically zero (membrane mirrors) to tens of percent for mirrors with piezoelectric actuators.

Hysteresis is a residual positional error from previous actuator position commands. It limits the mirror ability to work in a feedforward mode, outside of a feedback loop [45].

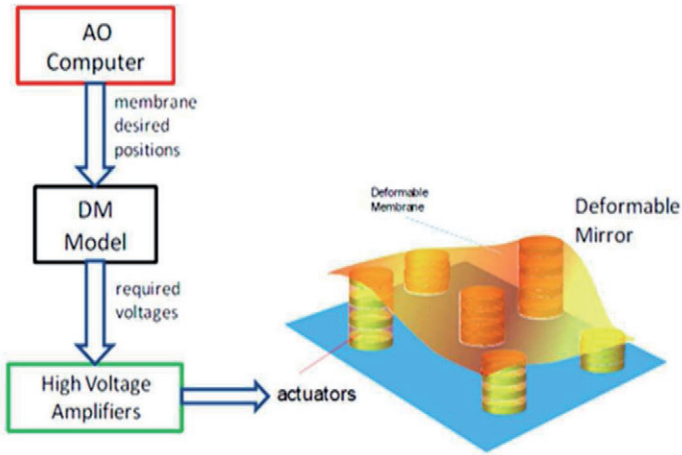

Figure (3.4): Operation of a DM Model with AO System [45].

3.4 Concepts of Deformable Mirror

Main types of DMs are shown in figures (3.5-6) and a number of DM concepts are presented [40][67][68][69][70]:

1) Segmented concept: mirrors are formed by independent flat mirror segments. Each segment can move a small distance back and forth to approximate the average value of the wavefront over the patch area. Normally these mirrors have little or zero cross-talk between actuators. Considerable improvement of the performance of the segmented mirror can be achieved by introducing three degrees of freedom per segment: piston, tip and tilt. These mirrors require three times more actuators than piston segmented mirrors and they suffer from diffraction on the segment edges. This concept was used for fabrication of large segmented primary mirrors for the Keck telescopes [40].

2) Continuous faceplate concept: mirrors with discrete actuators are formed by the front surface of a thin deformable membrane. The shape of the plate is controlled by a number of discrete actuators that are fixed to its back side. The shape of the mirror depends on the combination of forces applied to the faceplate, boundary conditions (the way the plate is fixed to the mirror), the geometry and the material of the plate. These mirrors are considered to be the best, as they allow smooth wavefront control with very large (up to several thousands) degrees of freedom.

3) Micro-Electro-Mechanical Systems (MEMS) concept: mirrors are fabricated using bulk and surface micromachining technologies. MEMS mirrors have a great potential to be cheap. They can break the high price threshold of conventional AO [67].

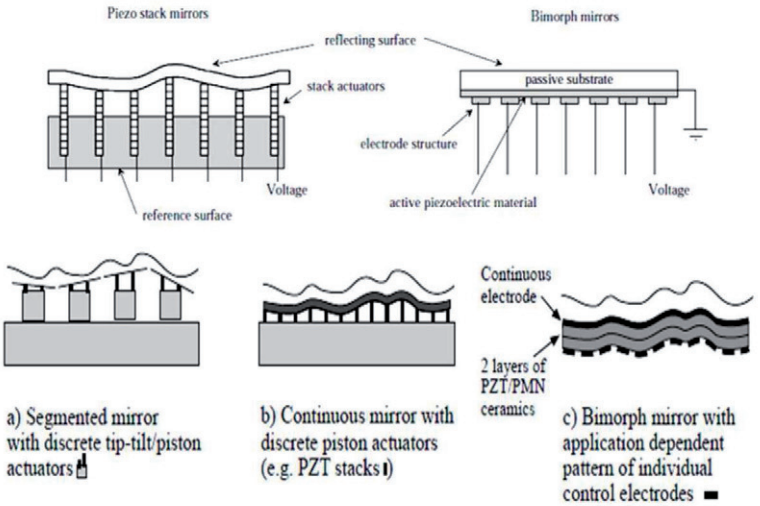

Figure (3.5b): Three Classes of DM. (a) A Segmented Mirror with tip-tilt/piston Actuators behind each Segment, (b) Continuous Facesheet Mirrors with individual Piston Actuation and an Example of a Bimorph Mirror (c).[17]

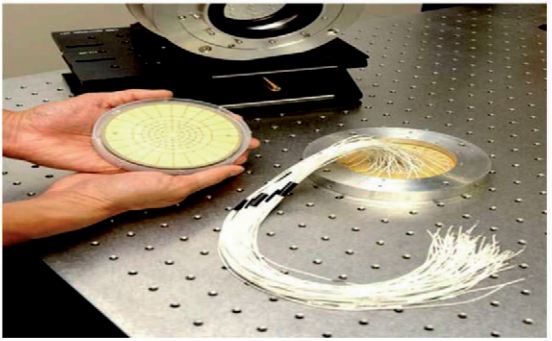

Figure (3.6): The DM from Hokupa`a-85 (with 85 Actuators)

4) Membrane concept: mirrors are formed by a thin conductive and reflective membrane stretched over a solid flat frame. The membrane can be deformed electrostatically by applying control voltages to electrostatic electrode actuators that can be positioned under the membrane; a bias voltage is applied to all electrodes, to make the membrane initially spherical. The membrane can move back and forth with respect to the reference sphere [68].
5) Bimorph concept: mirrors are formed by two or more layers of different materials. One or more of (active) layers are fabricated from a piezoelectric or electrostrictive material. Electrode structure is patterned on the active layer to facilitate local response. The mirror is deformed when a voltage is applied to one or more of its electrodes, causing them to extend laterally, which results in local mirror curvature. Bimorph mirrors are rarely made with more than 100 electrodes [69].
6) Ferrofluid concept: mirrors are liquid DMs made with a suspension of small (about 10 nm in diameter) ferromagnetic nanoparticles dispersed in a liquid carrier. In the presence of an external magnetic field, the ferromagnetic particles align with the field, the liquid becomes magnetized and its surface acquires a shape governed by the equilibrium between the magnetic, gravitational and surface tension forces. Using proper magnetic field geometries, any desired shape can be produced at the surface of the ferrofluid. This new concept offers a potential alternative for low-cost, high stroke and large number of actuators DMs [70].

3.5 The Main Types of Actuators

The main types are listed here [45] [66]:
1) Piezo stack: this is a DM made of discrete actuators, composed of piezo-electric ceramics, which is composed of an electrostrictive material.
2) Electrostatic: MEMS type of devices, made on a single piece of silicon, on which electrostatic actuators are built.
3) Magnetic: these are integrated devices using voice-coil actuators, composed of a magnet and a solenoid.

3.6 The Main Types of Wavefront Sensors (WFS)

The main types of wavefront sensors are briefly described here, with representative diagrams [44][72][73]:

1) **Curvature:** This technique was introduced by Roddier (1988). The wavefront aberration is measured at two planes around the focal plane, where the aberration causes excess illumination (at I_1) and lack of illumination (at I_2).

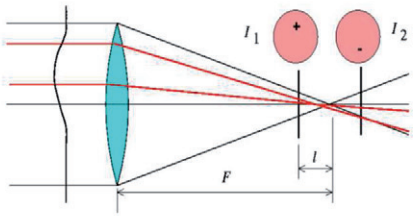

Figure (3.7): Schematic of Curvature Wavefront Sensor

2) Shack-Hartmann (SH): The pupil is divided into "subapertures" by a lenslet array. The aberrations produce displacements of the spots produced by each subaperture. The position of the spot is proportional to the gradient of the wavefront at each subaperture. '*Centroiding*' is the process of finding the position of each spot, computing the centre of gravity of the subaperture in pixel units [17] [74].

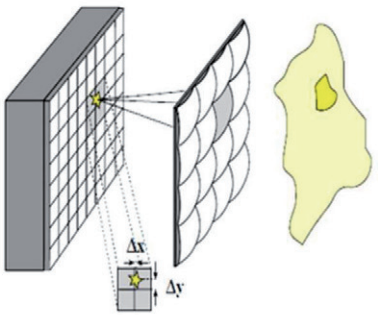

Figure (3.8): Measurement of Principle of a Shack-Hartmann WFS [17]

Figure (3.9): Shack-Hartmann WFS From ThorLab

3) Lateral Shearing Interferometer: An interferogram can be formed by making the wavefront interfere with its shifted version. The aberrations can be measured by analyzing the fringe shapes.

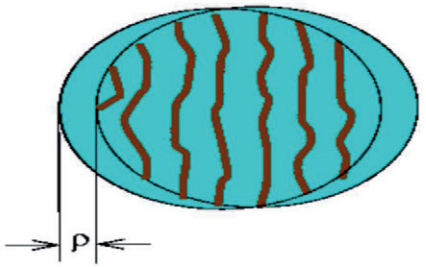

Figure (3.10): Schematic of Lateral Shearing Interferometer WFS

4) Pyramid: A glass pyramid is placed at the focus of a lens, dissecting the beam into 4 apertures. It is possible to measure the wavefront aberrations by comparing the intensity on equivalent positions on each subaperture [75].

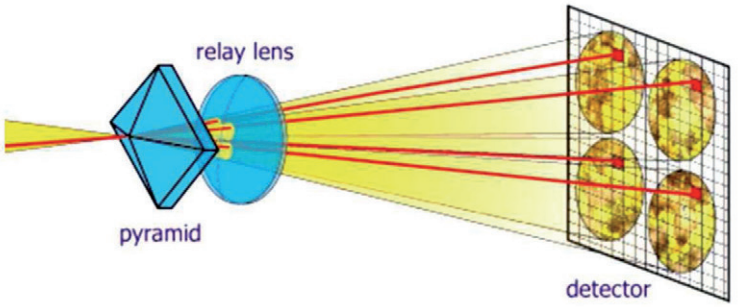

Figure (3.11): Schematic of Pyramid WFS [75]

3.7 Functional Description

A general scheme for an AO system is presented in figure (3.12). The telescope is pointed to a guide star, which is used for measuring the atmospheric turbulence. The light beam from the telescope is received by the DM or wavefront corrector, which corrects the aberrations caused by the turbulence, shaping its surface with a figure that nulls the shape of the wavefront passed through the atmosphere.

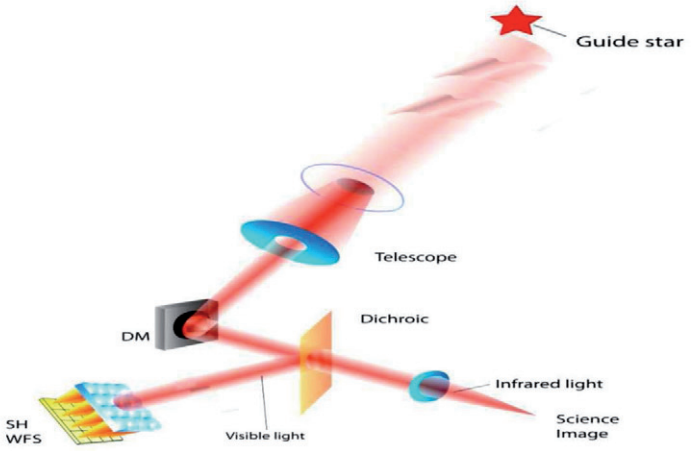

Figure (3.12): Diagram of a Typical AO System with Natural Guide Star Placed after a Telescope. The AO System is composed of a DM and a Phase or WF Sensor [45]

the DM, an AO system includes a phase or WF Sensor to measure the residual aberrations after the wavefront has been corrected by the DM. The Shack Hartmann WFS (SH-WFS) is the most commonly used in AO systems for astronomy. The WFS uses optical wavelengths (which are commonly referred to those between 350 and 1000 nm) for measuring the wavefront. This is usually implemented by diverting the light with a dichroic, letting the infrared light pass to a science instrument. The AO system works in closed-loop by trying to keep a flat (or null) residual wavefront at the science image. This is orchestrated by a powerful computer, capable of processing the large amount of information coming from the WFS and calculating the commands to the DM. A "real-time" computer is used, meaning one which is capable of doing these computations in real-time, at rates of potentially thousands of updates per second. The current personal computers have become so powerful that they are starting to be used as AO computers.

Different types of DMs have been developed over the last 30 years. They are usually classified depending on the technology used in the actuators. Most DMs have actuators in an equally spaced rectangular grid, where their acting direction is parallel amongst them and perpendicular to the mirror membrane. By varying their length a few microns, the membrane becomes locally deformed at the actuator position. The

local deformation of the membrane is usually called the "influence function" produced by the actuator. A typical influence function on the membrane spans neighbouring actuators, having a 10% to 20% effect on the immediately adjacent actuators. Figure (3.13) presents a typical influence function [45].

The control of the DM is generally based on knowledge of the actuator influence functions. Actuator influence functions are used to define the relationship between the actuator commands and the deformations of the mirror surface. Usually, a least squares method is used to determine the set of actuator commands which will minimize the error in the mirror surface. Mirror deformations due to each actuator command multiplied by the influence of that actuator are added to the initial distorted mirror surface, which results in the corrected mirror shape [17].

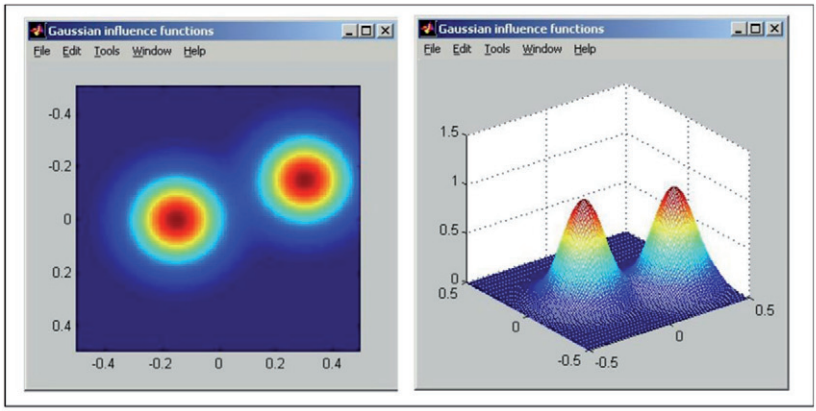

Figure (3.13): Gaussian Influence Functions

Figure (3.14) shows this process of correcting a deformed mirror surface based on the actuator influence functions. It can be seen from the figure that the corrected mirror shape has smaller deformations (two orders of magnitude smaller) which is of higher spatial frequency than the initial mirror surface.

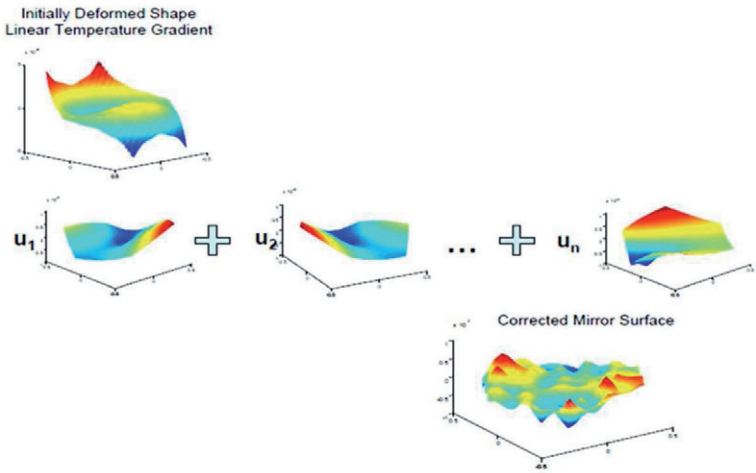

Influence functions can be generated experimentally; one specifies the

Figure (3.14): Correction of Distorted Mirror by adding Actuator Influence Functions Scaled by Input Values

Shape and extent of the single-actuator influence function, one has the choice of five shapes: Green's Function, Gaussian, Piston, Linear, and Cubic. Each shape is prompted for two parameters Δx, Δy that define the effective width of the influence function.

3.8 Implication of Open and Close-Loop Operation

The classical AO systems are a closed-loop based systems, a WFS measures the action of the DM, because it is placed "downstream" with respect to the DM in the optical path. So it measures the residual error and feeds it back to the system. See the top part of figure (3.15) for a comparison diagram.

In principle, this closed-loop system is fundamentally simple; it measures the phase as a function of the position of the optical wavefront under consideration, determines its aberration, computes a correction, reshapes the DM, observes the consequence of that correction, and then repeats this process over and over again as necessary if the phase aberration varies with time. Via this procedure, the AO system is able to improve optical resolution of an image by removing aberrations from the wavefront of the light being imaged [45].

Multi-Object Adaptive Optics (MOAO) requires operation in an optical open-loop, i.e. the wavefront sensor does not measure residual turbulence but rather "raw" incoming aberrations caused by the atmosphere. The DM in charge of applying the

inverse of the turbulent phase must therefore work with no feedback, unlike classical AO systems, where the wavefront sensor closes the optical loop for DM positioning [76].

Figure (3.15): Comparison diagram for closed-loop and open-loop operation in AO. Top panel: closed-loop operation, showing how WFS closes the loop with respect to the DM. Bottom panel: open-loop operation, where the WSF paths are different and unrelated with respect to the DM path.

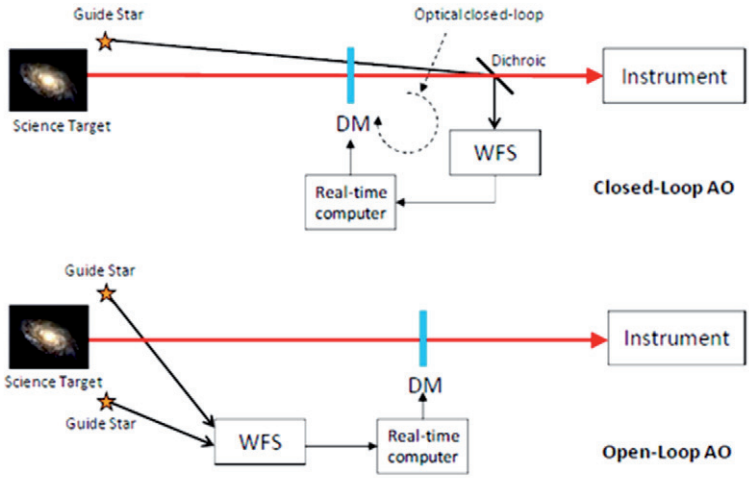

Figure (3.15): Comparison Diagram for Closed-loop and Open-loop Operation in AO system [45]

3.9 Implementation of Close-Loop Operation using a Poke Matrix Method in AO Process

In a typical AO system which comprising a deformable mirror, a Shack Hartmann wavefront sensor (SH-WFS) and an aberrated beam of light reflect from a DM and illuminates the SH-WFS. The WFS measures the average gradient (aka slope) of the wavefront over each sub-aperture in an array of lenslet to produce a vector of wavefront slope measurements.

To complete an adaptive optics system with this optical setup, converting the wavefront slope measurements into commands to the deformable mirror is needed. When the vector of measured slopes is multiplied by the control matrix it produces a vector of commands that if it applied to the DM (in addition to any commands that

currently exist on the DM) will produce the minimum RMS wavefront slopes [86] as follows:

1) The Simulation Model and WFS Data

The surface of the deformable mirror is controlled by 32 actuators as an example arranged on a 6 x 6 grid with no actuators on the corners. Shack- Hartmann wavefront sensors are arranged on a 14 x 14 grid with the corners obscured, so that there are 196 wavefront slope measurements in two directions. Thus, the Poke matrix (P) is 196 x 32 elements. To find a linear P matrix between DM commands and the phase shifts (gradients) on the sensor we have to do a least square identification between the values of the command voltages (as the inputs to the system) and the output phase measurements.

2) Setup the DM-Actuator Pattern

The used DM-actuator pattern arranged as two dimensional mesh grid of 32 actuators as shown in Figure (3.16).

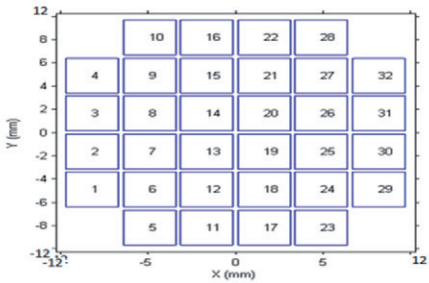

Figure (3.16): Layout and Actuator Numbering of the 32-Channel Square-Grid.

3) Create the Influence Functions

Influence functions (IF) can be generated experimentally, which can take the shape of Green's Function, Gaussian, Piston, Linear, and Cubic. The senior parameters that affect the final shape are Δx and Δy that define the effective width of the influence function.

Simulation the influence functions are developed out using the Gaussian model. Each actuator influence function is generated from the corresponding actuator of SH-WFS. The resulting surface shape of the DM is generated according to the vector coefficients. This vector of coefficients then represented as a column vector in the actuator influence matrix.

Figure (3.17) shows first scaled IF, which is scaled to 14 X 14 samples and fit to 80% from aperture size. Therefore, 96 locations were taken to represent by 32 actuators

instead of 196 samples. Euclidian distance was used to calculate and determine the closer actuator (from 32 actuators) to the sample for doing the action.

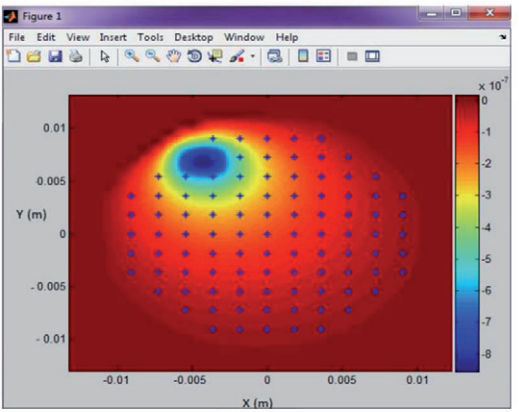

Figure (3.17): The First scaled DM Influence Function.

4) Making a Poke Matrix

The adaptive optics control matrix is generated by creating a pseudo-inverse of a measured Poke matrix. The Poke matrix is a matrix that measures the response of each actuator on the SH-WFS. The Poke matrix is generated by actuating each actuator or group of actuators individually, measuring the wavefront slopes, and assembling the vector of slope measurements into a matrix. Figure (3.18) shows the Poke matrix that was measured for a 32 actuator, square grid membrane DM layout in array 96 x 32 elements [86].

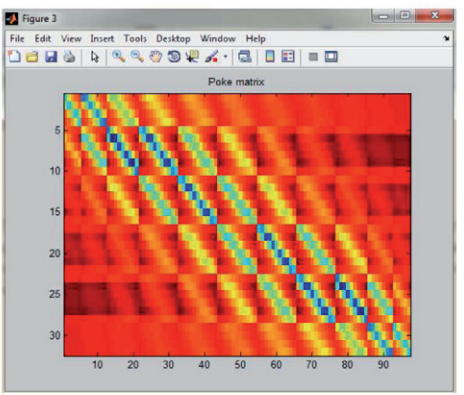

Figure (3.18): The Poke Matrix.

This matrix describes the relationship between commands to the DM and response of the wavefront sensor. Mathematically, this matrix can be written as [87]:

$$\nabla\phi = P.c \qquad .....(3.1)$$

Where $\nabla\phi$ is the vector of wavefront slopes, P is the Poke matrix, and c is the vector of DM commands. The best Poke matrix contains only the effect of the actuator motion. The low gain mode can be removed from the control matrix using the singular-value decomposition (SVD) techniques that will be described later.

5) Making a Control Matrix from a Poke Matrix

Once a good Poke matrix has been established, this Poke matrix needs to be inverted to create a control matrix that relates the measured wavefront slopes to DM commands mathematically it can be represented as [84]:

$$\begin{aligned} c &= pseudoinverse(P).\nabla\phi \\ &= \Gamma.\nabla\phi \qquad .....(3.2) \end{aligned}$$

Where Γ represent the control matrix. Since the Poke matrix is not square (it is 2 times the number of sub-apertures by the number of actuators), it cannot be inverted classically, but instead it requires a different mathematical technique.

SVD can be used to calculate a pseudo-inverse of a matrix. In SVD, the Poke matrix is decomposed into the product of three matrices U, S, and V.

U is a set of orthonormal output basis vectors that are found by finding the eigenvectors of $P.P^*$ where (*) operator is the transpose.

V is a set of orthonormal input basis vectors that are found by finding the eigenvectors of $P^*.P$.

S is a diagonal matrix of singular values that are found as the square root of the eigenvalues of the eigenvectors in U and V.

The SVD decomposition can be used to calculate a pseudo-inverse of the Poke matrix, P, as [85]:

$$\Gamma = P^+ = V.S^+.U^* \qquad .....(3.3)$$

Where the (+) operator is the pseudo-inverse. The pseudo-inverse of S is found by taking the reciprocal of each diagonal element of the S matrix.

The condition number of a matrix is the ratio of the highest gain to the lowest gain. If a matrix is formed of orthogonal vectors, then the condition number will be 1. Since in most deformable mirrors the influence functions are not orthogonal, it is

expected that the condition number will not be unity, but lower values are generally better.

6) Using a Control Matrix in Integrator Control

After establishing a control matrix, the commands for the DM are calculated in each step of the AO loop by taking the commands from the last loop and adding the measured slopes times the control matrix times the system gain, or [86];

$$c(t) = c(t-1) + gain \ . \Gamma . \nabla \phi \qquad .....(3.4)$$

Chapter Four

Simulation and Problem Analysis

4.1 Introduction

Very large ground-based telescope with primary mirror more than 100m diameter has been considered. Such a diameter may allow planet imaging from the ground if images of high contrast can be achieved over regions large enough for planet detection. Most of the proposed primary configurations use segmented mirrors. For a proposed primary configuration consisting of segments with gaps between them, diffractive modeling is needed to reveal the image and how that image is affected by this pupil configuration; gap width, apodization, miss-positioning, and tilt errors of the individual segments.

Current plans for future very large telescopes envisage apertures of more than 100m diameter, their gain over the present generation of (10m) telescopes will not be simply a proportion to their increased light gathering power only, correction to diffraction limit with AO is needed to increase image sharpness.

In order to test the performance of different designs, several programs have been developed to model the resulting diffraction patterns or PSFs for different apertures. In its simplest form, the models determine the Fraunhofer diffraction of light through an aperture. The diffraction is calculated by performing a Fourier Transform (FT) on an incoming wavefront that represented by a complex 2D array. Taking the real part of the resultant amplitude image and squaring it gives the intensity.

Several ideas explore the use of alternative “apodized” apertures for high contrast imaging in the optical or near-infrared [79][80].

The complete model calculates the diffraction of a light wave’s amplitude passing through the aperture of a telescope with a secondary mirror (obscuration) and support structure (spiders). An input wavefront array with the shape of the pupil undergoes FT to give a PSF and MTF of the telescope. A single wavelength PSF is generated (750 nm), after calculating the PSF of the aperture, an ideal test image can be convolved with the PSF.

A crucial issue for any design is its ability to not only achieve a high contrast, but do so in a way that does not seriously degrade the intrinsic resolution of the companion PSF. The smaller aperture size essentially spreads out the light of any faint companion and drastically increases the integration time, making it harder to detect [81].

Next the array undergoes an inverse FFT which results in the intensity pattern at the pupil plane to create the image on the detector. The simulation was performed with 1500 × 1500 and 1024 × 1024 element arrays; also the array is taken in terms of the

wavelength in order to keep the theoretical diffraction limit of the telescope of interest to be truncated at zero value inside this array.

4.2 Simulation of Telescope's Aperture Configurations

Several configurations for the primary mirror of the telescope can be analyzed such as circles, or any shape derived from them by cutting along chords. The analytical study for next generation optical telescope; utilizing mirror segmentation techniques, including the following steps:

- Studying the primary mirror of the telescope, which is composed of a number of individual mirror subsegments. These subsegments act as a single mirror envisage apertures of more than 100m diameter.
- Comprising the efficiency of different configurations with adjacent hexagonal subsegments and close-packed circular subsegments and other shapes.
- The apodization shapes effect on the contrast diffraction limit (high–contrast imaging of exoplanets) can be studied.
- Studying the effect of subsegments gap, the secondary obscuration, subsegments size and the spiders.

In figures (4.1, 4.2, 4.3) several designs has been created to test the simulations in order to gauge the degradation in contrast from the ideal case and to determine the best configuration. In the absence of atmospheric turbulence, the phase function *W(x,y)* in Eq. (2.29) becomes zero then:

$$PSF(x,y) = \frac{1}{\lambda^2 d^2 A_p}\left\| FT\{p(x,y)\}\Big|_{f_x=\frac{x}{\lambda d},\, f_y=\frac{y}{\lambda d}} \right\|^2$$

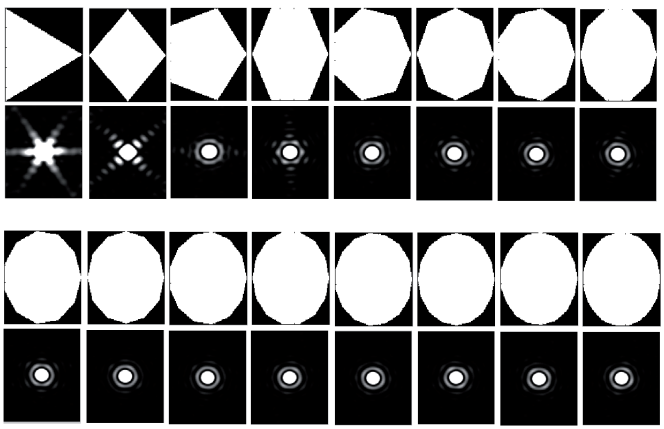

Figure (4.1): One Subsegment Pupil's Configurations for Telescope with 500 Pixels Diameter and their Corresponding PSFs.

Figure (4.1) shows pupil's configurations for telescope with 500 pixels diameter, the corresponding point spread functions are shown. The PSF is computed at its coherent, combined focus.

The PSF at different telescope apertures are shown in Figures (4.2, 4.3), built up from 25 pixels subsegments diameter for the 500 pixels diameter without/with obscuration and spiders with their corresponding PSF are shown.

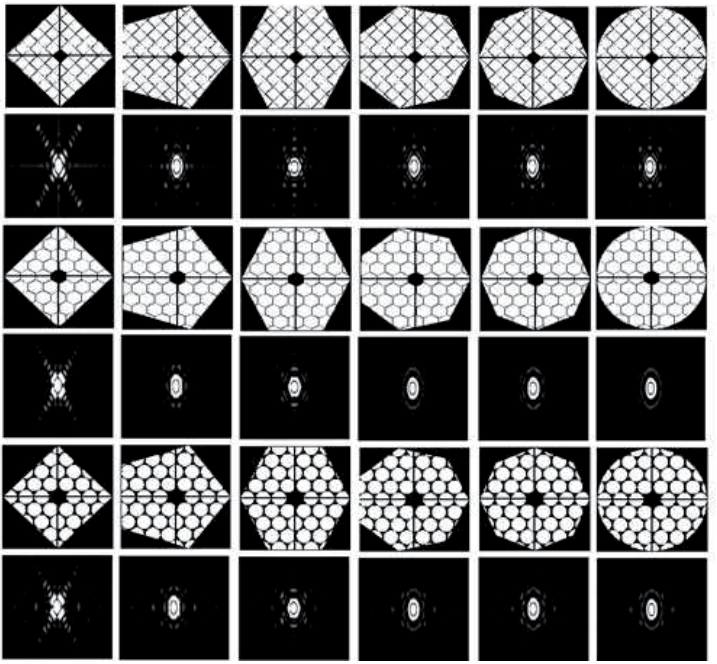

Figure (4.2): Aperture Configurations for Telescopes Built up from 25 Pixels Subsegments Diameter with Corresponding Point Spread Functions without Obscuration and Spiders.

The MTF at different telescope apertures are shown in Figure (4.4) where each aperture considered as a one segment (i.e. trapezium (4), pentagon (5), hexagon (6), heptagon (7), octagon (8) and circular (cir)).

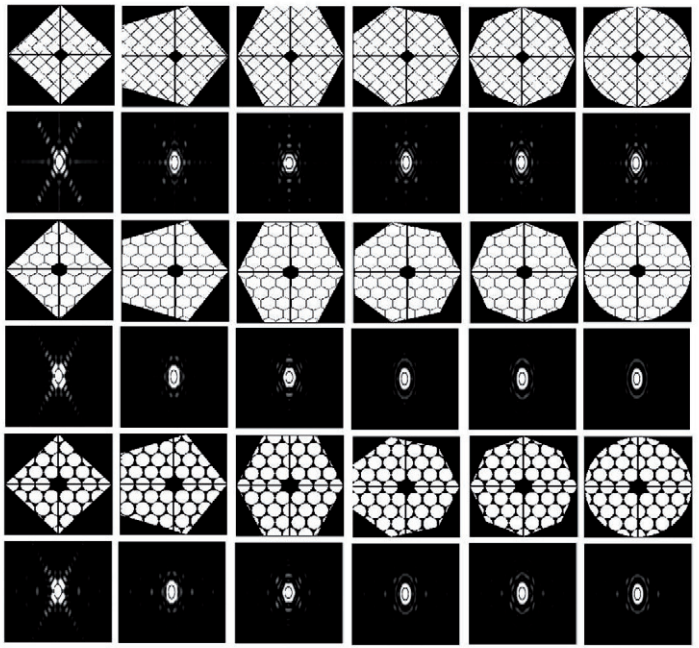

Figure (4.3): Aperture Configurations for Telescopes Built up from 25 Pixels Subsegments Diameter with Corresponding Point Spread Functions with

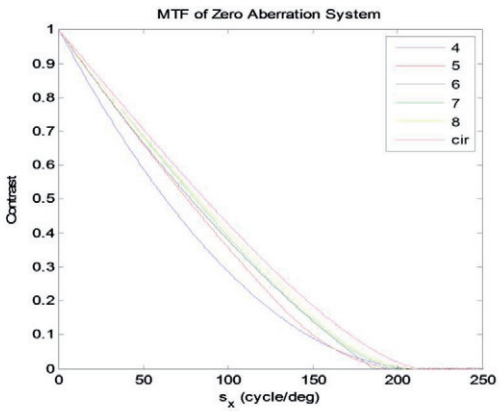

Figure (4.4): Contrast vs. Spatial Frequencies (s_x) in Cycle per Degree.

Figure (4.4) Normalized MTF is plotted as modulation (contrast) versus spatial frequency (in cycle per degree). Demonstrates very clearly that the non-segmented circular aperture is the highest cutoff frequency, which means that one segment circular aperture is the best for high contrast imaging and faint object detection.

The previous behavior (non-segmented circular aperture is the best MTF) will not stand when multiple segments is used to build primary mirror of a telescope. The corresponding results of the figures (4.1, 4.2, 4.3) can be summarized in figure (4.5), where the normalized MTF or the contrast drawn as a function for the spatial frequency. Note that in figures (4.5-a, b, c) the MTF for sub-segmented apertures (4-4 for trapezium subsegment in trapezium apodized aperture, 4-5 for that trapezium subsegment in pentagon apodized aperture and so on…). The highest cutoff frequency was found for hexagonal apodized aperture with different subsegment.

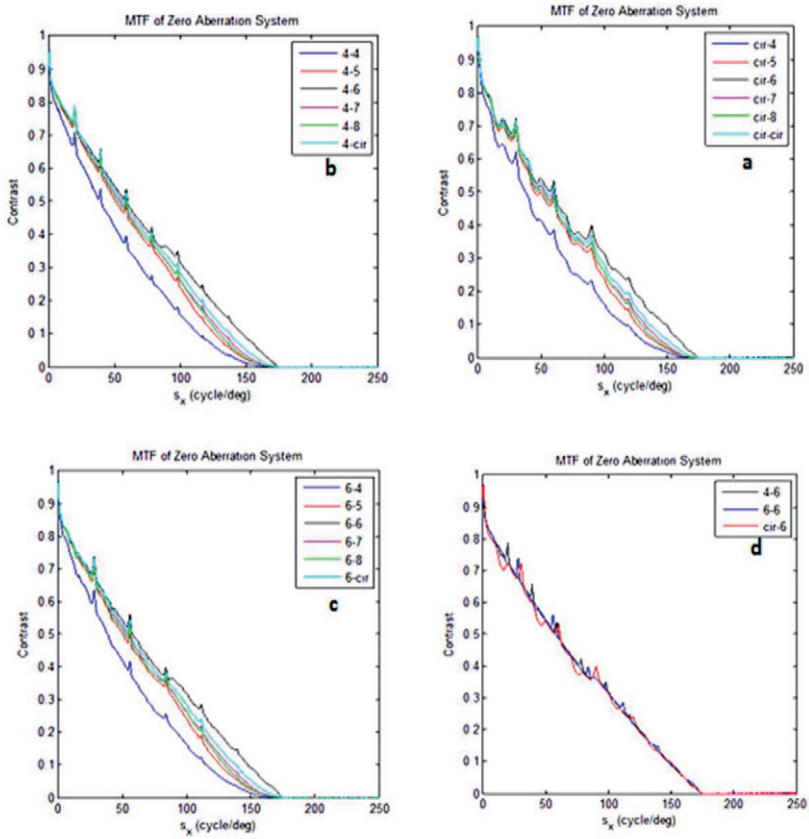

Figure (4.5): Contrast vs. Spatial Frequencies (S_x).

Figure (4.5d) shows that the highest contrast (MTF) was for hexagonal apodized aperture with trapezium subsegments (4-6), hexagonal apodized aperture with hexagon subsegments (6-6) and hexagonal apodized aperture with circular subsegments (cir-6) which are almost the same, means that the hexagonal apodized aperture is the optimal shape.

4.3 Simulation of Imaging through the Atmospheric Turbulence

A phase screen based on Kolmogorov turbulence theory was generated. The screen was generated based on a PSD function that was mentioned in chapter (2), Eq. (2.20). The aperture diameter and the r_0 is specified:

$$\phi_n(K) = 0.033 C_n^2 \times K^{-11/3} \qquad 1/L_0 \langle K \langle 1/l_0$$

Where: C_n^2 represent the strength of the turbulence and is equal to *Fried* coherent length $((r_0)^{-5/3})$.

The phase screen using Kolmogorov model will be structured as follows:

- Generating two dimensional array of integers (1024X1024).
- The square root of the generating array is taken to be represented the element K.
- Taking C_n^2 to be equal $((r_0)^{-5/3})$, where r_0 = 10 cm.
- Using Eq. (2.20) to Calculate the PSD.
- Generating the initial phase screen for Kolmogorov by taking the real part of FT of the square root for the PSD multiply by Gaussian white noise.

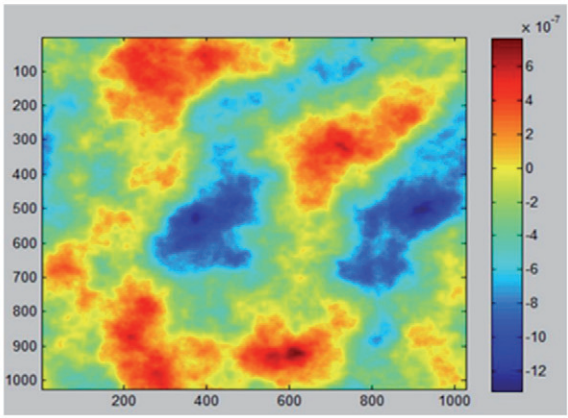

Figure (4.6): Simulated Initial Phase Screen for Kolmogorov.

In the next section the atmospheric turbulence (*Kolmogorov* spectrum) effect on hexagonal aperture and the response of the PSF and MTF will be considered.

4.4 Calculating the Affected MTF

The Kolmogorov turbulence (dynamic aberration) and its effects on the optical system performance will be included. Then the optimal three shapes of the apodized apertures mentioned in section 4.2 (i.e. hexagonal apodized aperture with subsegments

hexagon (6-6), hexagonal apodized aperture with subsegments circular (cir-6) and hexagonal apodized aperture with subsegments trapezium (4-6)) were tested, to determine the lower effected aperture by the turbulent to be adopted for the next generation optical telescope. At first the behavior of 6-6 apodized aperture system will be considered. Figure (4.7) shows the complex wavefront at affected 6-6 apodized aperture.

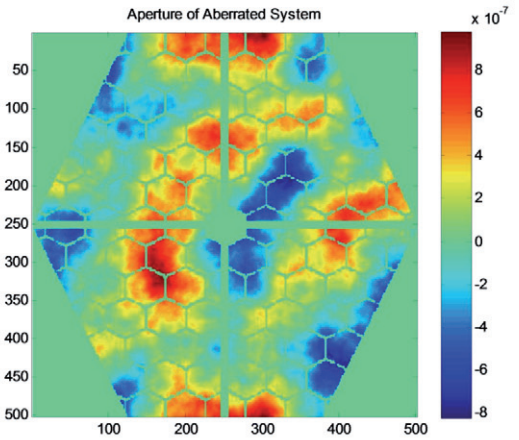

Figure (4.7): Aberrated 6-6 Apodized Aperture System.

The effect of the turbulent on the optical system is shown in figures (4.8-a, b), where the discrete line represents the diffraction limit (MTF of zero aberration system), while the continuous line represents the aberrated system.

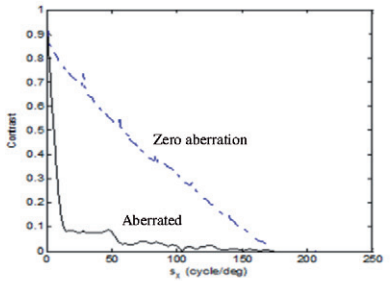

Figure (4.8a): MTF for 6-6 Aperture of Aberrated System in x Direction.

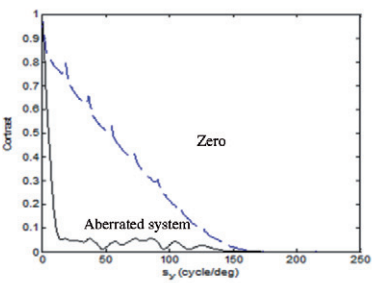

Figure (4.8b): MTF for 6-6 Aperture of Aberrated System in y Direction.

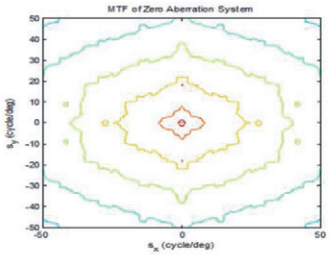

Figure (4.9a): MTF Contour of Zero Aberration System.

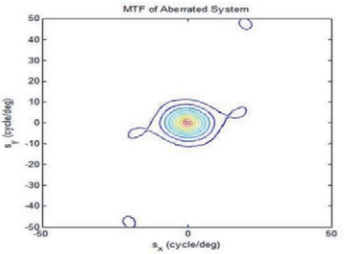

Figure (4.9b): MTF Contour of Aberrated System.

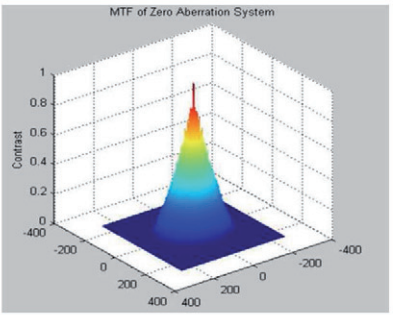

Figure (4.10a): MTF Surface of Zero Aberration System.

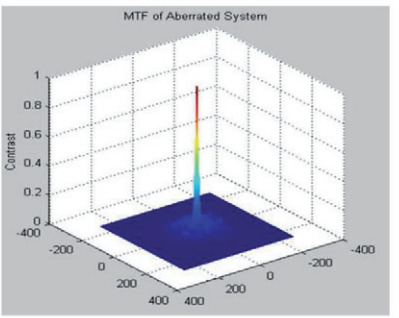

Figure (4.10b): MTF Surface of Aberrated System.

Figures (4.9, 4.10) show how the seeing condition r_0 was severely affects MTF for Large radius aperture and this will be reduced as radius decreases. In the same way the affected cir-6 apodized aperture is illustrated in figures (4.11, 4.12, 4.13 and 4.14).

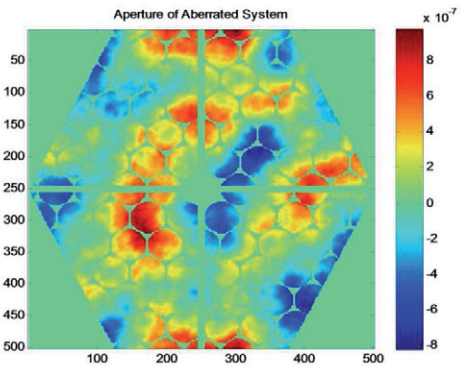

Figure (4.11): Aberrated cir-6 Apodized Aperture System.

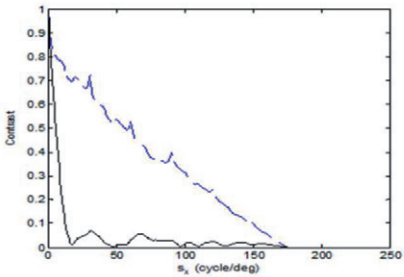

Figure (4.12a): MTF for cir-6 Aperture of Aberrated System in x Direction.

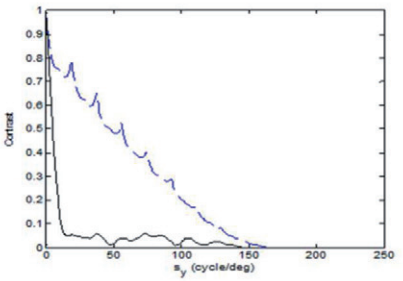

Figure (4.12b): MTF for cir-6 Aperture of Aberrated System in y Direction.

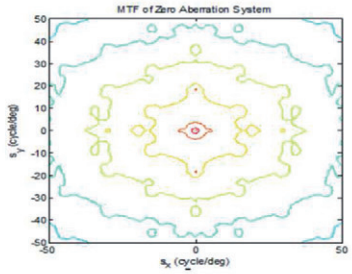

Figure (4.13a): MTF Contour of Zero Aberration System.

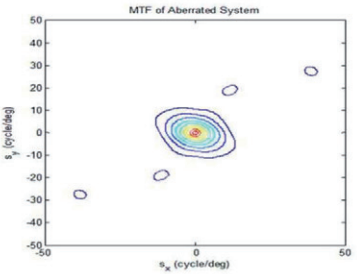

Figure (4.13b): MTF Contour of Aberrated System.

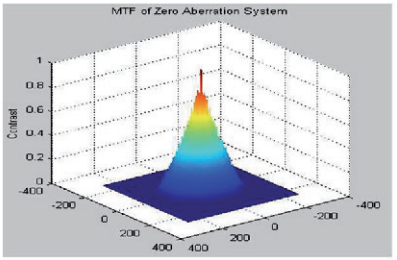

Figure (4.14a): MTF Surface of Zero Aberration System.

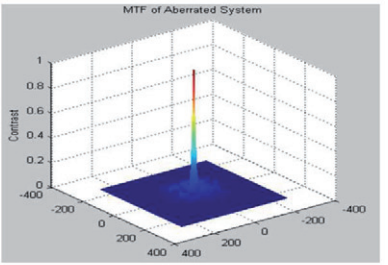

Figure (4.14b): MTF Surface of Aberrated System.

Also the affected 4-6 apodized aperture is shown in figures (4.15, 4.16, 4.17 and 4.18).

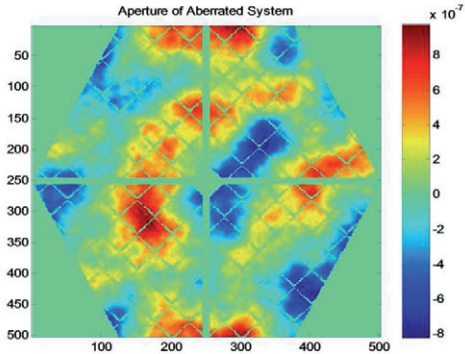

Figure (4.15): Aberrated 4-6 Apodized Aperture System.

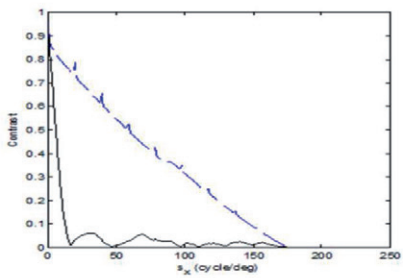

Figure (4.16a): MTF for 4-6 Aperture of Aberrated System in x direction.

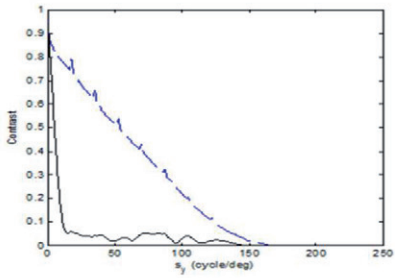

Figure (4.16b): MTF for 4-6 Aperture of Aberrated System in y direction.

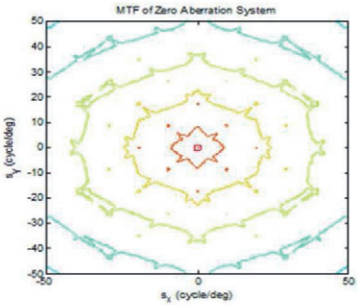

Figure (4.17a): MTF Contour of Zero Aberration System.

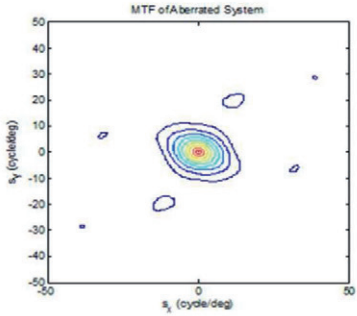

Figure (4.17b): MTF Contour of Aberrated System.

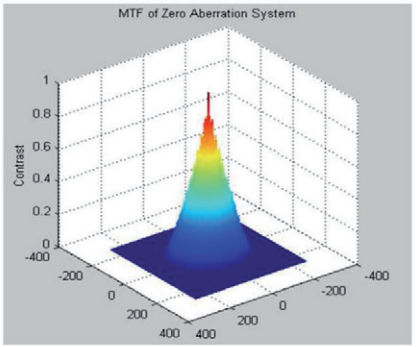

Figure (4.18a): MTF Surface of Zero Aberration System.

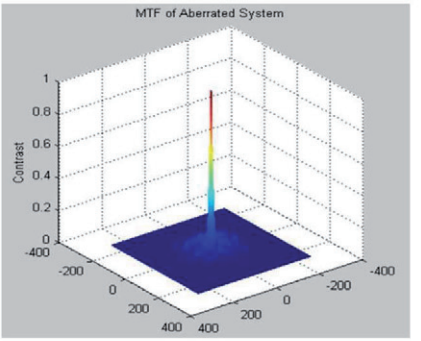

Figure (4.18b): MTF Surface of Aberrated System.

Now the effect of the remaining parts of the mirrors at edges of the hexagonal apodized aperture will be studied, in order to determine there effect on the optimal shape of the next generation field aperture. Clipped design and the corresponding PSF are shown in figure (4.19).

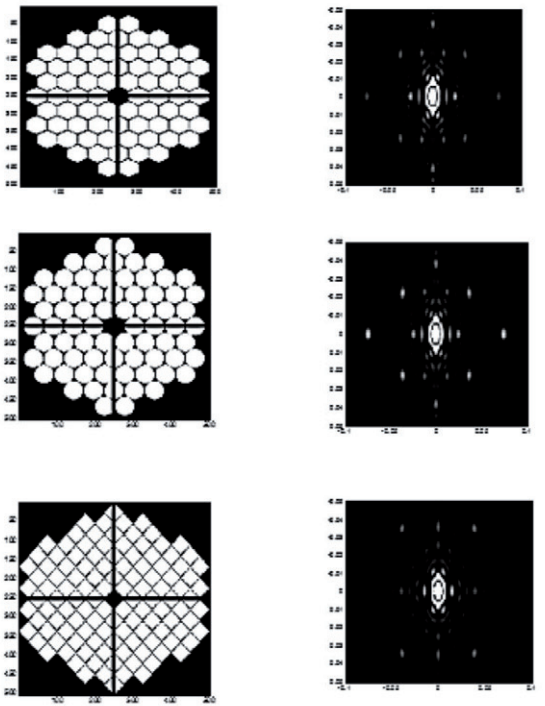

Figure (4.19): Clipped Apertures and the Corresponding PSFs.

The MTF with/without aberration for each design are shown in figure (4.20).

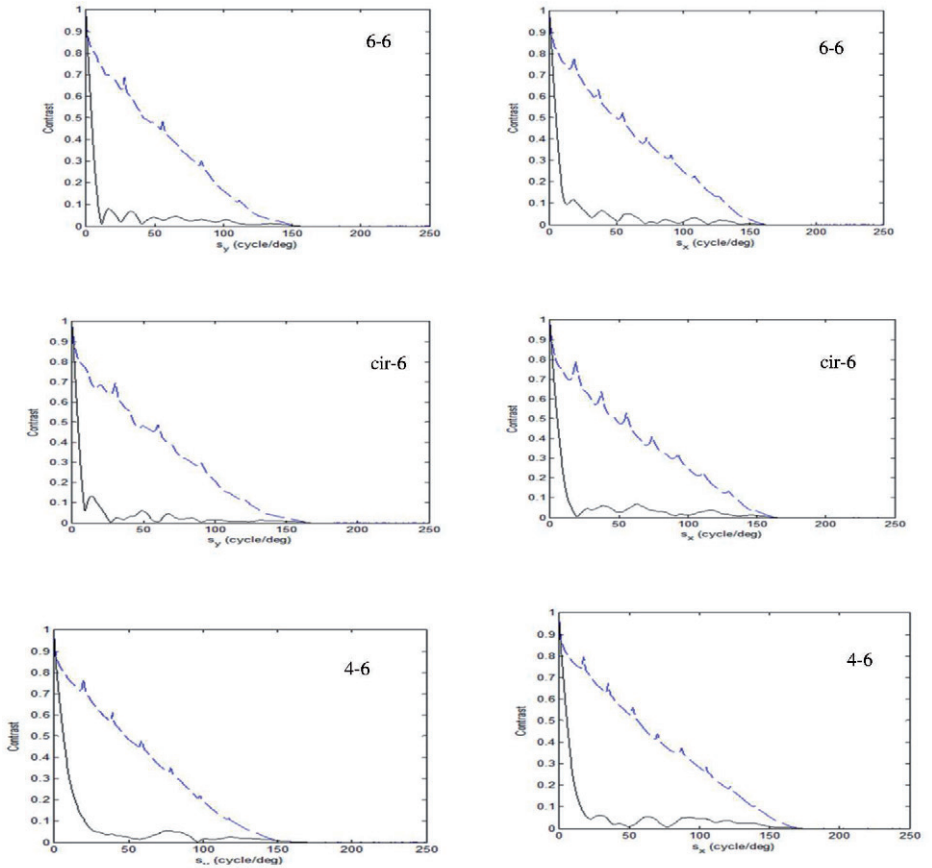

Figure (4.20): the MTF for each Clipped Aperture of Aberrated System in x and y Directions.

It can be concluded that the clipped 4-6 apodized aperture is the best configuration with the largest cutoff frequency and MTF. The ripple in the previous figures is due to the gaps between the subsegments. This ripple is minima for clipped 4-6 apodized aperture.

4.5 Image Quality Metrics

There are many kinds of image quality metrics. They can be categorized into two distinct groups, *geometric* such as Full Width at Half Maximum (FWHM), Mean Square Error (MSE), Peak Signal to Noise Ratio (PSNR) and *diffraction* such as MTF,

PSF and Encircled Energy (EE). Some metrics are both geometric and diffraction based such as MTF and EE, these metrics can be especially useful for setting the image quality criteria of certain imaging applications.

4.6 The objective fidelity criteria

In order to provide unbiased results, evaluation with subjective measures requires careful selection of the test subjects and carefully designed evaluation experiments.

The objective criteria, although widely used are not necessarily correlated with human perception of image quality. However, they are useful as a relative measure in comparing different versions of the same image.

Commonly used objective measures (geometric image quality metrics) are the MSE, PSNR [82][83], CORR is the correlation between object before and after convolution with the optical system and FWHM of the PSF.

Table (4-1, 4-2) contains some fidelity criteria for comparison between three different apertures before/after apodized aperture clipping.

Table (4-1): A Comparison the Geometric Image Quality Metrics before Removing the Remaining Parts of the Mirror

Aperture Type	Area	MSE	CORR	FWHM
Cir-6	151373	6.4071e-05	0.9975	0.0015
6-6	157364	6.3313e-05	0.9985	0.0015
4-6	159005	6.3078e-05	0.9988	0.0015

Table (4-2): A Comparison Geometric Image Quality Metrics after Removing the Remaining Parts of the Mirror

Aperture Type	Area	MSE	CORR	FWHM
6-6	135175	1.0916e-05	0.9984	0.0017
Cir-6	143111	1.1475e-05	0.9977	0.0016
4-6	152280	1.0634e-05	0.9987	0.0016

Until now the simulation result shows that the apodized aperture of 4-6 configurations has the best alignment, highest MTF, largest cutoff frequency and the largest collecting area.

The effect of subsegment radius on optical system PSNR can be shown in figure (4.21). It can be seen that the highest PSNR is for apodized aperture 4-6 with subsegment radius 25 pixels and decreased with increased subsegment radius, while other aperture type (6-6 and cir-6) have smooth variation with radius increased. For

technical constraints the small subsegment is required. Therefore, 25 pixels is the optimal radius for the proposal design.

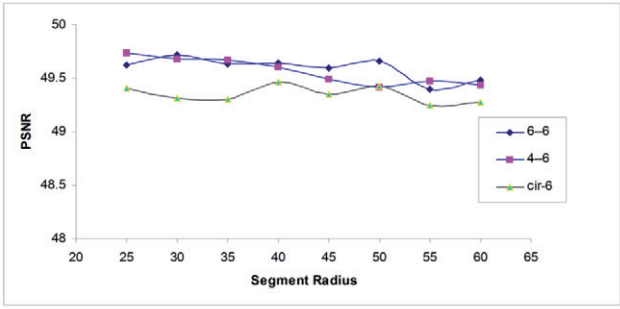

Figure (4.21): PSNR vs. Segment Radius.

The telescope PSNR as function of apodized aperture radius is shown in figure (4.22), one can found that for large apodized aperture over 150 pixels radius that three configurations are almost the same. This behavior coincides with MTF curves shown in figure (4.20), where the cutoff frequency is nearly 150 cycle / deg. Therefore, the MTF is a principle factor that determined the optimal dimension of the proposed telescope design. Tradeoff between telescope diameter over the optimal value and image quality is useless.

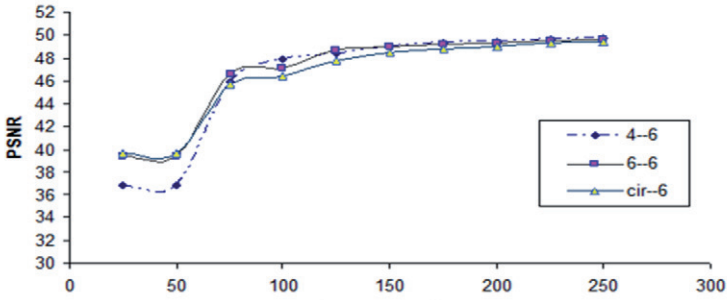

Figure (4.22): PSNR vs. Aperture Radius.

To investigate a relationship between subsegments gaps, PSNR, and MSE figures (4.23, 4.24, 4.25) r

Figure (4.23) illustrates a fact that PSNR is inversely proportional to the gaps between subsegments of the telescope aperture. This means that the narrower gap is the best for designing the apodized aperture of telescope. From this curves one can found that 6-6 apodized aperture is the optimal shape.

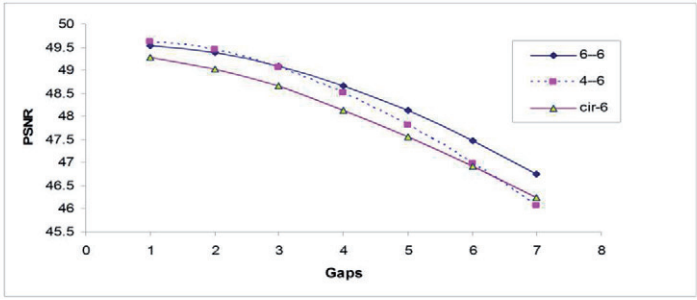

Figure (4.23): PSNR vs. Gaps.

When the gap is increased the MSE is increased in a nonlinear relationship as shown as in figure (4.24).

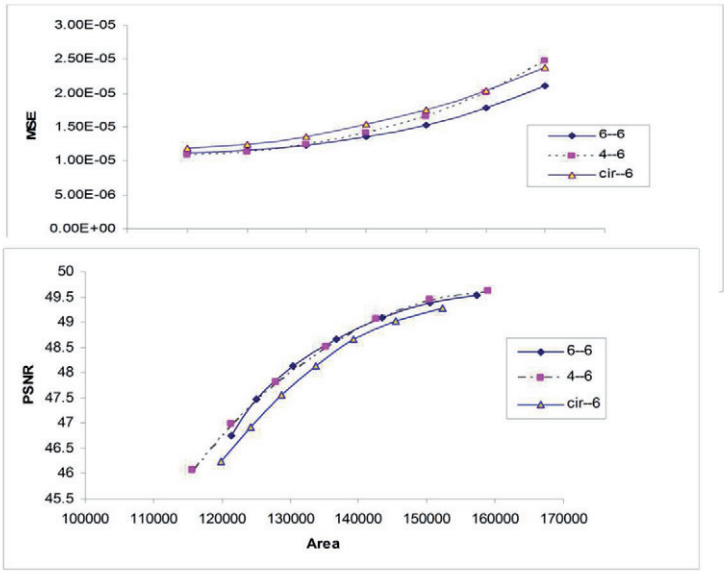

Figure (4.25): PSNR vs. Area.

While PSNR is directly proportional with collecting area of the telescope, as in Figure (4.25).

To study the effect of subsegments location two different design were used and results are as shown in figures (4.26, 4.27).

Table (4-3) contains geometric image quality metrics location's dependent. For the symmetrical and unsymmetrical design mentioned in figures (4.26, 4.27) it's very

clear; that rotating the symmetrical/ unsymmetrical apodized aperture by 90^0 decreases the efficiency of the faint object detection process. Because the extension of the dimension into x and y direction is not equal. Therefore, PSF and MTF will be affected as well as other dependent calculations.

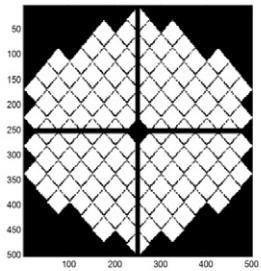

Figure (4.26): Symmetrical 4-6 Apodized Aperture.

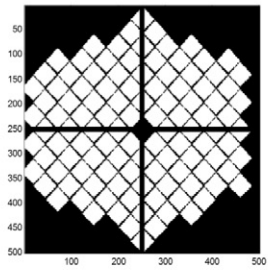

Figure (4.27): Unsymmetrical 4-6 Apodized Aperture.

Table (4-3): A Comparison Geometric Image Quality Metrics Location's Dependent.

Aperture Type	MSE	PSNR	CORR
Symmetrical 4-6	1.13e-05	49.4309	0.9977
Rotated by 90^0			
Symmetrical 4-6	1.15e-05	49.3799	0.9975
Rotated by 180^0			
Symmetrical 4-6	1.13e-05	49.4309	0.9977
Unsymmetrical 4-6	1.35e-05	48.6957	0.9955
Rotated by 90^0			
Unsymmetrical 4-6	1.36e-05	48.6562	0.9952
Rotated by 180^0			
Unsymmetrical 4-6	1.35e-05	48.6957	0.9955

The visual shape of the diffraction for different geometric forms of apertures (4-6, 6-6, cir-6 apodized apertures) and how can be changed with gaps changing can be illustrated in figures (4.28, 4.29, 4.30). It can be concluded that changes in gaps are so vital that can be destroyed the optical system PSF and produced artificial diffraction pattern. Nevertheless, 4-6 and cir-6 configurations have the highest fidelity criteria the visual output (seen) was so noisy and much degraded. The cleanest image was captured with 6-6 apodized apertures with less affected by gaps changes; therefore, this aperture configuration is the recommended design for next generation optical telescope.

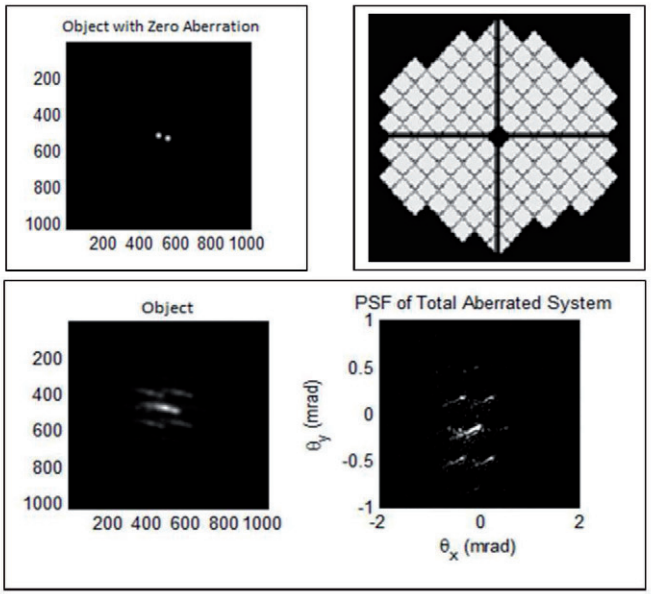

Figure (4.28): Diffraction Pattern for 4-6 Apodized Aperture.

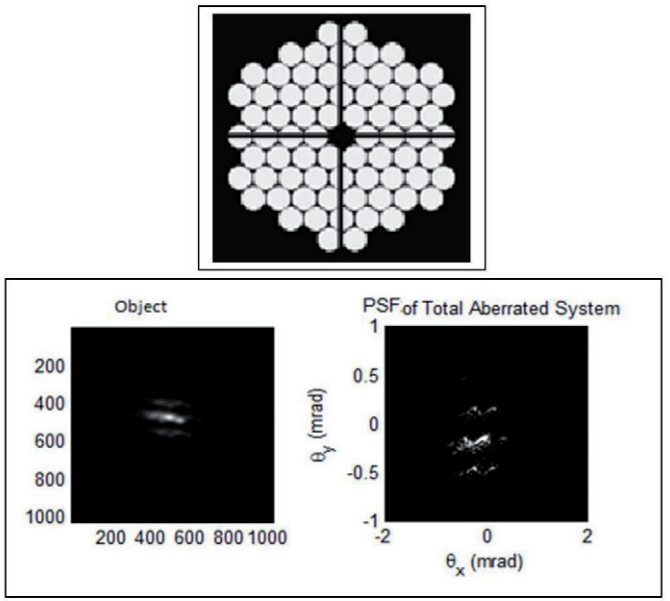

Figure (4.29): Diffraction Pattern for cir-6 Apodized Aperture.

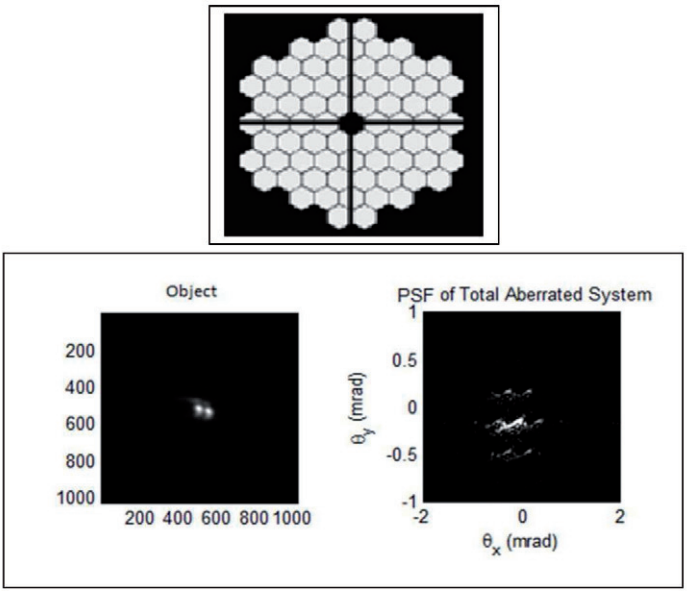

Figure (4.30): Diffraction Pattern for 6-6 Apodized Aperture.

4.7 Describing the Wave Aberration Function Using Modified Zernike Polynomials (H)

In the following section modified Zernike polynomials will be adopted. For hexagonal aperture, the aberration up to 5^{th} order will be calculated which represent traditional Seidel (primary) and second order aberrations as in figures (4.34, 4.35, 4.36 and 4.37).

4.8 Double-Index Modified Zernike Polynomials (H)

In a pyramid arrangement, according to table (2-2) in chapter two, figure (4.34) illustrates modified Zernike polynomials for hexagonal aperture up to 5^{th} order to represent different types of aberration modes.

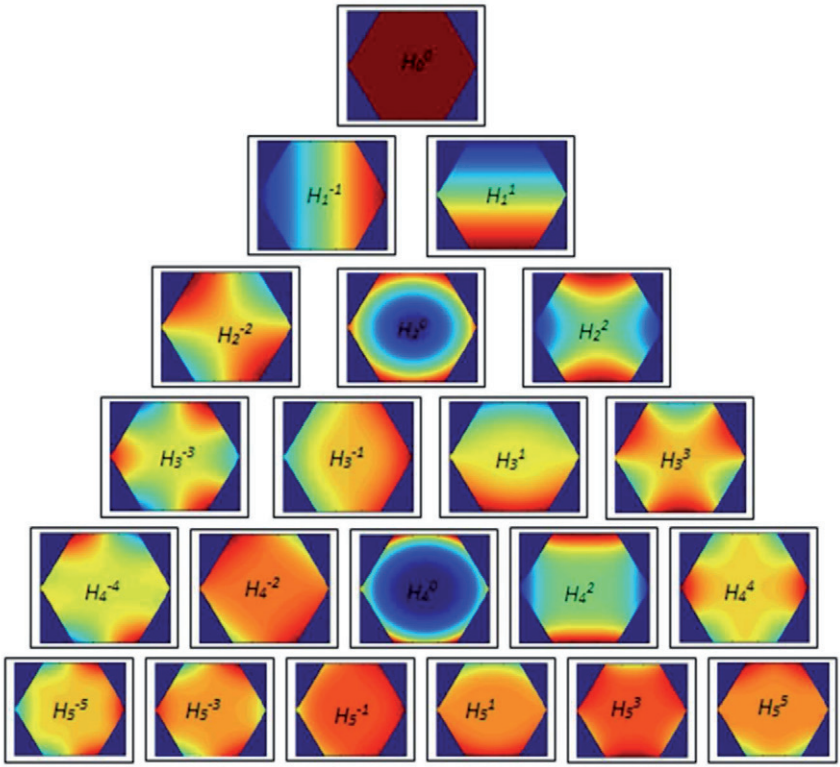

Figure (4.34): Modified Zernike polynomials up to 5th order.

4.9 Double-Index Modified Zernike Polynomial (H) PSFs

The PSF images for each mode of modified Zernike polynomials for the hexagonal aperture are illustrated in figure (4.35). For more explanation and representation the cross-section of the PSF in terms of visual angle (θ_x in x direction and θ_y in y direction) measured in *mrad* are shown in figures (4.36, 4.37).

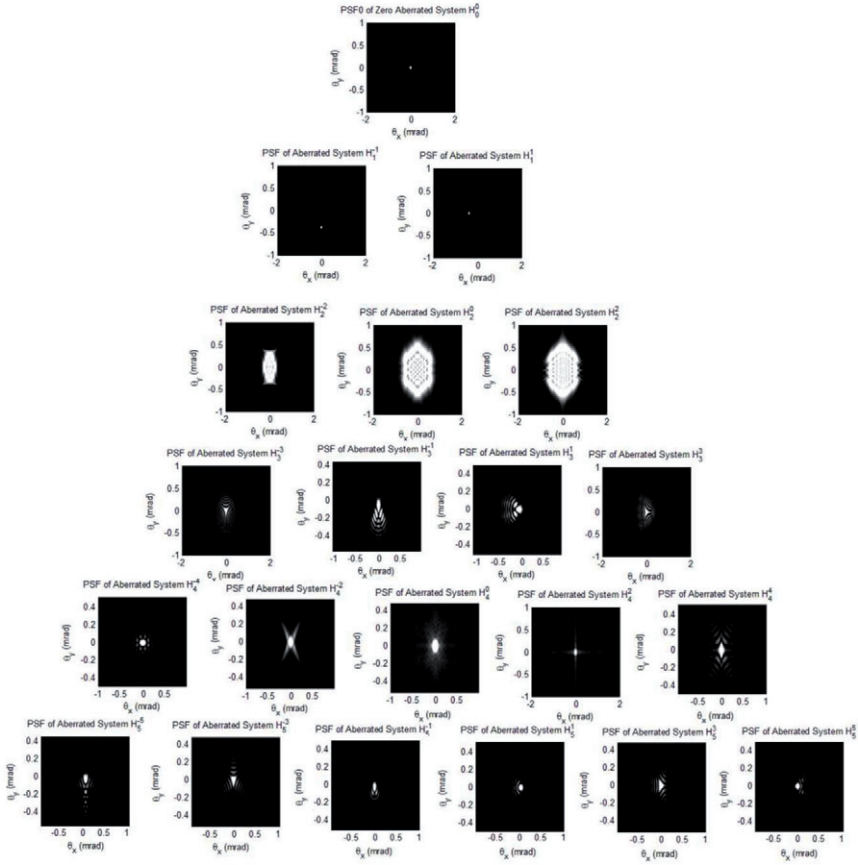

Figure (4.35): Double-Index Modified Zernike Polynomial (*H*) PSFs.

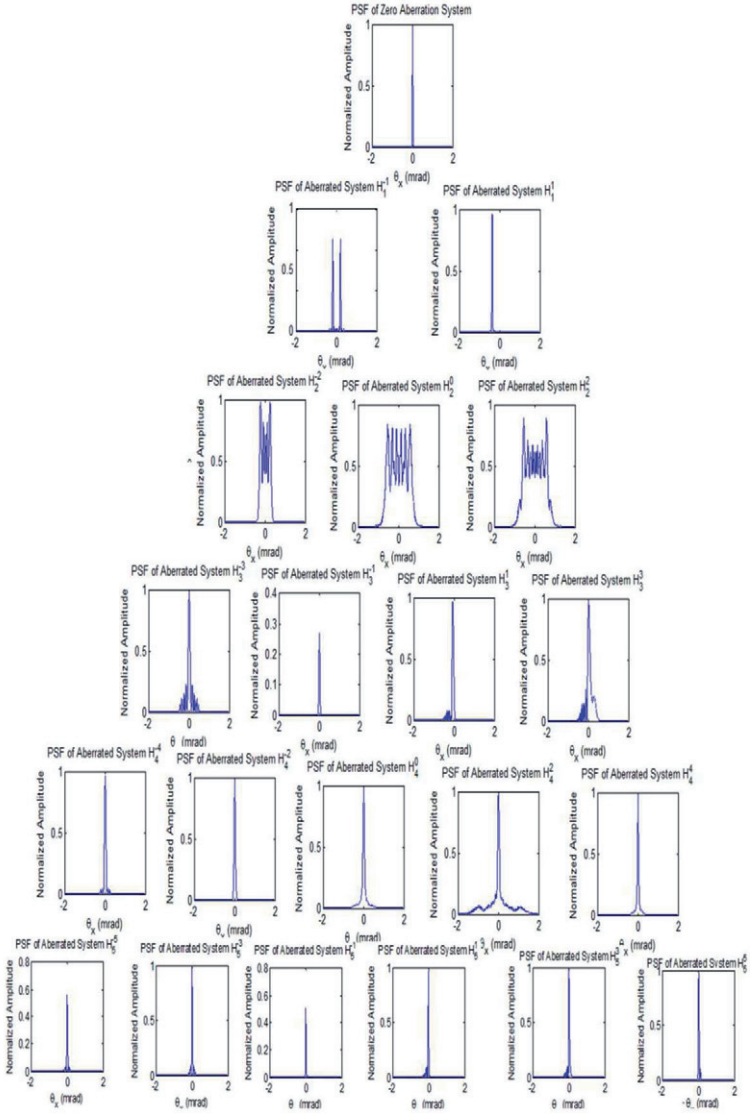

Figure (4.36): PSF Cross-Sections in Terms of Visual Angle θ_x(mrad).

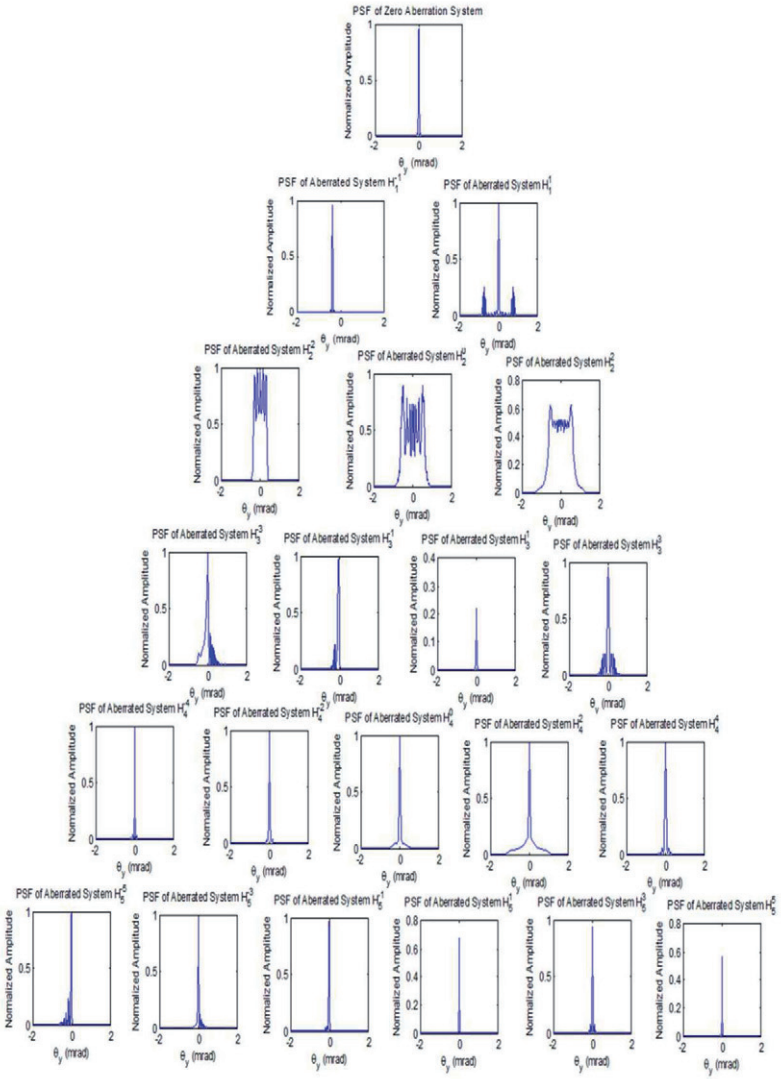

Figure (4.37): PSF Cross-Sections in Terms of Visual Angle θ_y(mrad).

A binary star simulation was carried out to visualize the earlier aberration up to 5th order (figure (4.38)). It can be seen from the figure that the first order aberration ($H_1^1, H_1^{-1}, H_2^2, H_2^{-2}, H_2^0, H_3^{-3}, H_3^{-1}, H_3^1, H_3^3$) contains the major part of optical aberration.

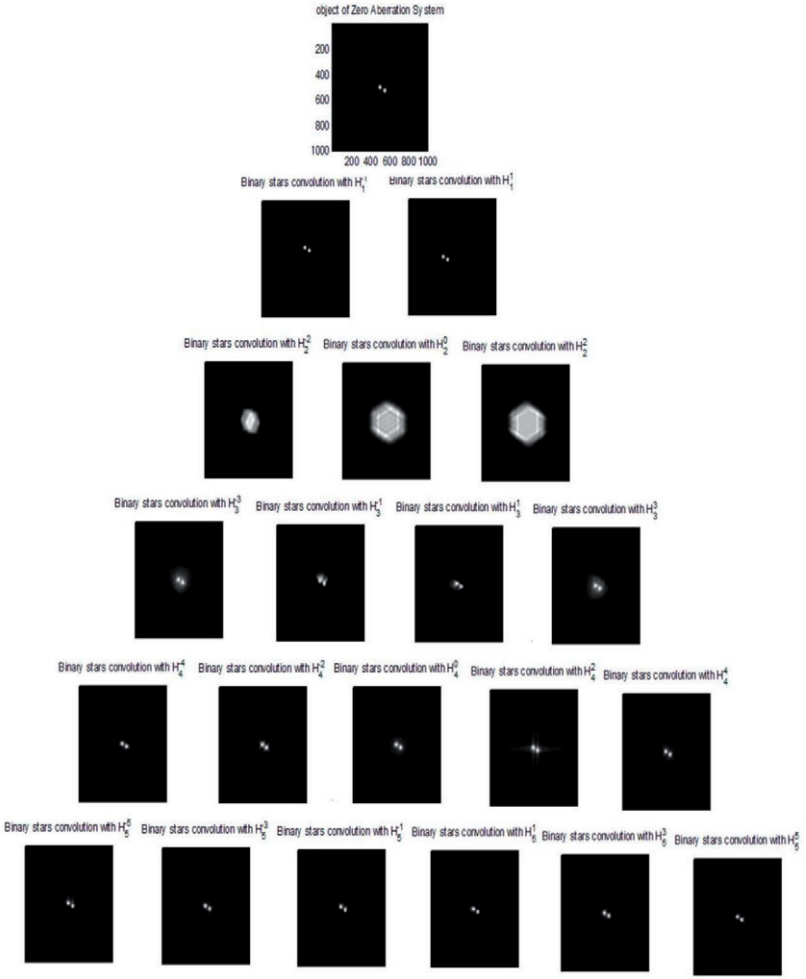

Figure (4.38): Polynomials Mode Aberration Images.

The observed image of the binary star (case study) as a result of almost all types of aberration is shown in figure (4.39). The plot in figure (4.40) illustrates the produced shape in a deformable mirror in adaptive optics system to correct and reduce most aberrations modes from the incident wavefront at hexagonal aperture of the telescope.

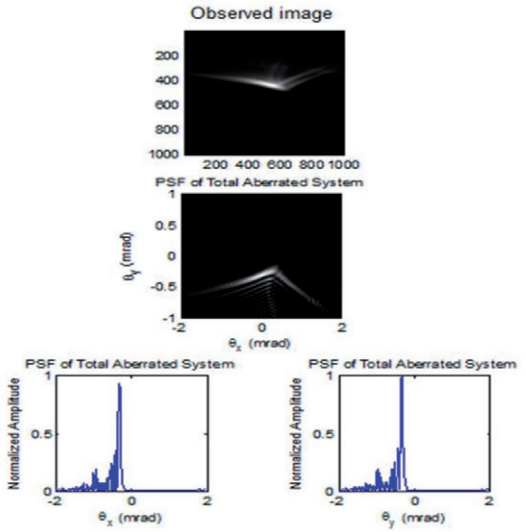

Figure (4.39): The Result of the Accumulative HModes (observed image).

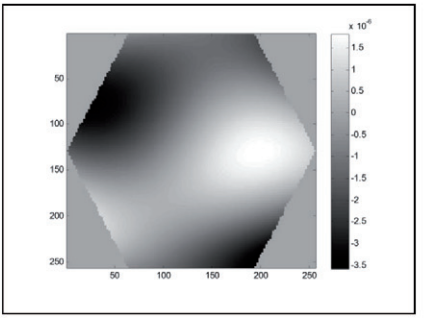

Figure (4.40): Plot Shows the Shape Produced in a Deformable Mirror in Adaptive Optics System.

The shape in figure (4.40) represents the initial state for adaptive optics correction that will be described later in section 4.7.
Phase map or aberrated 72-segment mirror for 6-6 apodized aperture can be illustrated in figure (4.41).

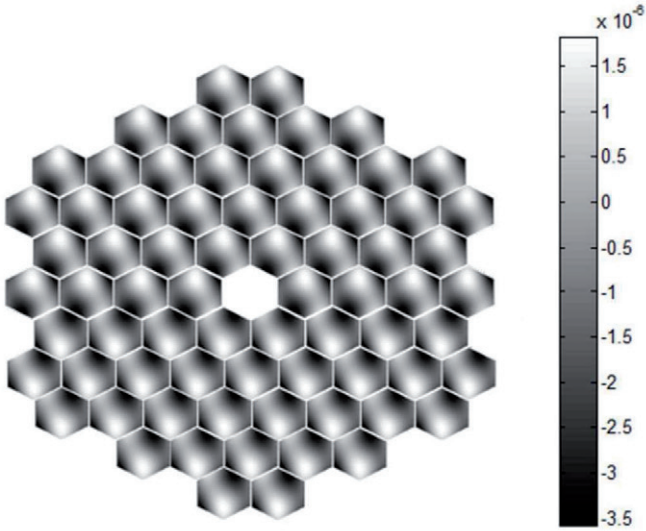

Figure (4.41): Phase Map for Aberrated Aperture.

4.10 Implementation and Results of Computer Simulations for AO Process

In AO setup, the control software is the vital link between the wavefront sensor and the deformable mirror. In essence, the control software for spot field deviations can be used to reconstruct the phase of the incident beam and generate the conjugate commands of the DM.

The surface of the deformable mirror is controlled by 32 actuators as an example arranged on a 6 x 6 grid with no actuators on the corners. Shack- Hartmann wavefront sensors are arranged on a 14 x 14 grid with the corners obscured, so that there are 196 wavefront slope measurements in two directions. Thus, the Poke matrix (P) is 196 x 32 elements. To accomplish an AO process for an optical system steps below explain the process to fit an arbitrary surface using DM influence functions. Phase space will be used instead of gradient or Laplacian (curvature) space because of the lake of sensors.

1) Evaluating the Control Matrix with Poke-Control Product

After generating the control matrix as shown as in figure (4.42), one way of evaluating the quality of the control matrix is to multiply it by the Poke matrix and compare it with an identity matrix as shown in figure (4.43). A single number metric is the RMS of the difference between the Poke-control product and the identity matrix, which would ideally be zero. If it is significantly non-zero then the control matrix may be poorly conditioned for adaptive optics.

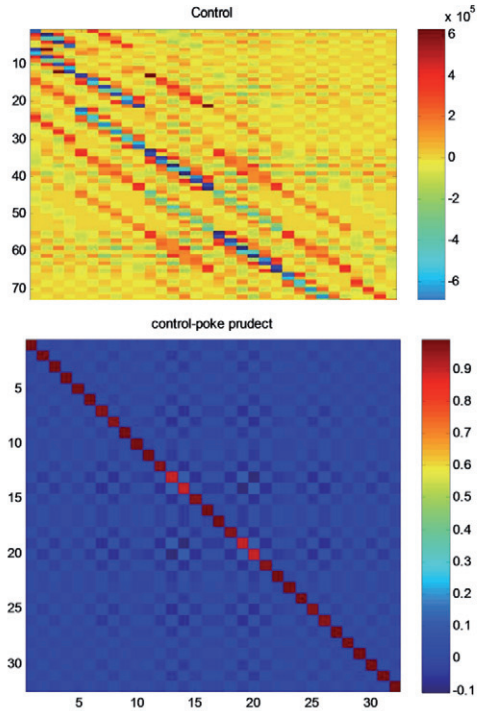

Figure (4.43): Control-Poke Product.

2) SVD Mode and Control Matrix Analysis

The decomposition of actuator and sensor spaces can be introduced for adaptive optics. The decomposition, which is based on the SVD of the "Poke matrix," provides orthonormal bases, or modes, for both actuator and sensor spaces. These modes are useful for the design of the control loops, as well as for analysis of the wavefront error and the performance of the control loops [88].

Figure (4.44) shows the singular values (S) of the control matrix (Γ). There are 32 positive singular values, corresponding to the 32 actuator degrees of freedom that remain after the piston mode is removed.

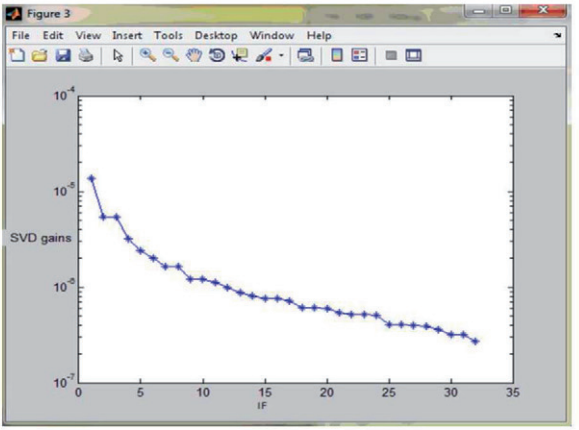

Figure (4.44): SVD Gains from Measured Poke Matrix.

It is a common to examine the magnitudes of the gains from the SVD calculation to determine the quality of the Poke matrix and help to identify any problems.

The condition number was 49.8 indicating a fairly good Poke matrix, but analysis of the SVD gains shown in Figure (4.44), showed an area of potential improvement. The highest gain was significantly higher than the others gain, indicating a problem with a background static aberration in the system.

3) The Measured Poke Matrix Analysis

The measured slopes in the Poke matrix together are averaged to show the background pattern, and then this average Poke is subtracted from the Poke matrix to produce cleaner Poke matrix, as in Figure (4.45). A comparison of the cleaner poke matrix with the measured Poke matrix is shown in figure (3.18) is clear. The horizontal streaks that were in the previous measured Poke matrix have been removed and the pattern is much clearer.

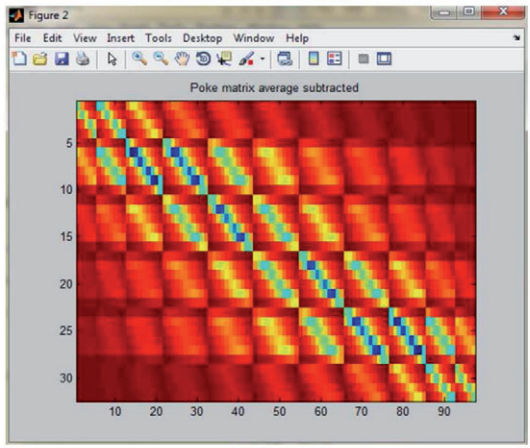

Figure (4.45): Poke Matrix with Average Slope Removed.

After removing the static aberration from the background, the amplitude of the measured of the influence function (Poke) is examined by subtracting the maximum slope from the minimum slope for each actuator to evaluate the efficacy of each actuator. The peak-to-valley Poke amplitude for each influence function is given by figure (4.46). This plot shows that some of the actuators do not have strong influence on the wavefront sensor as others, although they are so small, but it is unsecured to neglect from the matrix since they are all significantly above the wavefront sensor noise floor.

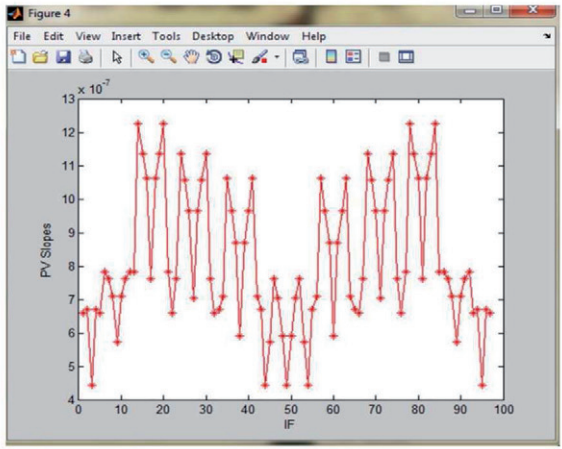

Figure (4.46): Peak to Valley Slopes for Each Influence Function.

4) Creating the Phase Screen

The phase screen can be generated as mentioned in section 4.3 or from the orthonormal Zernike/ modified Zernike polynomials modes mentioned in chapter 2, as shown in figure (4.47).

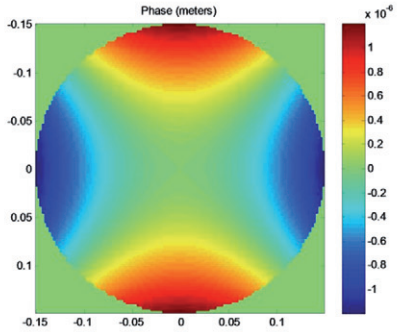

Figure (4.47): Zernike mode Z_2^2

5) Generating DM Commands

This next section of simulation takes the sampled shape from phase screen as a vector and multiplies it by the control matrix generated earlier to create a vector of actuator forces or commands. The commands are then displayed as a bar chart as shown in figure (4.48). To simulate throw limitations of the DM, we assumed a 50% throw bias is assumed to limit the DM force range to ±50%. Figure (4.49) display the requested forces, limited forces and the difference between them.

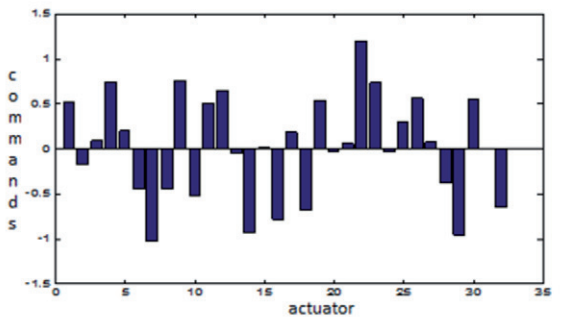

Figure (4.48): Actuator Commands.

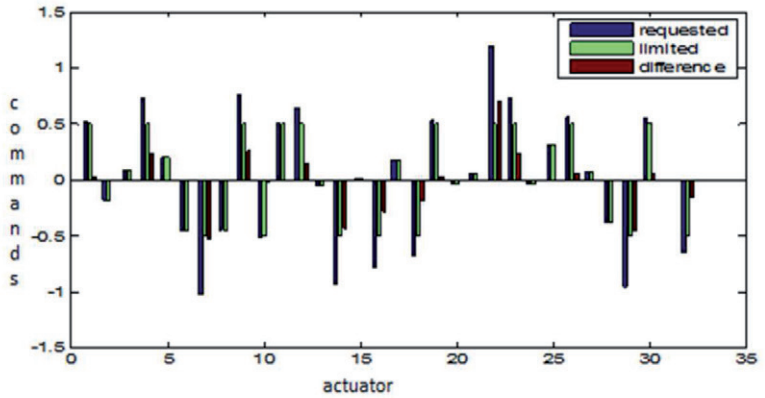

Figure (4.49): Actuator Requested, Limited, Difference Commands.

6) Constructing the DM Surface Using the Poke Matrix Method

The final stage of the simulation is constructing the DM surface by summing the influence functions (Poke matrix) weighted by the commands. Figures (4.50, 4.51 and 4.52) display the results and analysis.

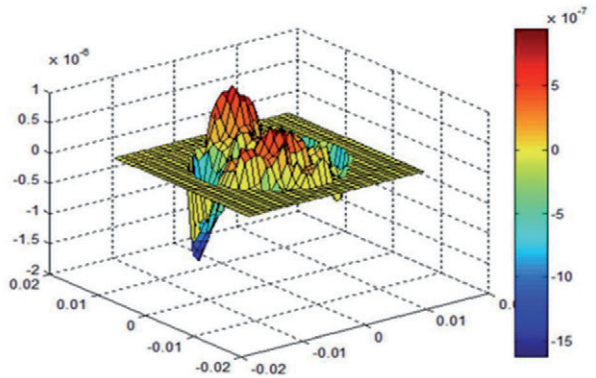

Figure (4.50): The Wavefront Shape (Desired Shape).

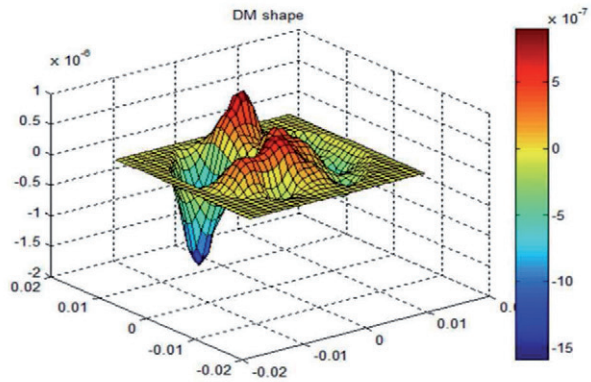

Figure (4.51): The Deformable Mirror Shape.

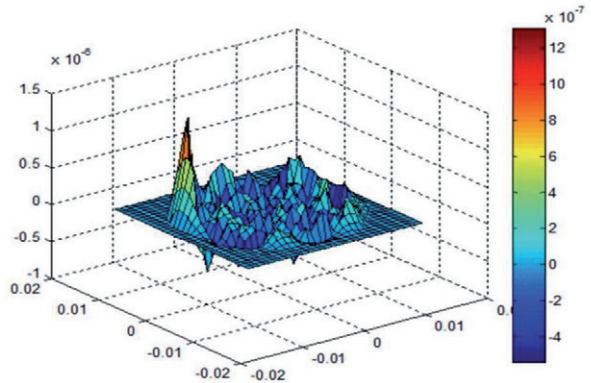

Figure (4.52): Difference between Desired Shape and DM Shape (Residual Error).

Applying AO process using the Poke matrix to correct the phase screen (Kolmogorov spectrum) turbulent is given in figure (4.53). This figure contains the ideal PSF for the optical system without turbulent, distorted PSF and corrected PSF, also contains blurred image and corrected image.

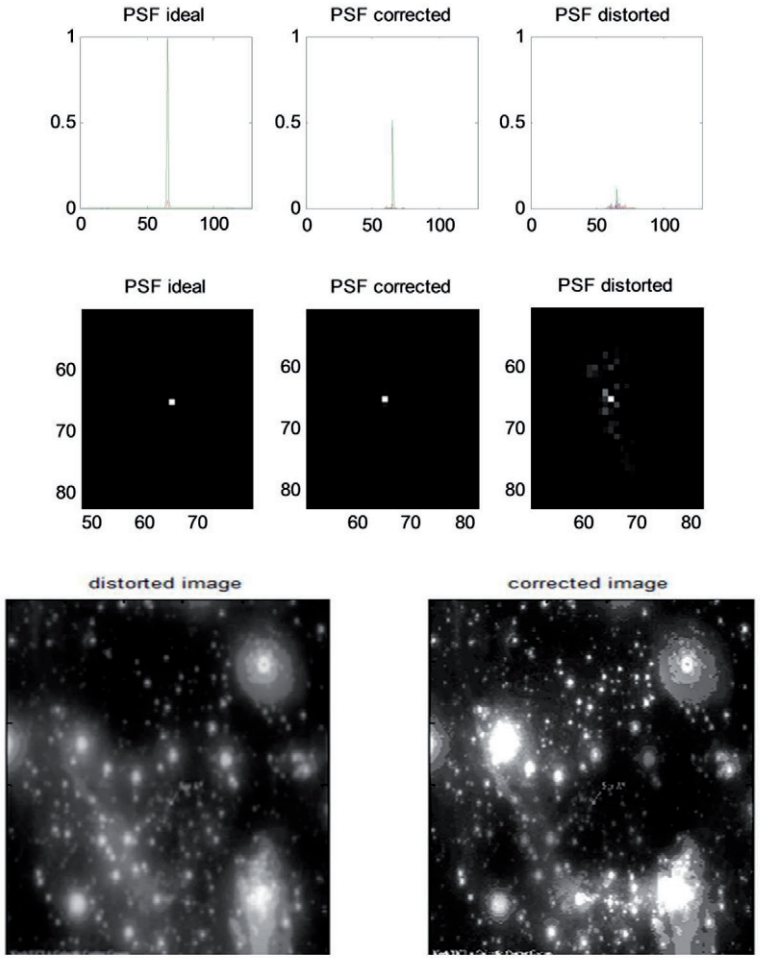

Figure (4.53): Point spread functions (top) and corrected images (down) with AO system.

7) Reproduction of Zernike Modes using Poke Matrix Method

Zernike modes up to 5th order can be generated to represent the turbulent as in figures (4.54, 4.55 and 4.56) and then corrected using AO process as in figure (4.57).

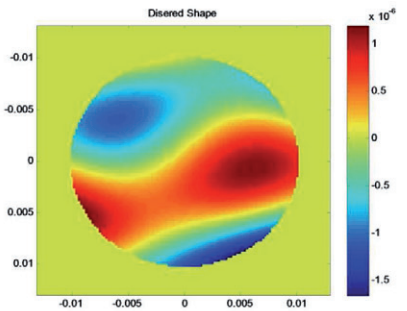

Figure (4.54): Aberrated Wavefront Shape (up to 5th order).

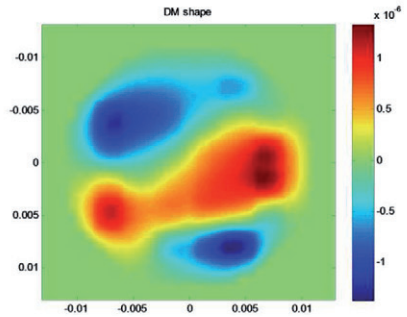

Figure (4.55): The Deformable Mirror Shape.

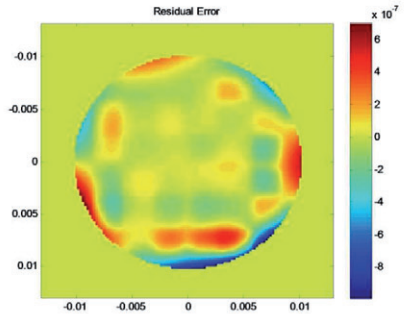

Figure (4.56): The Residual Error.

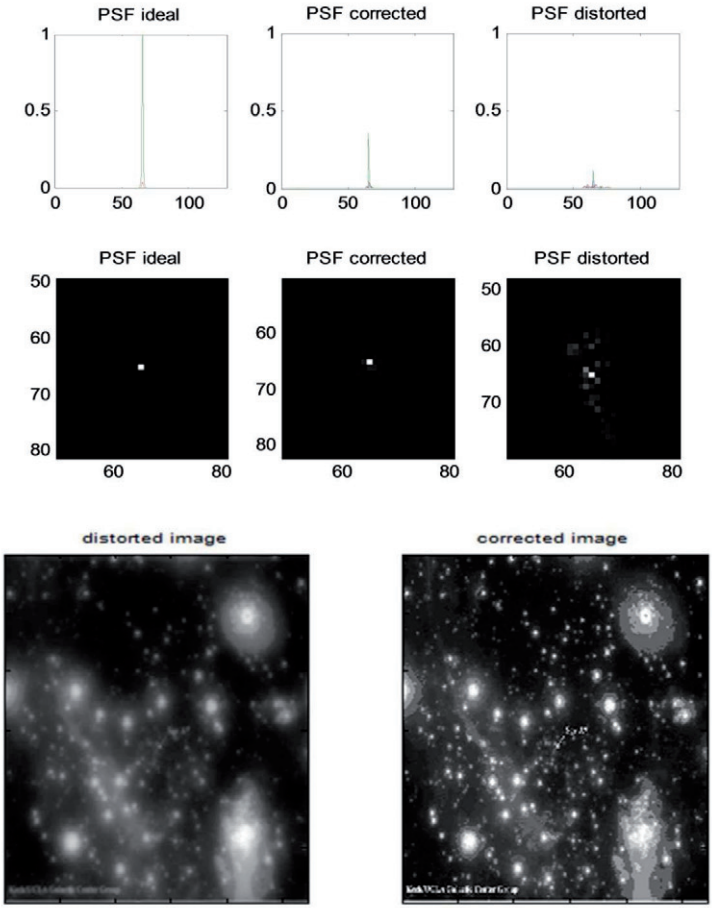

Figure (4.57): Point spread functions (top) and corrected image (down) with AO system.

8) Reproduction Modified Zernike Modes Using Poke Matrix Method

The plots in figures (4.58, 4.59, 4.60, 4.61 and 4.62) illustrated the results of using Poke matrix method for correction the aberration of the modified Zernike polynomials up to 5th order for hexagonal aperture in AO system.

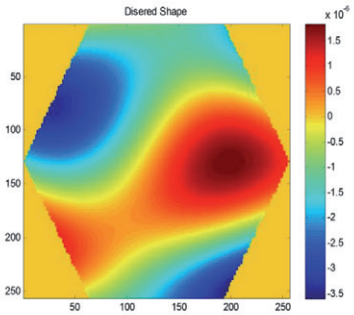

Figure (4.58): Shape of an Aberrated Wavefront (up to 5th order).

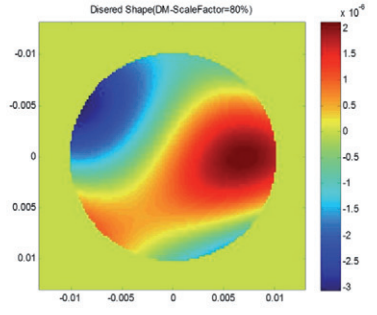

Figure (4.59): Desired Shape (DM with Scale Factor 80%).

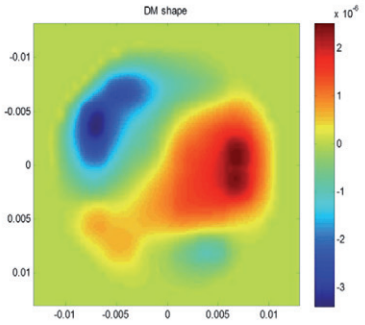

Figure (4.60): The Deformable Mirror Shape.

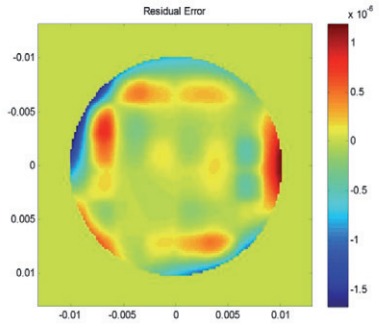

Figure (4.61): The Residual Error

Therefore, must be neglected.

The residual error in figure (4.61) is due to the limitations of the DM's actuators and to the neglected edges correction.

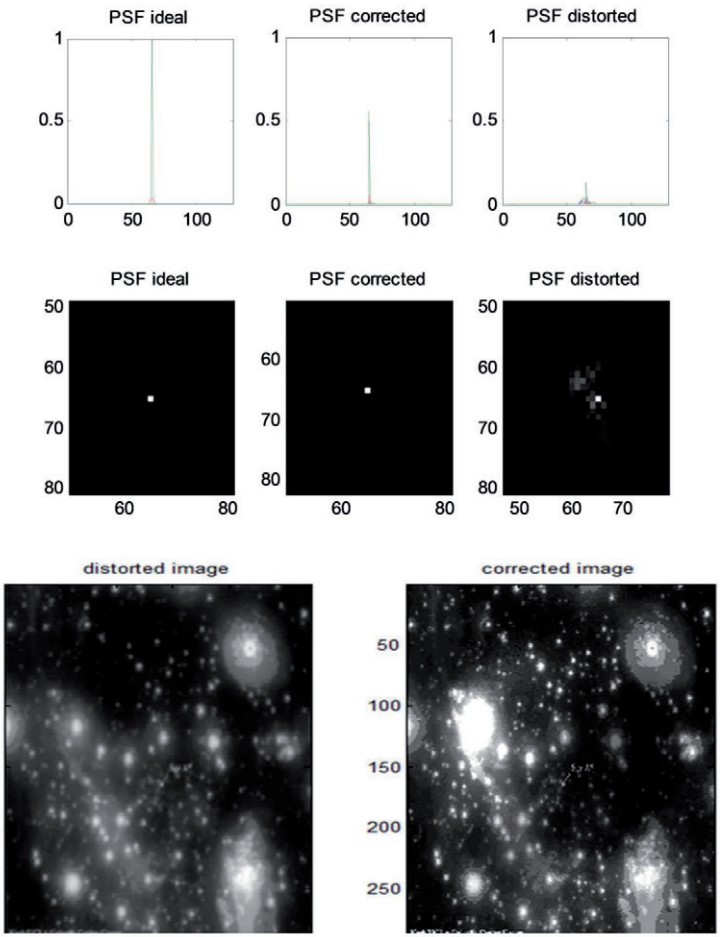

Figure (4.62): Point spread functions (top) and corrected image (down) with AO system.

9) Constructing the DM Surface Using Zernike/modified Zernike Polynomials

Applying AO process using the Zernike/modified Zernike polynomials to correct the phase screen (Kolmogorov spectrum) turbulent is given in figures (4.63, 4.64).

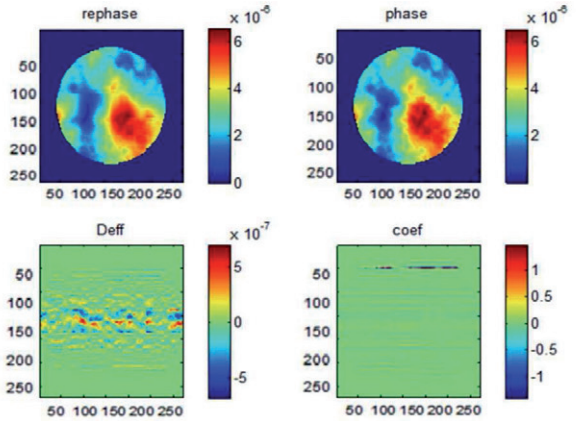

Figure (4.63): Phase Retrieval Using Zernike Method.

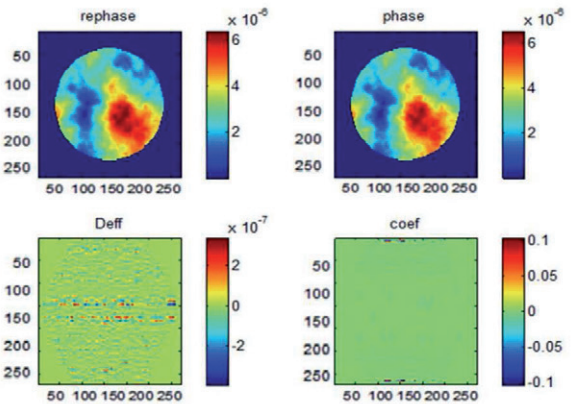

Figure (4.64): Phase Retrieval Using Modified Zernike Method.

4.11 The suggested Method for AO Surface Fitting

An efficient algorithm for the adaptive optics system of large telescopes will be presented. This improved method depend on sine or cosine trigonometric orthogonal

function (figure (4.65)) to determine the best surface fitting for AO process instead of the Poke matrix Zernike/modified Zernike method. The powerful of this algorithm is that it's more accurate with less complexity to determine the coefficients of wavefront reconstruction using least square fitting criteria, which represent the actuators commands of the DM surface. Another important property of this algorithm, that it can be used for any arbitrary shapes of the telescope aperture. The corresponding residual error is significantly smaller than of Zernike and modified Zernike polynomial for both circular and hexagonal aperture.

The mathematical expression for the suggested method is:

$$trigo = \sin((\bar{x}^2 + \bar{y}^2)\frac{\pi}{180}) \bmod (rand.\bar{x}, 10) \qquad \text{.....} \quad (1.4)$$

Where:

rand is uniformly distributed random numbers.

Mod is a Modulus after division.

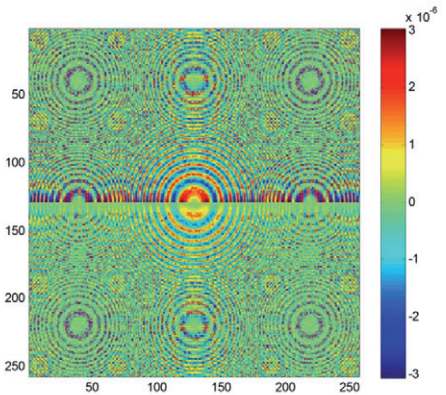

Figure (4.65): The Shape of Proposed Method Function.

4.12 Constructing the DM Surface using the suggested Method (Trigonometric function)

The two figures (4.66, 4.67) show the comparison between Poke matrix method and the suggested method for correcting the phase screen turbulent. The residual error of the AO correction using new suggested method is very small (10^{-19}) compared to Poke matrix method (10^{-7}).

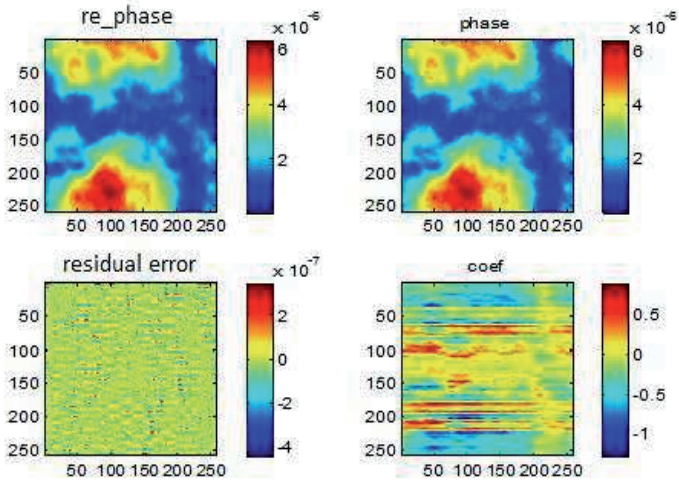

Figure (4.66): Phase Retrieval Using Poke Matrix Method.

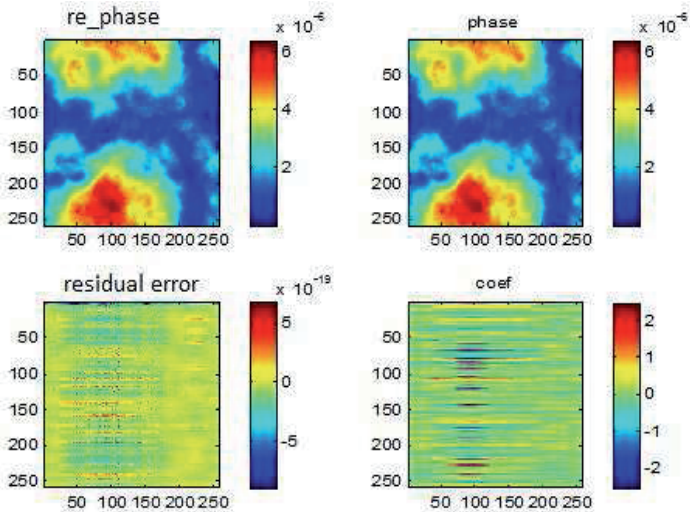

Figure (4.67): Phase Retrieval Using the Suggested Method.

Figures (4.68, 4.69) show the result of the new suggested method for correcting the aberration due to Zernike polynomials (up to 5th order) for circular aperture and modified Zernike polynomials (up to 5th order) for hexagonal aperture respectively.

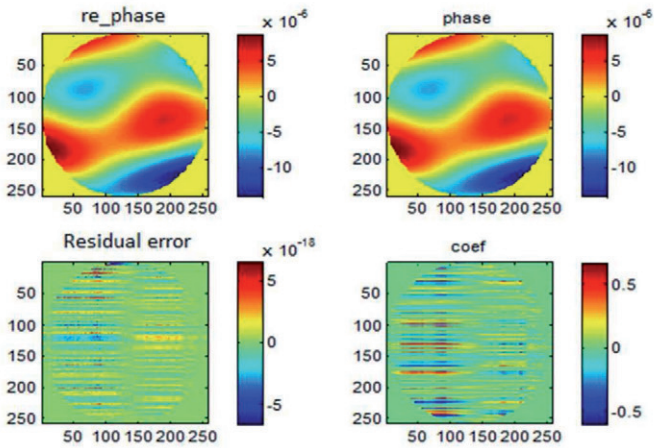

Figure (4.68): Phase Retrieval Using the Suggested Method for Circular Aperture

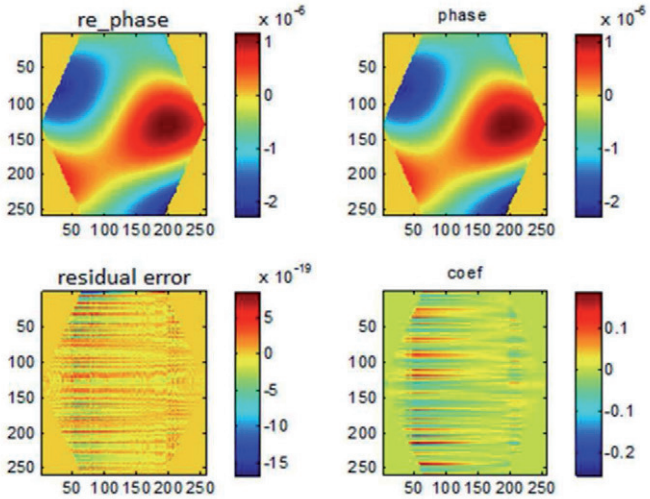

Figure (4.69): Phase Retrieval Using the Suggested Method for Hexagonal Aperture.

4.13 Strehl Ratio Calculations

Tables (4-4, 4-5 and 4-6) illustrate the reconstruction process of the wavefront, where the RMS wavefront error calculated in meter and in radiance to determine uncompensated/compensated Strehl ratio for the used methods.

Table (4-4) shows the result of using Zernike/modified Zernike polynomials method for reconstruction the DM surface to compensation the dynamic aberration type (Kolmogorov Model).

Table (4-4): Strehl Ratio Calculations for Zernike/modified Zernike polynomials Methods to correct Kolmogorov turbulence

Zernike Method		**Modified Zernike Method**	
RMS_WFE Uncomp. (m)	2.4576e-7	RMS_WFE Uncomp. (m)	2.4576e-7
RMS_WFE Uncomp. (rads)	2.4394	RMS_WFE Uncomp. (rads)	2.4394
RMS_WFE (m)	2.8870e-8	RMS_WFE (m)	1.4932e-8
RMS_WFE (rads)	0.2866	RMS_WFE (rads)	0.1482
SR_uncomp.	0.0026	SR_uncomp.	0.0026
SR	0.9212	SR	0.9783

When the perturbation is represented by static (Zernike/modified Zernike) and dynamic aberrations, tables (4-5, 4-6) show the result of using Poke matrix method and new suggested method to reconstruct the DM surface, respectively.

Table (4-5): Strehl Ratio Calculations for Poke Matrix Method to Correct Kolmogorov Turbulence, Zernike Turbulence and Modified Zernike Turbulence

Phase Screen (Kolmogorov) Turbulence		**Zernike Modes (Z) Turbulence**		**Modified Zernike Modes (H) Turbulence**	
RMS_WFE Uncomp. (m)	2.4576e-7	RMS_WFE Uncomp. (m)	4.2044e-7	RMS_WFE Uncomp. (m)	4.0139e-7
RMS_WFE Uncomp. (rads)	2.4394	RMS_WFE Uncomp. (rads)	4.1733	RMS_WFE Uncomp. (rads)	3.9842
RMS_WFE (m)	1.0462e-7	RMS_WFE (m)	1.1123e-7	RMS_WFE (m)	9.9504e-8
RMS_WFE (rads)	1.0384	RMS_WFE (rads)	1.1041	RMS_WFE (rads)	0.9877
SR_uncomp.	0.0026	SR_uncomp.	2.7301e-8	SR_uncomp.	1.2765e-7
SR	0.3402	SR	0.2955	SR	0.3770

Table (4-6): Strehl Ratio Calculations for the Suggested Method to Correct Kolmogorov Turbulence, Zernike Turbulence and Modified Zernike Turbulence

Phase screen (Kolmogorov) Turbulence		**Zernike modes (Z) Turbulence**		**Modified Zernike modes (H) Turbulence**	
RMS_WFE Uncomp. (m)	2.4576e-7	RMS_WFE Uncomp. (m)	4.2044e-7	RMS_WFE Uncomp. (m)	4.0139e-7
RMS_WFE Uncomp. (rads)	2.4394	RMS_WFE Uncomp. (rads)	4.1733	RMS_WFE Uncomp. (rads)	3.9842
RMS_WFE (m)	1.8928e-20	RMS_WFE (m)	5.6231e-20	RMS_WFE (m)	2.672e-20
RMS_WFE (rads)	1.8788e-13	RMS_WFE (rads)	5.5815e-13	RMS_WFE (rads)	2.652e-13
SR_uncomp.	0.0026	SR_uncomp.	2.7301e-8	SR_uncomp.	1.2765e-7
SR	0.9999	SR	0.9999	SR	0.9990

The results from tables (4-5, 4-6) are very clear; the improvement of the AO process using new suggested method instead of Poke matrix method increases the correction for Kolmogorov turbulent by 65.88%, 70.35% for Zernike turbulent and for modified Zernike turbulent by 62.2%. While compared with Zernike/modified Zernike polynomials methods (tables (4-4 & 4-6) improved the correction by 2.16% using modified Zernike polynomials and by 7.87% when using Zernike polynomials for Kolmogorov turbulent.

Chapter Five

Conclusions and Suggestions for Future Works

5.1 Conclusions

According to the investigation laid out in the book, different geometrical shapes were tested to build the proposal primary mirror for next generation optical telescope; like triangle, trapezium, pentagon, hexagon, heptagon, octagon…. and circular.

The simulation results showed that for non-segmented aperture the circular shape has the best PSF, highest MTF and largest cutoff frequency. Because of the technical constraints, mirrors with diameter more than 8m till now can not be built; the segmented apodized aperture suggested overcoming this constraint.

The apodized aperture with 250 pixels radius has the highest contrast (MTF) was for the hexagonal aperture with subsegments trapezium, hexagon and circular with almost the same, which means that the hexagonal apodized aperture is the optimal shape (figures (4.7, 4. 11, 4.15)).

For orthogonality reason related to Zernike polynomials, the uncompleted outer segments have to be removed (figure (4.20)). After clipping, the apodized apertures were tested again according to the size of subsegments, obscuration, spiders, and gaps between subsegments. The simulation result showed that the 4-6 apodized aperture has the best alignment, highest MTF, largest cutoff frequency, highest PSNR, and the largest collecting area, but under critical condition (deformation the gaps between the subsegments) this configuration produces an artificial diffraction pattern that destroyed the PSF of the optical system. The 6-6 apodized aperture configuration that has 72 subsegments with 25 pixels radius was more resist to this defects. Therefore, this configuration is the recommended design.

Modified Zernike polynomials were used to estimate the initial state of the Adaptive optics process.

The results of the suggested method showed the correction improvement of the AO process as shown in tables (4-4, 4-5, 4-6).

The suggested method increases the correction over the Poke matrix method for:

- Kolmogorov turbulent by 65.88% .
- Zernike turbulent by 70.35% .
- Modified Zernike turbulent by 62.2% .

The suggested method improves the correction for Kolmogorov turbulent in comparison with:

- Zernike polynomials method by 2.16% .
- Modified Zernike polynomials method by 7.87% .

5.2 Suggestions for Future Works

One may suggest the following ideas to the framework of the present investigation:

1. Using larger deformable secondary mirror instead of small DM to increase the field of view correction.
2. Increasing corrected field of view which is related to integration time and small isoplanatic angle by using "Multi-Conjugated Adaptive Optics" (MCAO) (tomography), through a number of DMs conjugated at different altitude in order to compensate the turbulence by layers and thus extended the field of view.
3. The final implication of using real stars or "natural" guide stars (NGS) as a reference star is limited sky-coverage, to overcome these limitation "artificial" stars called laser guide star (LGS) may be proposed.
4. Coronographic instruments can be included into telescope design to get more reliable results.

References

References

[1] M. Lyubenova and M. Kissler-Patig, “An Expanded View of the Universe”, Science with the European Extremely Large Telescope, 2009

[2] D. Silva, P. Hickson, C. Steidel, M. Bolte, “TMT Detailed Science Case: 2007”, TMT Observatory Corporation, 2007.

[3] L. Pasquini, G. Avila, H. Dekker, B. Delabre, S. D’Odorico, A. Manescaua, M. Haehnelt, B. Carswell, R. Garcia-Lopez, R. Lopez, M.T. Osorio, R. Rebolo, S. Cristiani, P. Bonifacio, V. D’Odorico, P. Molaro, P. Spano’, F. Zerbi, M. Mayor, M. Dessauges, D. Megevand, F. Pepe, D. Queloz, S. Udry, “CODEX: the High Resolution Visual Spectrograph for the E-ELT”, http://www.eso.org/sci/libraries/SPIE/7014-52.pdf, 2008.

[4] J. D Monnier, “Optical Interferometry in Astronomy”, Reports on Progress in Physics, Vol. 66, pp. 789–857, April 2003.

[5] M. V. Klein, T. E. Furrak,”Optics”, Second Edition, Printed in Singapore, 1986.

[6] D. J. Schroeder, “Astronomical Optics”, Second Edition, Library of Congress Cataloging, 2000.

[7] www.tmt.org/foundation-docs/index.html.

[8] A. T. Tokunaga and R. Jedicke, “New Generation Ground-Based Optical/Infrared Telescopes”, Encyclopedia of the Solar System, 2nd edition Editors: L. McFadden, T.V. Johnson, P.R. Weissman, Academic Press, 2006

[9] Michael Zeilik, Stephen A. Gregory, “introductory astronomy & astrophysics”, fourth edition, printed in USA, 1998.

[10] A. Abdullah and P. Ioannou, “Real-Time Control of a Segmented Telescope Test-Bed”, Proceeding Of the 42nd IEEE Conference on Decision and Control, Maui, Hawaii, Vol. 1, pp. 762-767, Dec. 2003.

[11] C. F. Dunkl, “Orthogonal Polynomials on the Hexagon”, SIAM Journal on Applied Mathematics, Vol. 47, No. 2, pp. 343-351, April 1987.

[12] R. G. Lane, A. Glindemann and J. C. Dainty, “Simulation of a Kolmogorov Phase Screen”, Waves in Random Media 2, pp. 209-224. Printed in the UK 1992.

[13] W. Swantner and W. W. Chow “Gram-Schmidt Orthonormalization of Zernike Polynomials for General Aperture Shapes”, Applied Optics, Vol. 33**,** No. 10, 1 April 1994.

[14] V. N. Mahajan “Zernike Circle Polynomials and Optical Aberrations of Systems with Circular pupils”, Supplement to Applied Optics, December 1994.

[15] G. Love and A. K. Saxena, “Active and Adaptive Optics for the New Generation of Large Telescopes”, Current Science, Vol. 66, No. 5, 1994.

[16] L. M. Mugnier, G. Rousset and F. Cassaing, “Aperture Configuration Optimality Criterion for Phased Arrays of Optical Telescopes”, Vol. 13, No. 12, J. Opt. Soc. Am. A, December 1996.
[17] A. Glindemann, S. Hippler, T. Berkefeld, and W. Hackenberg, “Adaptive Optics on Large Telescopes”, Kluwer Academic Publishers. Printed in the Netherlands, expaAG.tex; 1999.
[18] O. L. de Weck and D. W. Miller, “Integrated Modeling and Dynamics Simulation for the Next Generation Space Telescope”, Under the sponsorship of the NASA Goddard Space Flight Center, SSL#5-99, June 1999.

[19] J. S. Gibson, C. C. Chang and N. Chen, “Adaptive Optics with a New Modal Decomposition of Actuator and Sensor Spaces”, Proceedings of the American Control Conference, Arlington, VA June 25-27, 2001.
[20] G. Z. Angeli, M. K. Cho and M. S. Whorton, “Active Optics and Control Architecture for a Giant Segmented Mirror Telescope”, 2003. http://www.gsmt.noao.edu/documentation/SPIE_Papers/4840-22-presentation.pdf .
[21] R. Angel, J. Burge, J. L. Codona, W. Davison and B. Martin, “20 and 30 m Telescope Designs with Potential for Subsequent Incorporation into a Track - Mounted Pair (20/20 or 30/30)”, http://www.optics.arizona.edu/loft/Publications.htm, 2003.
[22] C. Cox and P. Hodge, “Point Spread Function Modeling for the James Webb Space Telescope”, www.stsci.edu/jwst/software/point-spread-function-modeling.pdf, 2004.
[23] E. Sabatke, J. Burge and D. Sabatke, “Analytic Diffraction Analysis of a 32-m Telescope with Hexagonal Segments for High-Contrast Imaging”, Applied Optics, Vol. 44, No. 8, March 2005.
[24] A. Beasley, “Xinζtics Deformable Mirror”, www.mso.anu.edu.au/technology/XineticsDM.pdf, 2007.
[25] V. N. Mahajan, and G.-m. Dai, “Orthonormal Polynomials in Wavefront Analysis: Analytical Solution”, J. Opt. Soc. Am. A, Vol. 24, No. 9, 2007.
[26] A. Basden, T. Butterley, R. Myers, and R. Wilson, “Durham Extremely Large Telescope Adaptive Optics Simulation Platform”, Applied optics, Vol. 46, Iss.7, pp. 1089-1098, March 2007.
[27] G. M. Dai, “Wavefront Reconstruction from Slope Data within Pupils of Arbitrary Shapes Using Iterative Fourier Transform”, the Open Optics Journal, Vol. 1, pp. 1-3, 2007.
[28] L. Jolissaint, B. Ellerbroek and G. Angeli, “Analytical Modeling of the Optical Transfer Function of a Segmented Telescope with/without Adaptive Optics Correction of the Telescope's Dynamical Aberrations”, SPIE Proceeding, Vol. 6271, June 2007.

[29] A. M. Hvisc and J. H. Burge, “Structure Function Analysis of Mirror Fabrication and Support Errors”, SPIE Proceeding, Vol. 6671, 2007.
[30] T. Gray and D. W. Miller, ”Minimizing High Spatial Frequency Residual in Active Space Telescope Mirrors”, M.Sc. Thesis, Department of Aeronautics and Astronautics, June 2008.
[31] E. Sidick**,** S. A. Basinger and D. C. Redding, “Improved Wavefront Control Algorithm for Large Space Telescopes”, SPIE Proceeding, Vol. 7015, 2008.
[32] G. m. Dai and V. N. Mahajan, “Orthonormal Polynomials in Wavefront Analysis: Error Analysis”, Applied Optics, Vol. 47, No. 19, July 2008
[33] A. Beghi, A. Cenedese, and A. Masiero, “Algorithms for Turbulence Compensation in Large Adaptive Optics Systems”, IEEE Conference publications, pp. 835-840, 2009.
[34] J. H. Allen, “Orthogonality and Convergence of Discrete Zernike Polynomials”, M.Sc. Thesis, University of New Mexico, Albuquerque, December 2010.
[35] C. D. Guzmán, “Technologies for Astronomical Wide-Field Adaptive Optics”, Ph.D. thesis, Department of Physics, Durham University, United Kingdom, December 2010.
[36] A. M. Nightingale, “Adaptive-Optic Approach to Mitigating Aero-Optic Disturbances for a Forced Shear Layer”, University of Notre Dame, Indiana, A Dissertation of Ph.D., December 2010.
[37] N. S. Brijlal, M. N. Avadhanulu, “A Textbook of Optics”, 2006.
[38] M. Bass, E. W. Van Stryland, D. R . Williams and W. L. Wolfe, “Handbook of Optics”, Second Edition, Devices, Measurements, and Properties, Vol. 2, McGRAW-HILL , INC. ,1995.
[39] Driggers, R. “Encyclopedia of Optical Engineering”, CRC, 2003
[40] E. Zarenski, “Limiting Magnitude in Binoculars”, Cloudy Nights Telescope Reviews, 2004.
[41] L. S. Pedrotti, ”Basic Physical Optics”, Fundamental of Photonics, Module 1.4, http://agamemnon.cord.org/step_online/st1-3/st13ttl.htm
[42] C. Schwab, “A Calibration System for a Rayleigh Laser Guide Star Constellation & A Planet around a Giant Star”, Dissertation of Doctor of Natural Sciences, University of Heidelberg, Germany, July 2010.
[43] W. G. Driscoll, W. Vaughan, “Handbook of Optics”, Sponsored by the Optical Society of America, 1978.
[44] R. J. Dorn, “A CCD Based Curvature Wavefront Sensor for Adaptive Optics in Astronomy”, Dissertation of Doctor of Natural Sciences, University of Heidelberg, Germany, November 2001.
[45] W. Cheng, “Propagation of Vortex Beam through a Turbulent Atmosphere”, M.Sc. Thesis, the School of Engineering of the University of Dayton, December 2009.

[46] A. M. Nightingale, “Adaptive-optic approach to Mitigating Aero-Optic Disturbances for Forced Shear Layer”, Ph.D. thesis, University of Notre Dame, December 2010.
[47] J. W. Goodman “Introduction to Fourier Optics”, Second Edition, San Francisco: McGraw Hill, 1996.
[48] J. D. Gaskill, “Linear Systems, Fourier Transforms, Optics”, New York: Wiley series in pure and applied optics, 1978.
[49] P. Y. Maeda, P. B. Catrysse, and B. A. Wandell “Integrating Lens Design with Digital Camera Simulation”, SPIE Proceeding Int. Soc. Opt. Eng., Vol. 5678, Digital Photography, pp. 48-58, 2005.
[50] J. C. Wyant, K. Creath, “Basic Wavefront Aberration Theory for Optical Metrology” Applied Optics and Optical Engineering, Vol. Xl, 1992
[51] R. N. Bracewell, “The Fourier Transform and Its Applications”, McGraw Hill, 2000.
[52] L. N. Thibos, R. A. Applegate, J. T. Schwiegerling and R. Webb, “Standards for Reporting the Optical Aberrations of Eyes”, Journal of Refractive Surgery, Vol. 18, October 2002.
[53] D. Malacara, “Optical Shop Testing”, library of congress, 1978.
[54] V. N. Mahajan, “Optical Imaging and Aberrations”, Part I, Ray Geometrical Optics, SPIE Press, 1998.
[55] L. Liang, B. Grimm, S. Goelz, J. Bille, “Objective Measurement of Wave Aberrations of the Human Eye with the use of a Hartmann-Shack Wave-front Sensor,” J. Opt. Soc. A, Vol. 11, No. 7, pp. 1949-1957, 1994.
[56] V. Lakshminarayanan and A. Fleck, “Zernike Polynomials: A Guide”, Journal of Modern Optics, Vol. 58, No. 7, pp. 545–561, April 2011.
[57] L. N. Thibos, “Handbook of Visual Optics”, v. 4/99, Indiana University, 1999.
[58] S. Yuan, “Tutorial on Strehl Ratio, Wavefront Power Series Expansion, Zernike Polynomials Expansion in Small Aberrated Optical Systems”, Arizona University, 2003.
[59] V. N. Mahajan and G.-m. Dai, “Orthonormal Polynomials for Hexagonal pupils: addendum”, J. Opt. Soc., Vol. 33, No. 10, 2008.
[60] V. N. Mahajan and G.-m. Dai, “Orthonormal Polynomials in Wavefront Analysis: Analytical Solution”, 2994 J. Opt. Soc. Am. A, Vol. 24, No. 9, September 2007.
[61] G. Dai, “Systems and Methods for Wavefront Reconstruction for Aperture with Arbitrary shape”, Patent application number: 20100238407, Assignees: AMO Manufacturing USA, LLC World Intellectual Property Organization, 2007.
[62] http://www.telescope-optics.net/

[63] M. Bass, E. W. Van Stryland, D. R . Williams and W. L. Wolfe, “Handbook of Optics”, Second Edition, Fundamentals, Techniques and Design, Vol. 1, McGRAW-HILL , INC ., 1995.
[64] D. Allen, “Adaptive Optics in Astronomy”, Physics 325, http://uw.physics.wisc.edu/~timbie/P325/Allen_adaptive_optics.pdf, Spring 2006.
[65] C. jingyuan, G. guangyong and T. yingxue “Modelling and Simulation of Adaptive Optics in the Scilab/Scicos Environment”, the Institute of Applied Physics and Computational Mathematics, Beijing, China, http://sciao.sourceforge.net/content.pdf
[66] T. P. Gabriele, “Active Control of a Thin Deformable in-Plane Actuated Mirror”, M.Sc. thesis, Department of Aeronautics and Astronautics, Air University, March 2007.
[67] P. Laird, R. Bergamasco, V. Berube, E.F. Borra, A. Ritcey, M. Rioux, N. Robitaille, S. Thibault, L. Vieira da Silva Jr and H. Yockell-Lelievre, “Ferrofluid Based Deformable Mirrors - a New Approach to Adaptive Optics Using Liquid Mirrors”, SPIE Proceeding of Astronomical Telescopes and Instrumentation meeting. arXiv:astro-ph/0212189. doi:10.1117/12.459065, August 2002.
[68] D. Brousseau, E. F. Borraa, S. Thibaultb, M. Ritceyc, J. Parenta, O. Seddikia, J.-P. Déryc, L. Faucherc, J. Vassalloa, A. Naderiana, “Wavefront Correction with a Ferrofluid Deformable Mirror: Experimental Results and Recent Developments”, SPIE Proceedings Vol. 7015, July 2008.
[69] http://en.wikipedia.org/wiki/Deformable_mirror
[70] E. Jordan “Design and Shape Control of Lightweight Mirrors for Dynamic Performance and Athermalization”, M.Sc. thesis, Department of Aeronautics and Astronautics, Massachusetts Institute of Technology, June 2007.
[71] P. Y. Maeda, “Zernike Polynomials and Their Use in Describing the Wavefront Aberrations of the Human Eye”, Psych 221/EE 362, Applied Vision and Imaging Systems, 2003.
[72] R. Tumbar, R. A. Stack, and D. J. Brady “Wave-Front Sensing with a Sampling Field Sensor”, Applied Optics, Vol. 39, No. 1, January 2000.
[73] D. R. Neal, M. E. Warren, J. K. Gruetzner, T. G. Smith and R. R. Rosenthal, “A Multi-Tiered Wavefront Sensor Using Binary Optics”, SPIE Vol. 2201, Adaptive Optics in Astronomy, 1994.
[74] G. Chanan, “Principles of Wavefront Sensing and Reconstruction”, Adaptive Optics for Vision Science and Astronomy, ASP Conference Series, Vol. **VOLUME**, **PUBLICATION YEAR** A. Quirrenbach, 2001.

[75] J. LeDue, L. Jolissaint, J.-P. V´eran and C. Bradley, “Calibration and Testing with Real Turbulence of a Pyramid Sensor Employing Static Modulation”, Vol. 17, No. 9, Optics Express 7186, April 2009.
[76] L. Jolissaint, “Synthetic Modeling of Astronomical Closed Loop Adaptive Optics”, arXiv: 1009.1581v2 [astro-ph.IM], November 2010.
[77] J. C. Dainty, A. V. Koryabin, and A. V. Kudryashov, “Low-Order Adaptive Deformable Mirror”, Vol. 37, No. 21, Applied Optics, July 1998.
[78] S. A. Cornelissen, A. L. Hartzell, J. B. Stewart, T. G. Bifano, P. A. Bierden, “MEMS Deformable Mirrors for Astronomical Adaptive Optics”, SPIE Proceeding, Vol. 7736, 2010.
[79] P. Nisenson, G. J. Melnick, J. Geary, M. Holman, S. G. Korzennike, R. W. Noyes, C. Papaliolios, D. D. Sasselov, D. Fischer, D. Gezari, R. G. Lyon, R. Gonsalves, C. Hardesty, M. Harwit, M. S. Marley, D. A. Neufeld and S. T. Ridgway “The Extrasolar Planet Imager”, Asp Conference Series, Vol. 294, 2003.
[80] D. N. Spergel, “A New Pupil for Detecting Extrasolar Planets”, arXiv:astro-ph/0101142v1, Jan 2001.
[81] J. Debes and Jian Ge, “High Contrast Imaging of Extrasolar Planets”, arXiv:astro-ph/0301051v1, Jan 2003.
[82] S. E. Umbaugh, “Computer Vision and Image Processing: A Practical Approach Using CVIPtools”, Prentice Hall, 1997.
[83] M. Cadik and P. Slavik, “Evaluation of two Principal Approaches to Objective Image Quality Assessment”, 8th International Conference on Information Visualisation, IEEE Computer Society Press, pp. 513-551, 2004.
[84] M. T. Heath, Scientific Computing: An Introductory Survey, McGraw-Hill, Boston, 1997.
[85] Y. Liu and S. Gibson, “Adaptive Control in Adaptive Optics for Directed Energy Systems”, Optical Engineering, Vol. 46, No. 4, April 2007.
[86] M. A. van Dam, A. H. Bouchez, D. Le Mignant, E. M. Johansson, P. L. Wizinowich, R. D. Campbell, J. C. Y. Chin, S. K. Hartman, R. E. Lafon, P. J. Stomski, and D. M. Summers, “The W. M. Keck Observatory Laser Guide Star Adaptive Optics System: Performance Characterization”, Publications of the Astronomical Society of the Pacific, pp. 310–318, February 2006.
[87] Y. Liu and S. Gibson, “Adaptive Optics with Adaptive Filtering and Control”, Proceeding of the 2004 American Control Conference Boston, Massachusetts, 2004.
[88] J. S. Gibson, C. C. Chang, and N. Chen, “Adaptive Optics with a New Modal Decomposition of Actuator and Sensor Spaces”, Proceedings of the American Control Conference Arlington, VA June 25-27, 2001.

Appendices

Appendix A

Zernike polynomials

In Table A.1 the Zernike polynomials computed from equations 2.29-2.31 are listed in polar coordinates as well as Cartesian coordinates. The conversion between the two coordinate systems is the ”standard” conversion:

$$\begin{cases} x = \rho\cos\theta \\ y = \rho\sin\theta \end{cases}$$

Table (A.1): Zernike Polynomials in polar and Cartesian Coordinates

n	m	i	Norm. factor	Zernike polynomials polar coordinates	Zernike polynomials Cartesian coordinates	Meaning
0	0	0	1	1	1	Piston or constant term
1	−1	1	2	$\rho\sin\theta$	y	Tilt y
1	1	2	2	$\rho\cos\theta$	x	Tilt x
2	−2	3	$\sqrt{6}$	$\rho^2\sin 2\theta$	$2yx$	Astigmatism ±45°
2	0	4	$\sqrt{3}$	$(2\rho^2-1)$	$-1+2x^2+2y^2$	Defocus
2	2	5	$\sqrt{6}$	$\rho^2\cos 2\theta$	x^2-y^2	Astigmatism 0° or 90°
3	−3	6	$\sqrt{8}$	$\rho^3\sin 3\theta$	$3yx^2-y^3$	Trefoil y
3	−1	7	$\sqrt{8}$	$(3\rho^3-2\rho)\sin\theta$	$-2y+3yx^2+3y^3$	Coma y
3	1	8	$\sqrt{8}$	$(3\rho^3-2\rho)\cos\theta$	$-2x+3x^3+3y^2x$	Coma x
3	3	9	$\sqrt{8}$	$\rho^3\cos 3\theta$	x^3-3y^2x	Trefoil x
4	−4	10	$\sqrt{10}$	$\rho^4\sin 4\theta$	$4x^3y-4y^3x$	Tetrafoil y
4	−2	11	$\sqrt{10}$	$(4\rho^4-3\rho^2)\sin 2\theta$	$-6yx+8x^3y+8y^3x$	Secondary astigmatism y
4	0	12	$\sqrt{5}$	$(6\rho^4-6\rho^2+1)$	$1-6x^2-6y^2+6x^4+12y^2x^2+6y^4$	Spherical aberration
4	2	13	$\sqrt{10}$	$(4\rho^4-3\rho^2)\cos 2\theta$	$-3x^2+3y^2+4x^4-4y^4$	Secondary astigmatism x
4	4	14	$\sqrt{10}$	$\rho^4\cos 4\theta$	$x^4-6y^2x^2+y^4$	Tetrafoil x
5	−5	15	$\sqrt{12}$	$\rho^5\sin 5\theta$	$5yx^4-10y^3x^2+y^5$	Pentafoil y
5	−3	16	$\sqrt{12}$	$(5\rho^5-4\rho^3)\sin 3\theta$	$-12yx^2+4y^3+15yx^4+10y^3x^2-5y^5$	Secondary trefoil y
5	−1	17	$\sqrt{12}$	$(10\rho^5-12\rho^3+3\rho)\sin\theta$	$3y-12yx^2-12y^3+10yx^4+20y^3x^2+10y^5$	Secondary coma y
5	1	18	$\sqrt{12}$	$(10\rho^5-12\rho^3+3\rho)\cos\theta$	$3x-12x^3-12y^2x+10x^5+20y^2x^3+10y^4x$	Secondary coma x
5	3	19	$\sqrt{12}$	$(5\rho^5-4\rho^3)\cos 3\theta$	$-4x^3+12y^2x+5x^5-10y^2x^3-15y^4x$	Secondary trefoil x
5	5	20	$\sqrt{12}$	$\rho^5\cos 5\theta$	$x^5-10y^2x^3+5y^4x$	Pentafoil x

n	m	i	Norm. factor	Zernike polynomials	
				polar coordinates	Cartesian coordinates
6	−6	21	$\sqrt{14}$	$\rho^6 \sin 6\theta$	$2xy(3x^2-y^2)(x^2-3y^2)$
6	−4	22	$\sqrt{14}$	$(6\rho^6-5\rho^4)\sin 4\theta$	$(6(x^2+y^2)-5)(4x^3y-4y^3x)$
6	−2	23	$\sqrt{14}$	$(15\rho^6-20\rho^4+6\rho^2)\sin 2\theta$	$2xy(15(x^2+y^2)^2-20(x^2+y^2)+6)$
6	0	24	$\sqrt{7}$	$20\rho^6-30\rho^4+12\rho^2-1$	$20(x^2+y^2)^3-30(x^2+y^2)^2+12(x^2+y^2)-1$
6	2	25	$\sqrt{14}$	$(15\rho^6-20\rho^4+6\rho^2)\cos 2\theta$	$(x^2-y^2)(15(x^2+y^2)^2-20(x^2+y^2)+6)$
6	4	26	$\sqrt{14}$	$(6\rho^6-5\rho^4)\cos 4\theta$	$(6(x^2+y^2)-5)(x^4-6y^2x^2+y^4)$
6	6	27	$\sqrt{14}$	$\rho^6\cos 6\theta$	$x^2(x^2-3y^2)^2-y^2(3x^2-y^2)^2$
7	−7	28	4	$\rho^7\sin 7\theta$	$4x^2y(x^2-3y^2)(x^2-y^2)+y(3x^2-y^2)(x^4-6x^2y^2+y^4)$
7	−5	29	4	$(7\rho^7-6\rho^5)\sin 5\theta$	$(7(x^2+y^2)-6)(5yx^4-10y^3x^2+y^5)$
7	−3	30	4	$(21\rho^7-30\rho^5+10\rho^3)\sin 3\theta$	$(3yx^2-y^3)(21(x^2+y^2)^2-30(x^2+y^2)+10)$
7	−1	31	4	$(35\rho^7-60\rho^5+30\rho^3-4\rho)\sin\theta$	$(35(x^2+y^2)^3-60(x^2+y^2)^2+30(x^2+y^2)-4)y$
7	1	32	4	$(35\rho^7-60\rho^5+30\rho^3-4\rho)\cos\theta$	$(35(x^2+y^2)^3-60(x^2+y^2)^2+30(x^2+y^2)-4)x$
7	3	33	4	$(21\rho^7-30\rho^5+10\rho^3)\cos 3\theta$	$(x^3-3y^2x)(21(x^2+y^2)^2-30(x^2+y^2)+10)$
7	5	34	4	$(7\rho^7-6\rho^5)\cos 5\theta$	$(7(x^2+y^2)-6)(x^5-10y^2x^3+5y^4x)$
7	7	35	4	$\rho^7\cos 7\theta$	$-4xy^2(x^2-y^2)(3x^2-y^2)+x(x^2-3y^2)(x^4-6x^2y^2+y^4)$
8	−8	36	$\sqrt{18}$	$\rho^8\sin 8\theta$	$8xy(x^2-y^2)(x^4-6x^2y^2+y^4)$
8	−6	37	$\sqrt{18}$	$(8\rho^8-7\rho^6)\sin 6\theta$	$2xy(3x^2-y^2)(x^2-3y^2)(8(x^2+y^2)-7)$
8	−4	38	$\sqrt{18}$	$(28\rho^8-42\rho^6+15\rho^4)\sin 4\theta$	$(28(x^2+y^2)^2-42(x^2+y^2)+15)(4x^3y-4y^3x)$
8	−2	39	$\sqrt{18}$	$(56\rho^8-105\rho^6+60\rho^4-10\rho^2)\sin 2\theta$	$2xy(56(x^2+y^2)^3-105(x^2+y^2)^2+60(x^2+y^2)-10)$
8	0	40	3	$70\rho^8-140\rho^6+90\rho^4-20\rho^2+1$	$70(x^2+y^2)^4-140(x^2+y^2)^3+90(x^2+y^2)^2-20(x^2+y^2)+1$
8	2	41	$\sqrt{18}$	$(56\rho^8-105\rho^6+60\rho^4-10\rho^2)\cos 2\theta$	$(x^2-y^2)(56(x^2+y^2)^3-105(x^2+y^2)^2+60(x^2+y^2)-10)$
8	4	42	$\sqrt{18}$	$(28\rho^8-42\rho^6+15\rho^4)\cos 4\theta$	$(28(x^2+y^2)^2-42(x^2+y^2)+15)(x^4-6y^2x^2+y^4)$
8	6	43	$\sqrt{18}$	$(8\rho^8-7\rho^6)\cos 6\theta$	$(x^2(x^2-3y^2)^2-y^2(3x^2-y^2)^2)(8(x^2+y^2)-7)$
8	8	44	$\sqrt{18}$	$\rho^8\cos 8\theta$	$(x^4-6y^2x^2+y^4)^2-(4x^3y-4y^3x)^2$

Appendix B

Matrix algebra

B) Linear least squares

We want to solve the equation

$$Ax = b \quad \ldots\ldots(B.1)$$

where A is of size $n \times m$, b is of size $n \times 1$ and x is of size $m \times 1$, and $n > m$. Since the system is over determined (i.e. $n > m$) there is no solution that solves the problem. Instead we want to find the vector b that minimizes the sum of the squared errors, i.e. minimizing the squared Euclidean norm:

$$\|r\|_2^2 = r^T r \quad \ldots\ldots(B.2)$$

where r is the error or the residual vector:

$$r = b - Ax \quad \ldots\ldots(B.3)$$

To minimize

$$\|r\|_2^2 = r^T r = (b - Ax)^T (b - Ax) = b^T b - 2x^T A^T b + x^T A^T Ax \quad \ldots\ldots(B.4)$$

we take the derivate with respect to x and set it to zero:

$$2A^T Ax - 2A^T b = 0 \quad \ldots\ldots(B.5)$$

which reduces to an $n \times n$ square linear system

$$A^T Ax = A^T b \quad \ldots\ldots(B.6)$$

If A has full rank, the matrix A^{T}A is non-singular and the least squares solution is given by:

$$x = (A^TA)^{-1}A^T b \qquad \ldots\ldots(B.7)$$

where $A^+ = (A^TA)^{-1}A^T$ is the Moore-Penrose pseudoinverse [26].

Appendix C

C) Singular value decomposition

The singular value decomposition, SVD, is an eigenvalue-like decomposition for rectangular matrices. The SVD of the real $n \times m$ matrix A has the form:

$$A = U\sum V^T \qquad \ldots\ldots(C.1)$$

where U is an $n \times n$ orthogonal matrix, V is an $m \times m$ orthogonal matrix and $\sum$ is an $n \times m$ diagonal matrix with

$$\sigma_{ij} = \begin{cases} 0 & for \quad i \neq j \\ \sigma_i \geq 0 & for \quad i = j \end{cases} \qquad \ldots\ldots(C.2)$$

where the diagonal elements σ_i are the singular values of A. They are usually ordered so that $\sigma_i \geq \sigma_{i+1}$ for $i = 1, \ldots, m-1$. The columns u_i of U and v_i of V are the corresponding singular vectors.

The singular values are the positive square roots of the eigenvalues of A^{T}A, and the columns of U and V are orthonormal eigenvectors of AA^T and A^{T}A, respectively (i.e. U and V are orthonormal $\leftrightarrow$ U^{T}U = I and V^{T}V = I, where I is the identity matrix).

The pseudoinverse of A (which also gives the least squares solution to the Problem in Appendix B.1) can now be computed by [26]:

$$A^+ = V\Sigma^+U^T \qquad \ldots\ldots(C.3)$$

The pseudoinverse of $\sum$ is obtained by transposing the matrix and inverting the diagonal entries (singular values). If a singular value is less than a predefined tolerance (tol) its inverse is set to zero (i.e. $\sigma_i^+ = 1/\sigma_i$ if $\sigma_i \geq tol$, otherwise $\sigma_i^+ = 0$ for i=1, ….., m).

If A should happen to be square and nonsingular, the pseudoinverse is the same as the usual matrix inverse, A^{-1}

الخلاصة

إن الهدف الاساس من تصميم الجيل القادم من التلسكوبات البصرية هو جمع المعلومات من المناطق البعيدة في الفضاء. هذه المعلومات ستستخدم لفهم: تركيبة الكون وولادة ونشوء النجوم واصل وتطور المنظومة الكوكبية والمجرات. المفتاح لأنجاز هذا الهدف هو بناء تلسكوب بصري فضائي او ارضي بمرآة عاكسة كبيرة. عدة صعوبات مرافقة لانشاء عاكس بهكذا حجم، لحل هذه الاشكالية هو بناء تلسكوب بصري ارضي او فضائي من خلال عدد من المرايا الصغيرة للتلسكوب الفضائي بالامكان حملها بواسطة المركبة الفضائية ومن ثم نشرها وترصيفها في المدار بالشكل المطلوب كقطعة واحدة عاكسة ومن ناحية ثانية فان التلسكوب البصري على سطح الارض اسهل تركيباً واقل كلفة.

نتائج المحاكاة اظهرت ان تركيبة الفتحة السداسية ذات الاجزاء السداسية (6-6) والتي تحتوي على 72 جزء هو التصميم الموصى به في تصميم الجيل القادم من التلسكوبات البصرية.

لتحسين وانجاز حد الحيود لتلسكوب المستقبل هنالك اساليب تفرض نفسها بقوة مثل المرآة المتغيرة (DM) وموضوع البصريات المطورة (AO) . النتائج الأولية لاختبار جبهة الموجة واعادة تركيب دالة الانتشار النقطية (PSF) باستخدام نظريات النمذجة العددية للمرآة المتغيرة الاحادية للبصريات المطورة قد انجزت ونتائجها الاولية قدمت.

تم تبني اربعة طرق لتركيب سطح DM لمكافأة جبهة الموجة الساقطة المشوهة هي:

متعددة حدود زرنايك و متعددة حدود زرنايك المطورة ومصفوفة البوك والطريقة المقترحة. نتائج المحاكاة اظهرت دقةً واقل زمناً حسابياً للطريقة الجديدة المقترحة.